National Library of Canada
Canadian Theses Service
Ottawa, Canada
K1A 0N4

Bibliothèque nationale du Canada
Services des thèses canadiennes

CANADIAN THESES

THÈSES CANADIENNES

NOTICE

The quality of this microfiche is heavily dependent upon the quality of the original thesis submitted for microfilming. Every effort has been made to ensure the highest quality of reproduction possible.

If pages are missing, contact the university which granted the degree.

Some pages may have indistinct print especially if the original pages were typed with a poor typewriter ribbon or if the university sent us an inferior photocopy.

Previously copyrighted materials (journal articles, published tests, etc.) are not filmed.

Reproduction in full or in part of this film is governed by the Canadian Copyright Act, R.S.C. 1970, c. C-30.

AVIS

La qualité de cette microfiche dépend grandement de la qualité de la thèse soumise au microfilmage. Nous avons tout fait pour assurer une qualité supérieure de reproduction.

S'il manque des pages, veuillez communiquer avec l'université qui a conféré le grade.

La qualité d'impression de certaines pages peut laisser à désirer, surtout si les pages originales ont été dactylographiées à l'aide d'un ruban usé ou si l'université nous a fait parvenir une photocopie de qualité inférieure.

Les documents qui font déjà l'objet d'un droit d'auteur (articles de revue, examens publiés, etc.) ne sont pas microfilmés.

La reproduction, même partielle, de ce microfilm est soumise à la Loi canadienne sur le droit d'auteur, SRC 1970, c. C-30.

THIS DISSERTATION
HAS BEEN MICROFILMED
EXACTLY AS RECEIVED

LA THÈSE A ÉTÉ
MICROFILMÉE TELLE QUE
NOUS L'AVONS REÇUE

NL-339 (r.86/06)

Canada

THE UNIVERSITY OF ALBERTA

STOCHASTIC MODELLING OF RIME ICING

by

© ALEXANDER LHOP KAON LIU

A THESIS

SUBMITTED TO THE FACULTY OF GRADUATE STUDIES AND RESEARCH

IN PARTIAL FULFILMENT OF THE REQUIREMENTS FOR THE DEGREE

OF MASTER OF SCIENCE

DEPARTMENT OF MECHANICAL ENGINEERING

EDMONTON, ALBERTA

FALL 1986

Permission has been granted to the National Library of Canada to microfilm this thesis and to lend or sell copies of the film.

The author (copyright owner) has reserved other publication rights, and neither the thesis nor extensive extracts from it may be printed or otherwise reproduced without his/her written permission.

L'autorisation a été accordée à la Bibliothèque nationale du Canada de microfilmer cette thèse et de prêter ou de vendre des exemplaires du film.

L'auteur (titulaire du droit d'auteur) se réserve les autres droits de publication; ni la thèse ni de longs extraits de celle-ci ne doivent être imprimés ou autrement reproduits sans son autorisation écrite.

ISBN 0-315-32321-3

THE UNIVERSITY OF ALBERTA

RELEASE FORM

NAME OF AUTHOR ALEXANDER LHOP KAON LIU

TITLE OF THESIS STOCHASTIC MODELLING OF RIME ICING

DEGREE FOR WHICH THESIS WAS PRESENTED MASTER OF SCIENCE

YEAR THIS DEGREE GRANTED FALL 1986

Permission is hereby granted to THE UNIVERSITY OF ALBERTA LIBRARY to reproduce single copies of this thesis and to lend or sell such copies for private, scholarly or scientific research purposes only.

The author reserves other publication rights, and neither the thesis nor extensive extracts from it may be printed or otherwise reproduced without the author's written permission.

(SIGNED) Alexander L. K. Liu

PERMANENT ADDRESS:

7470 Place Martin

Charlesbourg, Quebec

G1H 6C8

DATED October 9, 1986

THE UNIVERSITY OF ALBERTA

FACULTY OF GRADUATE STUDIES AND RESEARCH

The undersigned certify that they have read, and recommend to the Faculty of Graduate Studies and Research, for acceptance, a thesis entitled STOCHASTIC MODELLING OF RIME ICING submitted by ALEXANDER LHOP KAON LIU in partial fulfilment of the requirements for the degree of MASTER OF SCIENCE.

E.M. Bates
Supervisor

R. Forest

Edward Brown

Date October 9, 1986

Abstract

A two-dimensional stochastic rime icing model was developed to model rime feather growth at the ice accretion edges on a right circular cylinder. The straightline and curved trajectory models naturally produced a density variation along the surface of any arbitrary structure, unlike previous icing models. Both models were constructed for comparison of their growth angle and density predictions with experiment.

For cylindrical substrates, the growth angles of feathers from the curved trajectory model were in close agreement with experiment in flow conditions where droplets have large inertia and freeze individually. The density predictions from the straightline model agreed with experiment in flow conditions where the droplets tend to deform or coalesce in the region of the stagnation point on the cylinder. Otherwise, the curved trajectory model is a better predictor of local ice densities.

Acknowledgements

The author wishes to express his sincere appreciation to the various people who has contributed to the development of this thesis. First of all, without the guidance, encouragement, and understanding of Dr. E.M. Gates, the project would never have been completed. The author is also honoured to have had the opportunity to work with Dr. E.P. Lozowski of the Division of Meteorology. Their experience in the area of atmospheric icing was immense, and their persistent confidence in the experimental technique were significant contributing factors to the overall success of the project. Next, the author would like to thank Glenna Stirrett of the Cross Cancer Institute, Bill Andries of Dentistry, and Dr. Larry Filipow of the University of Alberta Hospital for their generous time and effort in explaining the fundamentals of X-radiation and its applications. Finally, the research was made possible with the financial assistance provided by the Department of National Defense.

Table of Contents

Chapter		Page
1.	INTRODUCTION	1
2.	DESCRIPTION OF STOCHASTIC RIME ICING MODELS	10
	2.1 Presentation of the Models	10
	2.1.1 The Straightline Trajectory Model	10
	2.1.2 The Curved Trajectory Model	12
	2.2 Implementation of Curved Trajectory Model	15
	2.3 Stochastic Model Features	17
3.	MODEL PREDICTIONS AND DISCUSSION	20
	3.1 Confidence in Curved Trajectory Model Predictions	22
	3.2 Rime Feathers	32
	3.2.1 Mechanisms for Feather-Growth	33
	3.2.2 Growth Angles	39
	3.3 Local Droplet Concentration	51
	3.3.1 Mechanisms for Developing Porous Accretions	52
	3.3.2 Density Variation	54
	3.3.3 Influence of Flow Parameters on Density	55
4.	EXPERIMENTAL INVESTIGATION	66
	4.1 Experimental Apparatus and Technique	66
	4.2 Measurement of Local Ice Density	71
	4.3 Experimental Procedure	77
5.	EXPERIMENTAL RESULTS AND COMPARISON WITH MODEL PREDICTIONS	82
	5.1 Rime Feathers	82
	5.2 Local Ice Density	93
	5.2.1 Description of Model of Bain and Gayet	93
	5.2.2 Model Predictions Versus Experiment	95

6. CONCLUSIONS 121

6.1 Rime Feather Growth Angles 121

6.2 Local Ice Densities 121

6.3 Applications 122

REFERENCES 123

APPENDIX 1 125

APPENDIX 2 127

APPENDIX 3 132

APPENDIX 4 133

APPENDIX 5 135

APPENDIX 6 146

APPENDIX 7 148

APPENDIX 8 150

List of Tables

Table — Page

3.1 Presentation of θ_m and E_m values calculated by Langmuir and Blodgett (1946) and from the curved trajectory model for a bare cylinder. D_c = 2.54 cm.....29

3.2 Growth angle measurements from straightline and curved trajectory models at various flow conditions 40

4.1 FROST tunnel conditions at which ice samples were produced on a cylinder for local ice density measurements 79

5.1 Calculation of $(-rv_o/T_s)$ at various flow conditions 84

5.2 Model predictions and rime feather growth angle measurements (degrees) at various flow conditions 91

5.3 Various parameters calculated for the experiments performed in the FROST tunnel 111

5.4 Various parameters calculated for the experiments performed by Prodi (1985). The ice accretions were grown on a 1 cm diameter cylinder 116

5.5 Average values for absolute stagnation point density (ρ_o) as calculated by Makkonen (1984) and by Macklin (1962) for a rotating cylinder. The calculations pertained to flow conditions from (a) FROST tunnel and (b) Prodi (1985) 120

List of Figures

Figure — Page

1.1 Comparison of ice accretion shape predictions from the model of Lozowski et al. (1983) with actual accretion shapes. U_∞ = 10 m/s, T_a = -10 °C, MVD = 130 μm 4

1.2 Comparison of accretion shapes produced by various models. D_c/D_d = 508, U_∞ = 10.7 m/s, T_a = -10 °C, and LWC = 0.48 g/m^3 7

2.1 Basic steps in a straightline model 11

2.2 Drag coefficient of a sphere as a function of Reynolds number ..13

2.3 Method of interpolation applied in the curved trajectory model .16

2.4 A straightline model produced by collecting 20,000 droplets on a cylinder. D_c/D_d = 1000 18

3.1 A straightline model produced by collecting 20,000 droplets on a cylinder. D_c/D_d = 508 21

3.2 Method of calculation of E_m and θ_m by Langmuir & Blodgett(1946) .23

3.3a Family of curves obtained by a differential analyzer for the determination of E_m at any flow condition 26

3.3b Family of curves obtained by a differential analyzer for the determination of θ_m at any flow condition 27

3.3c Family of curves obtained by a differential analyzer for the determination of V_1 at any flow condition 28

3.4 Comparison of (a) E_m and (b) θ_m from the curved trajectory with those from the curves of Langmuir and Blodgett (1946).....31

3.5 Effects of the droplet impact angle on the degree of shading activity downstream from discrete structures, for case with straightline trajectories.....34

3.6 A straightline model produced by collecting 10,000 droplets on an NACA 0012 airfoil. D_d = 25.4 μm 36

3.7 Straightline models produced by collecting 10,000 droplets on various wedges. D_d = 25.4 μm 38

3.8a A straightline model produced by collecting 20,000 droplets on a cylinder. D_d = 27.2 μm 42

3.8b A straightline model produced by collecting 20,000 droplets on a cylinder. MVD = 27.2 μm 43

3.9 Influence of three different limiting trajectories T_1, T_2, and T_3 on the magnitude of θ_m 46

3.10 Areas (shaded) on a droplet to which approaching droplets could stick 47

3.11 Diagrammatical definition of ζ. The ζ has a positive value, regardless of the sign for ψ 50

3.12 Plot of density variations produced by two stochastic models. D_c/D_d = 1000 53

3.13 Comparison of density predictions by two types of stochastic models. D_c/D_d = 508 56

3.14 Comparison of density predictions by two types of stochastic models. D_c/D_d = 688 57

3.15 Comparison of density predictions by two types of stochastic models. D_c/D_d = 1396 58

3.16 Model predictions of ρ/ρ_o versus α for test A from Table 3.1 ...61

3.17 Effect of a variable droplet spectrum on the density predictions by a straightline model. D_c/D_d = 934 62

3.18 Comparison of density predictions from a 2-D model with those from a 3-D model. D_c/D_d = 1000 64

4.1 Horizontal layout of FROST tunnel and its essential components .67

4.2 Variation of film density with position on the film. The pen displacement is proportional to the film darkness 76

5.1a Densitometer trace for test #1 98

5.1b Densitometer trace for test #2 99

5.1c Densitometer trace for test #3 100

5.1d Densitometer trace for test #4 101

5.1e Densitometer trace for test #5 102

5.2a Comparison between experiment and several models at test condition #1 103

5.2b Comparison between experiment and several models at test condition #2 104

5.2c Comparison between experiment and several models at test condition #3 105

5.2d Comparison between experiment and several models at test condition #4 106

5.2e Comparison between experiment and several models at test condition #5 107

5.3 Areas (denoted by x) on the ice sample images from which densities were obtained 108

5.4a Comparison between Prodi's results and the stochastic models at test condition I from Table 5.4 113

5.4b Comparison between Prodi's results and the stochastic models at test condition II from Table 5.4 114

5.4c Comparison between Prodi's results and the stochastic models at test condition III from Table 5.4 115

5.5 Curve fit for several straightline model predictions 118

List of Plates

Plate		Page
1.1	Ice accretion produced in an icing wind tunnel at conditions of Figure 1.1(a)	5
4.1	A sledge microtome	70
4.2	A Kristalloflex 2H X-ray generator with lead-lined box	73
4.3	A double-beam recording microdensitometer - model MK III C S	74
4.4	Positioning of X-ray film with respect to the X-ray tube	81
5.1	Cross-section of ice accretions produced at U_∞ = 10 m/s and T_a = -15 °C	85
5.2	Cross-section of ice accretions produced at U_∞ = 20 m/s and T_a = -15 °C	86
5.3	Cross-section of ice accretions produced at U_∞ = 30 m/s and T_a = -15 °C	87
5.4	Ice accretions from tests 1-3 in Table 4.1	96
5.5	Ice accretions from tests 4 and 5 in Table 4.1	97

Nomenclature

A_d	projected area of droplet	$[m^2]$
a	acceleration	$[m/s^2]$
C	concentration of droplets	
C_D	coefficient of drag	
D_o, D_a, D_b	film densities	
D_c, D_d	diameter of cylinder, droplet	[m]
E_m	overall collision efficiency	
F	force	[N]
G_j	local collision efficieny	
K	inertia of droplet	
LWC	liquid water content	$[g/m^3]$
m_d, m_j	mass of droplet	[kg]
MVD	median volume diameter	[m]
P_a	air pressure	$[N/m^2]$
PF	packing factor	
R	gas constant	[J/kg·°K]
r, R_d, r_j	radius of droplet	[m]
R_c	radius of cylinder	[m]
Re	Reynolds number	
S_i	sectors	
T, T_a	air temperature	[°C]
T_o, T_{su}	local surface temperatures	[°C]
T_s	average surface temperature	[°C]
T_1, T_2, T_3	droplet trajectories	
t	time	[s]
U_∞	freestream velocity	[m/s]
u_x, u_y	components of air velocity	[m/s]

V	droplet velocity	[m/s]
V_1	normalized droplet velocity at stagnation point	
v_x, v_y	components of droplet velocity	[m/s]
W	gravitational force	[N]
X_o, X_a, X_b	densitometer pen displacement	[mm]
x_s, Y_r, y_s	arbitrary initial droplet distances	
Y_1, Y_m	limiting droplet distance	
α, α_m	droplet impact angle	[degrees]
ζ, ψ	growth angles of rime feathers	[degrees]
η_a	air viscosity	[kg/m•s]
θ	angular position	[degrees]
θ_m	maximum impingement angle	[degrees]
$\rho, \rho_o, \rho_h, \rho_i, \rho_j$	ice densities	[kg/m^3]
ρ_a	air density	[kg/m^3]
ρ_w	water density	[kg/m^3]
v_o	velocity of droplet at stagnation point	[m/s]
v_r	normal component of droplet impact velocity	[m/s]
χ	angle of approach of droplets	[degrees]

1. INTRODUCTION

Atmospheric icing refers to the freezing of supercooled water droplets onto a surface whose temperature is near or below 0 °C. The continuous accretion of frozen droplets onto a structure would produce a load that could result in a failure of the structure.

Helicopters are especially prone to icing conditions when they fly through clouds at low altitudes. Specifically, the rotor blades may collect ice and if the thickness and shape of the accretion is right, the aerodynamic performance of the vehicle would degrade. More importantly, if during the flight the ice cracks and separates from the blades, the flying projectiles may make impacts with the craft itself, thereby endangering it and its occupants. Transmission lines and ships are also susceptible to icing problems when they operate in environments where the temperature drops below 0 °C.

Once formed on a structure, ice is a good adhesive. From an engineer's point of view, in the case of a helicopter, it would be desirable to design a de-icer system that would be capable of separating ice from the rotor blades as completely and as safely as possible.

The present goal for researchers in the field of atmospheric icing is to predict the ice loads on arbitrary structures, given the meteorological conditions. This is extremely difficult and requires the development of a physical model to describe the icing process.

Studies on icing began when scientists in the field of meteorology decided to measure the growth rate of hailstones, as they fell through

a cloud of supercooled droplets, and relate them to the properties of the cloud droplet spectra. Of note, Dolozell, Cunningham, and Katz (1946) exposed rotating cylinders to supercooled clouds to measure its liquid water concentration, and even to provide some information about the drop-size distribution. Tribus et al. (1948) applied the principles of dimensionless similarity and used experimental models to solve the differential equations of motion for a droplet. This provided a way of relating results from scale models to those of the prototypes. Later, Ludlam (1951) determined that the rate of ice accumulation on a hailstone was dependent on the heat balance at the surface of the hailstone. He used a cylinder to show this and, in effect, pioneered the history of the evolution of modelling efforts in icing research when he created a model for the icing of a rotating cylinder. Then, Messinger (1953) discovered that under certain flow conditions, not all of the impinging liquid freezes in the impingement region. This finding led to the classification of atmospheric icing into two regimes: wet (surface temperature is near 0 °C), and dry (surface temperature is below 0 °C) icing.

Ludlam discovered that his work could be extended to any situation where there is a relative movement between water droplets and an object. Since then, various people have formulated icing models that are specific to their fields of interest. For example, there are models by Lozowski and d'Amours (1980) for hail, Lozowski and Oleskiw (1981) for airfoils, Stallabrass (1980) for fishing trawlers, and McComber (1982) for power lines.

The previous models used cylinder icing as an initial estimate of icing effects to relate to the actual icing effects. Lozowski,

Stallabrass, and Hearty (1983) have extended the model for a non-rotating cylinder to allow for the dependence of icing on the angle around the cylinder for all icing conditions. With this icing model, Lozowski et al. (1983) attempted to predict ice shapes on cylinders at various icing wind tunnel conditions. Figure 1.1 shows how the model predictions compare with actual accretion shapes at three different liquid water contents, while U_∞ = 10 m/s, T_a = -10 °C, and MVD = 130 μm. The model predictions were not in good agreement with measurements under wet icing conditions. Under rime icing conditions, however, the model predictions were in closer agreement with the measurements. In the latter case (Figure 1.1(a)), the general discrepancies between the model predictions and the actual accretion occurred near the edges of the accretion. Closer examination of the sample grown in the tunnel showed that there were some "feathery" structures at the edge of the deposit. In the area of the stagnation line, the ice appeared greyish, indicating a relatively denser ice than that observed at the edge of the accretion. These features are clearly shown in Plate 1.1.

An assumption made in the Lozowski et al. model is that the density of ice is everywhere a constant and equal to 890 kg/m^3. Essentially this model, and all other existing models, ignore the details of droplet impacts completely and rather does an energy balance for a control volume. They are concerned with averaged droplet properties and effects.

Bain and Gayet (1983) and Finstad (1986) incorporated density variations into Lozowski's model and demonstrated that the dependence of ice accretion shape on the ice density was important. The resulting accretion shape, produced with Bain and Gayet's formulation for density

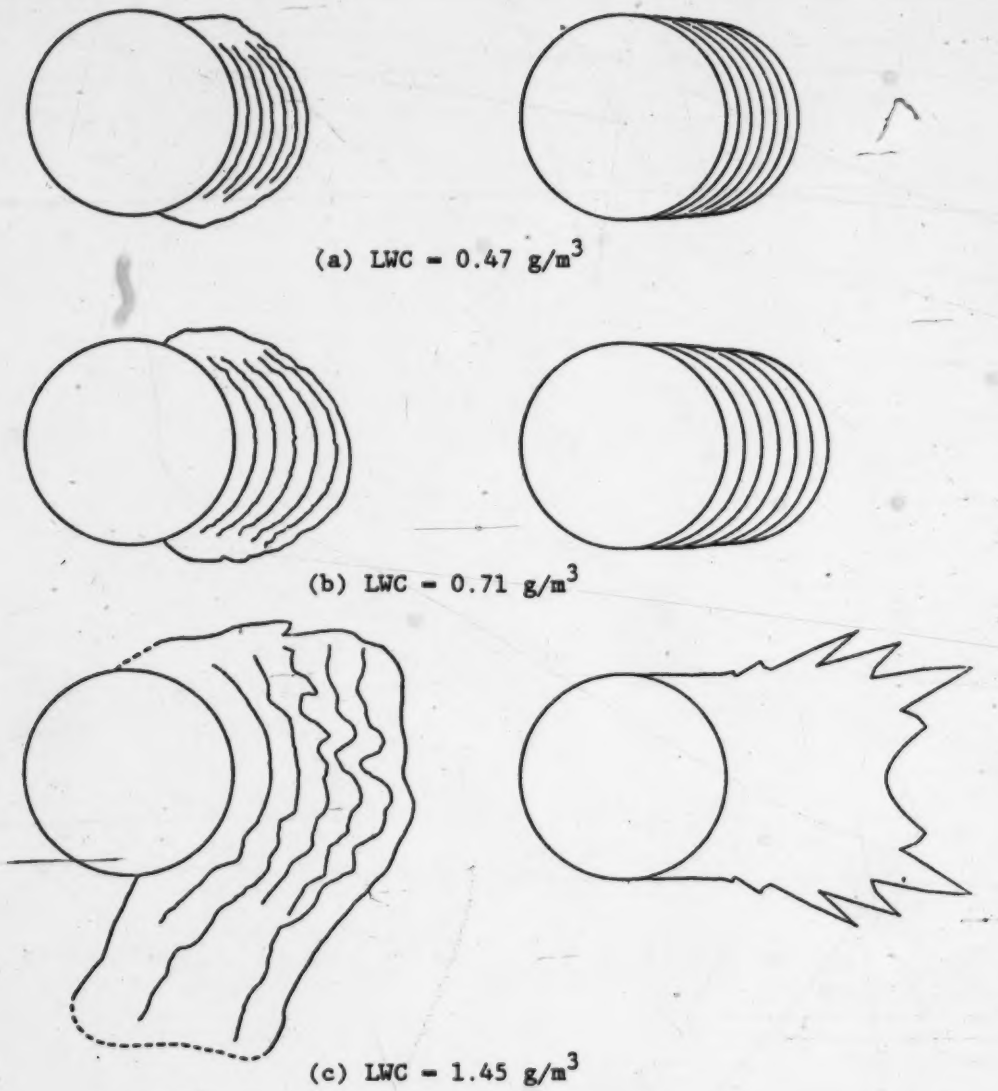

Figure 1.1 Comparison of ice accretion shape predictions from the model of Lozowski et al. (1983) with actual accretion shapes. U_∞ = 10 m/s, T_a = -10 °C, MVD = 130 μm.

Plate 1.1 Ice accretion produced in an icing wind tunnel at conditions of Figure 1.1(a).

variation along the cylinder surface, was an improvement over the original model but the predicted ice shapes were again elliptical and failed to account for the discrepancies at the accretion edges. A brief description of Bain and Gayet's model is provided in Chapter 5. Finstad, however, had more success in predicting the shape of the actual ice accretion. This is shown in Figure 1.2. Her results suggest that existing models require some empirical correlation for the density variation. This would be straightforward for a wet icing model where the density would be a maximum and equal to some constant everywhere on the ice accretion. In deposits grown under rime icing conditions, the ice density can vary from 80 to 900 kg/m^3, according to Macklin (1962).

Although providing a density correlation for the model of Lozowski et al. may improve on its accretion shape predictions, it should be cautioned that two ice accretions having different appearances in color and texture may have similar densities (Macklin, 1962). Therefore, it is not enough to assume a density variation in Lozowski's model. The presence of feathers in the actual accretion shows that, in these areas, the actual details of single droplet impacts may have to be taken into consideration to adequately describe the resulting accretion characteristics. As long as the droplets were smeared onto the deposit, as in Lozowski's model, air pockets cannot be created within the structure and consequently, the size of the ice would always be underestimated. This macroscopic approach would seem to work in regions where droplet impacts are sufficiently frequent. At the edges, however, the impacts are infrequent and a stochastic approach would be more appropriate. Therefore, further improvement of Lozowski's icing model

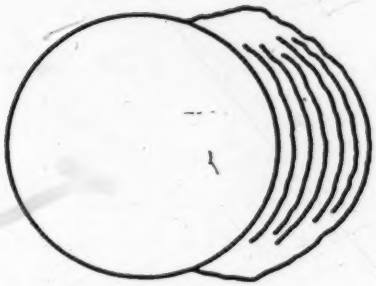

(a) actual accretion

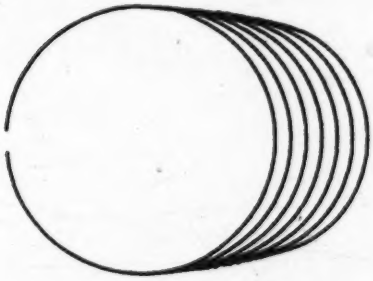

(b) model of Lozowski et al. (1983)

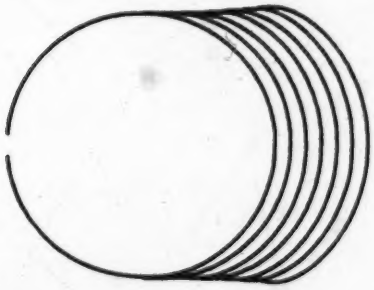

(c) model of Finstad (1986)

Figure 1.2 Comparison of accretion shapes produced by various models. D_c/D_d = 508, U_∞ = 10.7 m/s, T_a = -10 °C, and LWC = 0.48g/m^3.

could be achieved if the shape of the water droplets following impact with the cylinder is taken into consideration. The droplet shapes would depend on the icing conditions. Macklin (1962) found that the degree of droplet spreading depends largely on the impact momentum of the droplets and the heat balance at the icing surface.

The freezing process of the droplet is complicated and is affected by various properties of the airflow, the icing object, and the impinging water drops. In general, upon impact with the icing surface, the droplets freeze and liberate heat. The heat is transferred to the droplet's environment primarily by convection/evaporation into the airstream and conduction into the icing object. The latter has a warming effect on the icing surface.

Fraser, Rush and Baxter (1952) found that during an ice accretion process, rime ice forms whenever the temperature of the icing surface is below 0 °C. This is referred to as a dry-growth condition in which each droplet freezes completely before another droplet collides with it. An accretion built in this fashion usually traps air within the structure and has a whitish appearance. An extreme case of rime icing occurs when the icing surface temperature and the droplet impact velocities are moderately low. Under these conditions, the droplets not only freeze individually but tend to remain spherical following impact with a surface (Macklin, 1962). In 1983, Lozowski introduced a Monte Carlo simulation to observe the effects of single droplet impacts on a surface. In the model, solid spheres were collected on a single frozen droplet; this produced an open structure having low density. This stochastic model provides a link to the present study, because the approach could be extended to model an entire accretion.

The purpose of this research, then, is to devise a stochastic rime icing model that would provide a method of analyzing the microscopic details in a rime ice structure. The model would hopefully explain the nature of the accretion processes that occur around the edges of a rime ice deposit on a cylinder.

2. DESCRIPTION OF STOCHASTIC RIME ICING MODELS

2.1 Presentation of the Models

A stochastic model is one that enables water droplets to be admitted into the flow and collect on a surface one at a time. In the ensuing two sections, the method of construction of the straightline and the curved trajectory models will be given in detail, with the former provided first because of its simplicity. The basic features of the stochastic models will then be pointed out to complete the presentation.

2.1.1 The Straightline Trajectory Model

The three basic steps for the development of a simple two-dimensional stochastic model are shown in Figure 2.1. In the model, a droplet of a predetermined size is, first, introduced at an arbitrary vertical distance, Y_r, from the stagnation line. The distance is determined by a random number generator. Then, the droplet follows a straight line path until it collides with the surface of a cylinder. At the point of impact, the droplet is assumed to freeze as a rigid cylinder. By repeating this procedure for numerous equal-sized droplets, a two-dimensional rime accretion could be formed. The model was produced under the added assumptions that the gravitational effect was omitted and the accretion was symmetric with respect to the stagnation line. This assumption is reasonable for rime icing conditions in which water runback is minimal. A listing of a program for a straightline trajectory model is provided in Appendix 1.

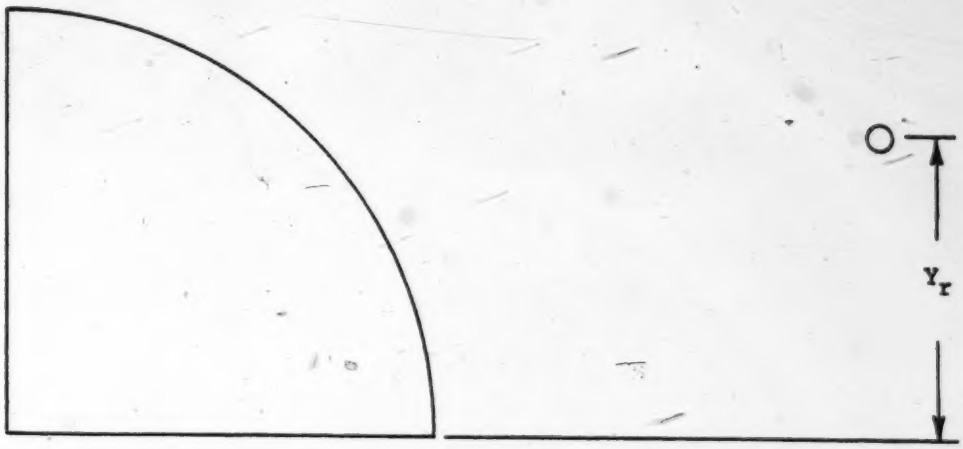

(a) droplet introduced

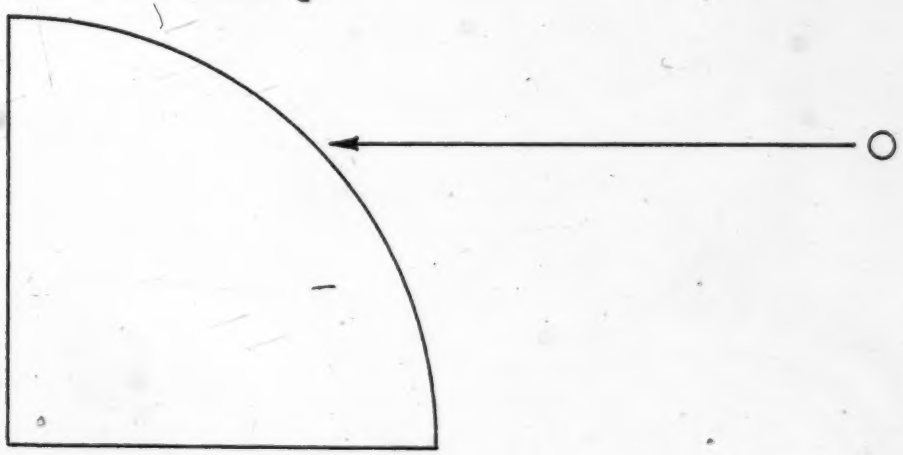

(b) droplet follows straight line path

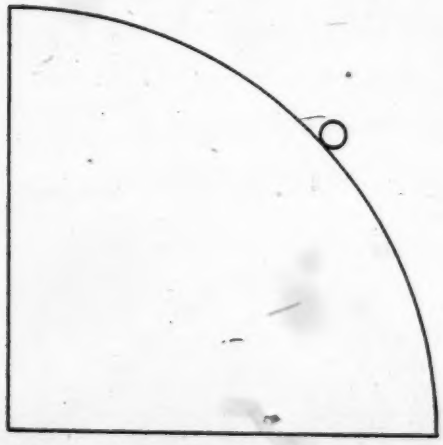

(c) droplet makes an impingement and remains spherical

Figure 2.1 Basic steps in a straightline model.

2.1.2 The Curved Trajectory Model

The curved trajectory model is produced in a similar fashion to the straightline model, only the droplets follow curved paths. The curvature of the droplet's trajectory is calculated by solving the equations of motion for the droplet in an airstream. The extensive calculations are shown in Appendix 2. This involve the reduction of the general equations to the following first order differential equations,

$$K \frac{dv_x}{dt} = \frac{C_D Re}{24} (u_x - v_x) \qquad (2.1.1)$$

$$K \frac{dv_y}{dt} = \frac{C_D Re}{24} (u_y - v_y) \qquad (2.1.2)$$

$$\frac{dx}{dt} = v_x \qquad (2.1.3)$$

$$\frac{dy}{dt} = v_y \qquad (2.1.4)$$

All variables are dimensionless with respect to flow parameters as indicated by equations (A.2.6) to (A.2.8) in Appendix 2. The inertia parameter, K, measures the ease with which a droplet may deflect away from the substrate. The Reynolds number, Re, represents the ratio of inertia forces to friction forces, and the drag coefficient, C_D, is the ratio of total drag to the dynamic pressure. All three dimensionless parameters depend on the flow conditions, and for incompressible flow, C_D is a function only of Re (Schlichting, 1979), as shown in Figure 2.2. For instance, when the flow conditions are such that the friction forces exerted by the airstream on the droplet are large compared to

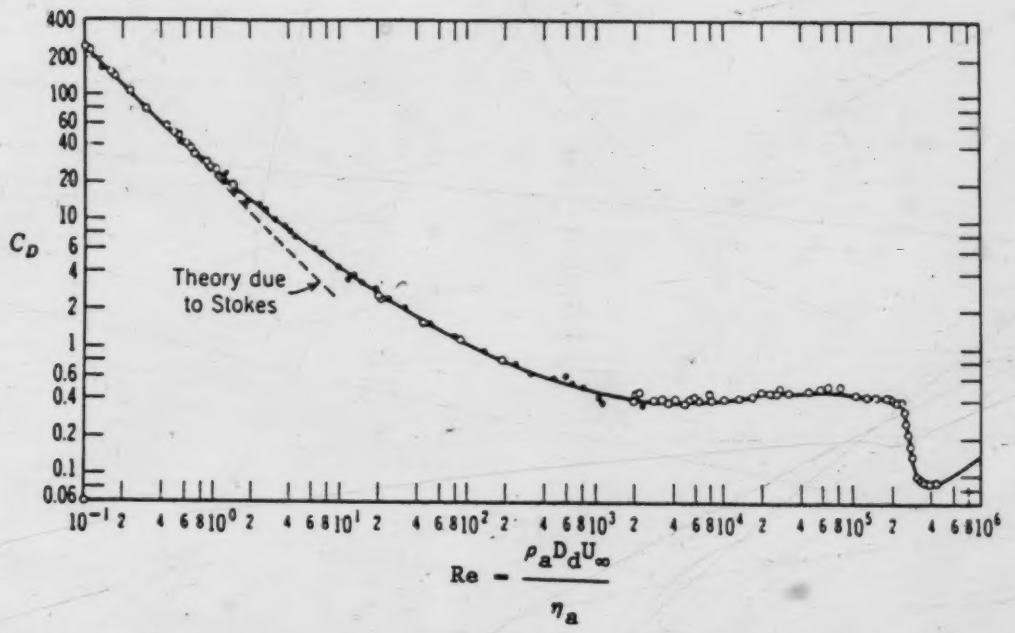

Figure 2.2 Drag coefficient of a sphere as a function of Reynolds number (Schlichting, 1979).

the droplet's inertia, the Re is small and the drag forces on the droplet is large. This causes droplets to be easily deflected away from the substrate and follow the streamlines. When the inertia forces are large compared to friction forces, however, Re is large and C_D is small. Because of the reduced drag on the droplet, their trajectories cannot be easily changed and the droplets tend to make impacts on the structure. Other variables in the above equations include the u_x and u_y, which are the air speeds in the x and y directions, and v_x and v_y, which are the droplet speeds in the x and y directions. Finally, x and y represent the coordinate of the droplet's location. The formulas for the calculation of K, C_D, and Re are given in Appendix 2. Appendix 3 shows how u_x and u_y could be obtained from the theory of potential flow past a right circular cylinder. The above four equations have four unknowns (v_x, v_y, x, and y) and are solved with a 4-th order Runge-Kutta numerical technique. The method is given in detail in Appendix 2.

Once the droplet's trajectory is determined, the accretion is built in a manner similar to that in the simple model. Droplets are released into the flow at $x = 10\ D_c$ and $y = Y_r$ with $v_x = 0$ and $v_y = 0$. It should be pointed out that the simple model is involved with basically one variable - the cylinder-to-droplet diameter ratio, D_c/D_d. In the curved trajectory model, however, there is an additional variable - the freestream velocity. A listing of a program for the curved trajectory model is provided in Appendix 5.

2.2 Implementation of the Curved Trajectory Model

The curved trajectory model is expensive to execute because the instantaneous location of the approaching droplet is calculated with an iterative technique. Also, the location is referenced to the positions of every accreted droplet to determine where and when the oncoming droplet makes a collision. To render the model more cost-efficient, there are several ways of reducing the number of iterations required in the calculations.

One, the area bounded by the cylinder surface, the limiting trajectory (trajectory corresponding to θ_m, defined in Section 3.1), the stagnation line, and the line $x = 10D_c$ is split up into five bands. The boundaries of the bands are given by the droplet trajectories with starting positions of $x = 10D_c$ and $y = 0.0$, $0.2Y_1$, $0.4Y_1$, $0.6Y_1$, $0.8Y_1$, and Y_1. Following the introduction of a droplet 'A' into the flow, rather than determining which droplet in the accretion it will collide with, only the droplets within the band that droplet A enters will be considered.

A second cost-saving feature is utilized to determine where droplet A would make a collision. This method involves the elimination of the iterative droplet trajectory calculations in favour of an interpolation technique, as illustrated in Figure 2.3. Within the band, any droplet having a c/d value within a certain tolerance of a/b is assumed to be within the path of the oncoming droplet. Among these droplets, only the outermost droplet will be impacted upon. i.e. the one with the greatest $|x_d|$. Calculation of the final position of the impinging droplet (x_d, y_d) involves the satisfaction of the assumptions $c/d = a/b$ and $(2R)^2 = (x_1 - x_d)^2 + (y_1 - y_d)^2$.

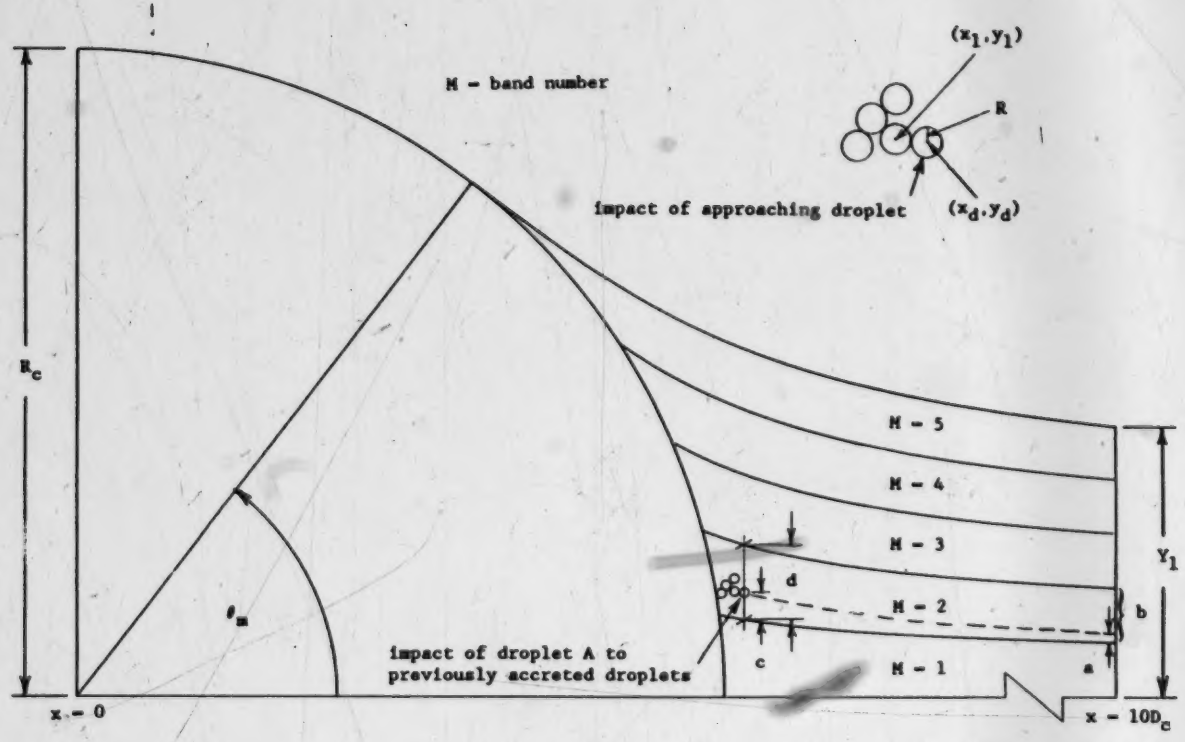

Figure 2.3 Method of interpolation applied in the curved trajectory model.

To execute the curved trajectory model, one would be required to, first, select the appropriate flow conditions D_c, D_d, U_∞, and T_a. Then, the corresponding Y_1 is calculated by trial and error from the program in Appendix 4 as follows: Try increasing values for y_s, and determine when the droplet barely collides or misses the cylinder. The droplet makes an impingement if the nearest iteration is printed. Otherwise, the droplet is shed in the airstream, and the nearest thousand iterations is printed. Once $y_s = Y_1$ is found, it (YMAX), along with the flow parameters, must be supplied to the curved trajectory model. The model is then executed with the commands in Appendix 5.

2.3 Stochastic Model Features

Figure 2.4 illustrates an example of a stochastic model produced with straightline trajectories. Since gravitational effects are ignored, the stochastic models are assumed to produce symmetric accretions and, thus, only a quarter cylinder will be shown in the models. A careful examination of the accretion shows that there are two interesting features of a stochastic model. One is that discrete structures have grown along the edges of the accretion. These structures seem to have preferred growth directions and could represent two-dimensional rime feathers. Measurements of the growth angles could be obtained readily and compared with those from actual accretions.

A second feature of the model is its tendency to trap air within the structure. By examining the area occupied by the droplets, one can obtain an estimate of the local droplet concentration. This is not the case in the models of Lozowski et al. and Bain & Gayet for they

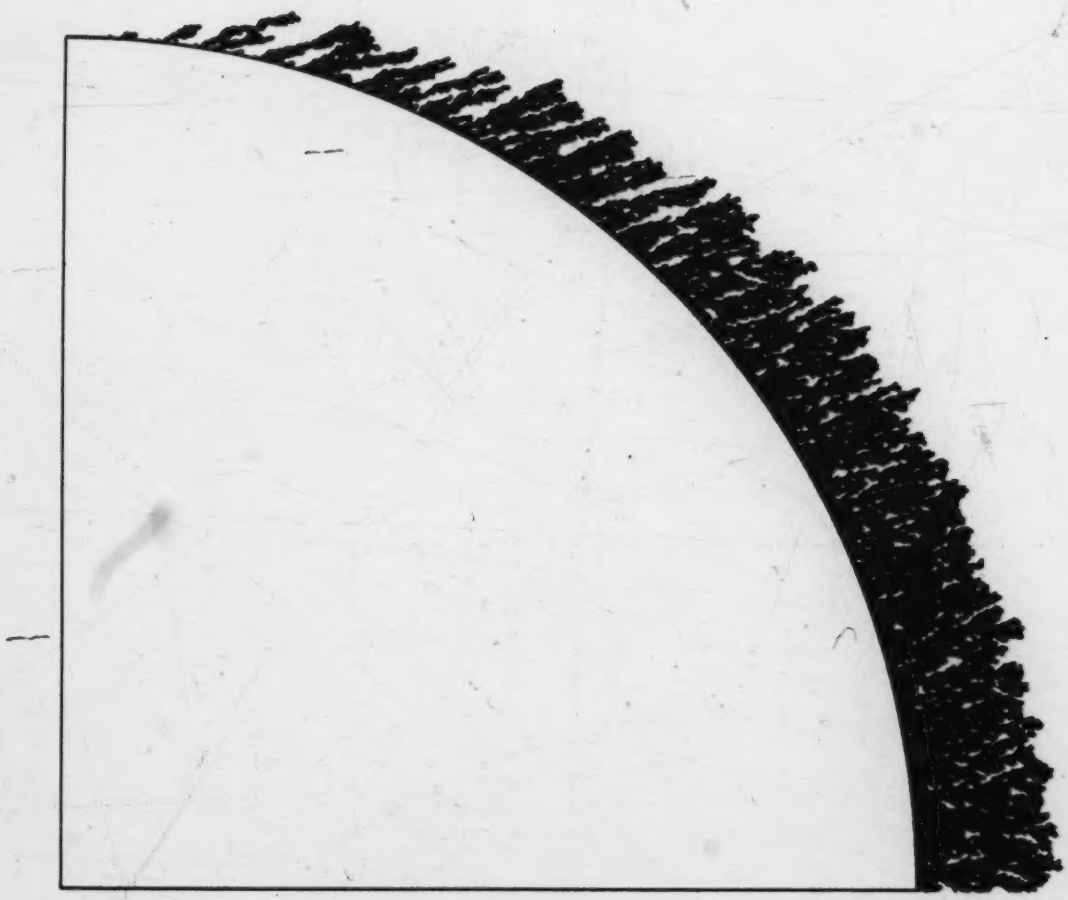

Figure 2.4 A straightline model produced by collecting 20,000 droplets on a cylinder. D_c/D_d = 1000.

require some empirical correlation for ice density. In the present models, the packing factor of the droplets in an annular area adjacent to the cylinder surface can be obtained and compared to the local ice density measurements on actual accretions. Appendix 6 provides the technique for the calculation of droplet concentration at every 5°-sector relative to the forward stagnation line. This practice will be employed in the present study, and droplet concentrations are plotted against the angular position of the midpoints of each sector.

At this time, it is important to acknowledge why the icing object will be limited to having a cylindrical form. Firstly, many structures often affected by atmospheric icing have a cylindrical shape. Secondly, the potential flow field, which affects both the droplet impact speed and the heat transfer to the airstream, is easily determined around a cylinder. This is not so with a real viscous flow field.

Another assumption made in the models is that each droplet remains cylindrical on impact with another droplet or the cylinder. In actual accretions, Macklin (1962) deduced that droplets are able to freeze spherically when the parameter $(-rv_o/T_s)$ is less than ten, where r is the median volume radius of the droplet spectrum in μm; T_s is the mean temperature of the icing surface in °C; and v_o is the droplet impact velocity at the stagnation point in m/s. Low surface temperatures would shorten the droplet's freezing time, while a reduction of the droplet's impact speed and size would minimize droplet spreading activity. Therefore, comparisons between the rime icing model and the actual ice accretions could be performed only under these flow conditions.

3. MODEL PREDICTIONS AND DISCUSSION

Figure 3.1 illustrates an example of an accretion produced by the stochastic model with straight line trajectories. It is important to note that there are two unique characteristics of a stochastic model. The model predicts the development of two-dimensional feathers and provides a method for obtaining an initial estimate for local droplet concentration. These two features are examined closely under separate section headings in this chapter: rime feathers and local droplet concentration. In both sections, there is a presentation of each stochastic model's predictions. Comparisons between model predictions will be made and this will be aided with a detailed analysis of the accretion processes that occur in the stochastic models. The chapter is intended to point out the physical similarities between the models, and to explain how the models consistently produce feathers and air inclusions.

Before any results from a curved trajectory model are considered in the discussion, however, it must be assured that the trajectories in the model were calculated correctly. Langmuir and Blodgett (1946), hereafter referred to as L & B, have determined several parameters analytically which could be used for comparison with those obtained from the model. The first section deals with this comparison with the view to establishing confidence in the curved trajectory model predictions of feather growth angles and local droplet concentration.

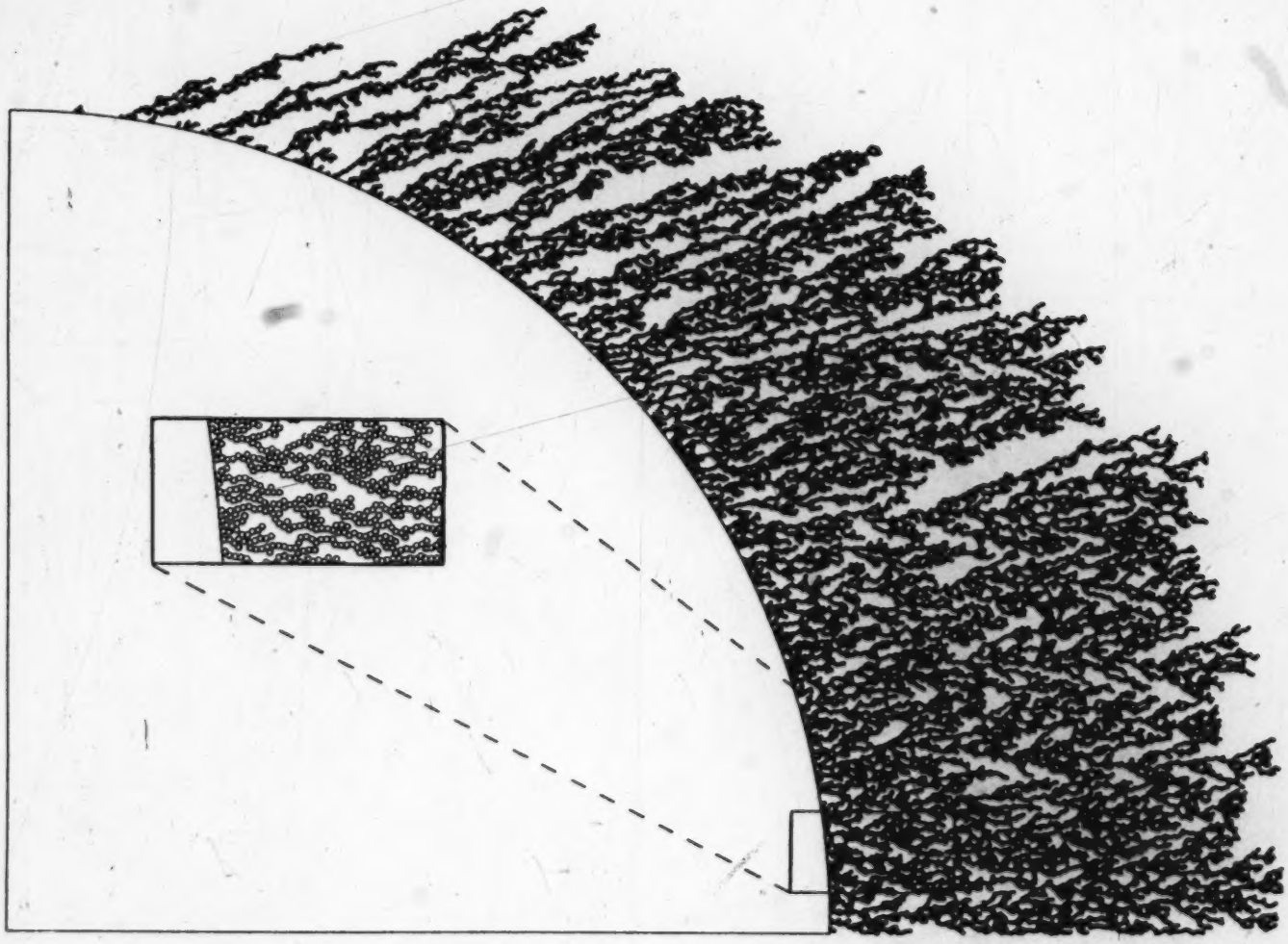

Figure 3.1 A straightline model produced by collecting 20,000 droplets on a cylinder. D_c/D_d = 508.

3.1 Confidence in Curved Trajectory Model Predictions

Researchers in the field of atmospheric icing often encounter two familiar parameters: the maximum impingement angle, θ_m, and the overall collision efficiency, E_m. According to Langmuir and Blodgett, these parameters determine the amount and distribution of ice on a structure and, therefore, having available data on E_m and θ_m would be a valuable asset for relating one ice-modelling situation to another. The two parameters have been calculated analytically by L & B, and have been used as a basis for comparison ever since. This section begins with a definition of E_m and θ_m. Then, the method by which L & B calculated these two parameters will be provided in detail. The section concludes with a comparison of model predictions of E_m and θ_m with those by Langmuir and Blodgett.

Figure 3.2 is a diagram illustrating how E_m and θ_m could be obtained. It can be seen that the calculation of both parameters is dependent on the curvature of the droplet trajectories. For example, E_m is defined as the ratio of the mass flow of water droplets striking the surface to the mass flow that would strike the surface had the droplets not been deflected by the airstream. This definition was provided by Langmuir and Blodgett (1946) and Makkonen (1984). As a direct consequence of the droplet's trajectory curvature, there exists a point on the cylinder surface downstream from which the droplets will not impinge. The angular position of this point is referred to as θ_m. An increase in trajectory curvature would decrease E_m and θ_m. Because the determination of E_m and θ_m relies on the curvature of the trajectories, L & B had to calculate the trajectories before E_m and θ_m could be found.

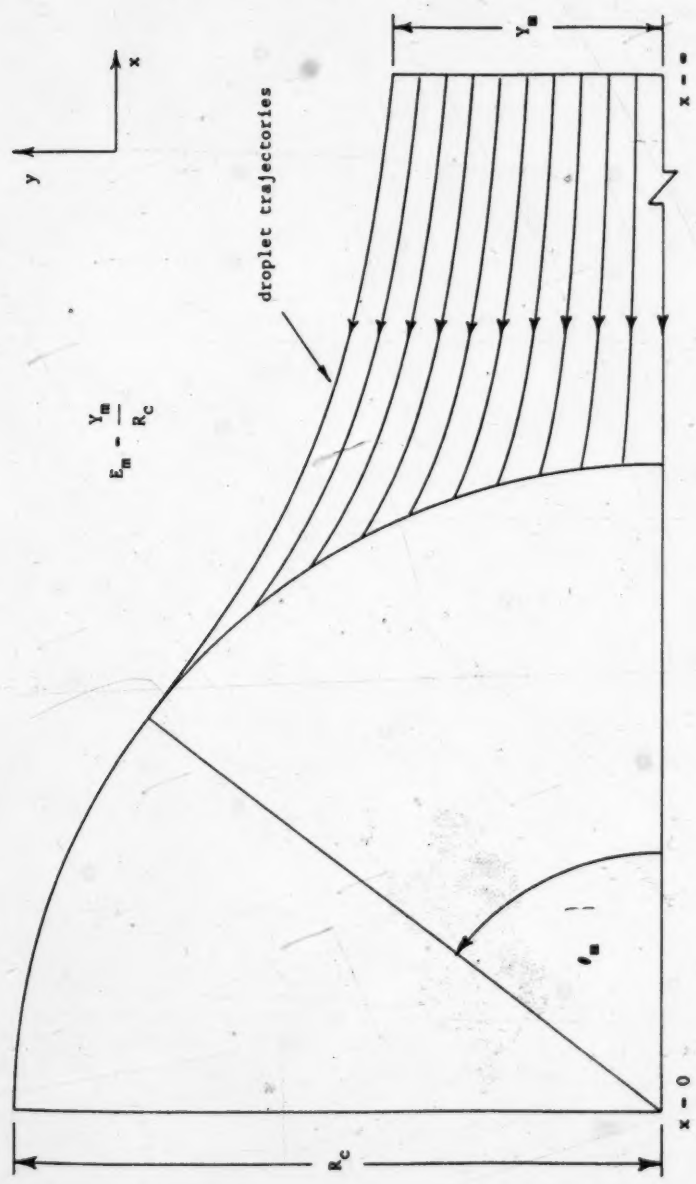

Figure 3.2 Method of calculation of E_m and θ_m by Langmuir & Blodgett (1946).

The approach employed by L & B begins with a conversion of the dimensionless equations of motion of the droplets into the following integral form:

$$v_x = (1/K) \int (u_x - v_x)\, d \int (C_D Re/24) dt + v_{x_1}$$

$$v_y = (1/K) \int (u_y - v_y)\, d \int (C_D Re/24) dt + v_{y_1}$$

$$x = \int v_x dt + x_1$$

$$y = \int v_y dt + y_1$$

where all the variables are as defined in Section 2.1.2, and u represents air velocities. The v_{x_1}, v_{y_1}, x_1, and y_1 are constants of integration.

Then, with a differential analyzer, the equations were solved for the x and y coordinates of the droplet at each time step. By repeating this step-by-step integration procedure for a droplet with an arbitrary initial y distance y_s from the stagnation line, a droplet trajectory is determined and plotted on a trace. A set of three or four droplet paths could be obtained at a given flow condition by using different y_s values. From this set of trajectories, two are selected for interpolation purposes: one barely missing a collision with the cylinder, and one barely making an impingement. The idea is to determine a limiting trajectory, one whose path is tangent to the surface of the cylinder at the point of impact, from these two curves. Once the limiting trajectory is interpolated by the operator of the analyzer, E_m and θ_m can be calculated and measured on the analyzer trace respectively.

In a similar fashion, E_m and θ_m can be obtained for various flow

conditions. The data obtained with the differential analyzer was planned to give families of curves in which the characteristics of the ice deposit, such as E_m and θ_m, are expressed as functions of the inertia parameter, $K = \frac{2\rho_w R_d^2 U_\infty}{9\eta_a R_c}$, and the impingement parameter, $\phi = \frac{18\rho_a^2 R_c U_\infty}{\eta_a \rho_w}$. The ρ_w, R_d, U_∞, η_a, R_c, and ρ_a are the water density, droplet radius, freestream velocity, air viscosity, cylinder radius, and air density respectively. Thus, K and ϕ are calculated from the the flow conditions and, once known, will determine E_m and θ_m. Figures 3.3(a) and 3.3(b) illustrate the family of curves for the data on quantities E_m and θ_m. Figure 3.3(c) is included for use in Chapter 5. The ϕ is a constant along each curve and every K-ϕ combination represents a unique flow condition. With the aid of these curves, we are in a position to compare L & B's calculations of E_m and θ_m with model predictions, to determine if the the trajectory calculations in the model are correct.

The comparison is performed at nine different flow conditions, for a bare cylinder. These conditions are shown in Table 3.1 and represent the range of icing conditions, outlined in next chapter, in which rime feathers could develop in the icing wind tunnel. A sample calculation of K and ϕ for test condition A is provided in Appendix 7.

In the curved trajectory model, the E_m and θ_m values are calculated as follows: A droplet is released into the flow, with zero initial velocity, at an arbitrary initial distance of ten cylinder diameters away from the center of the cylinder in the x-direction ($x_s = 10D_c$), and an arbitrary y distance from the stagnation line ($y_s = Y_r$). Then, the droplet's trajectory is calculated using the 4-th

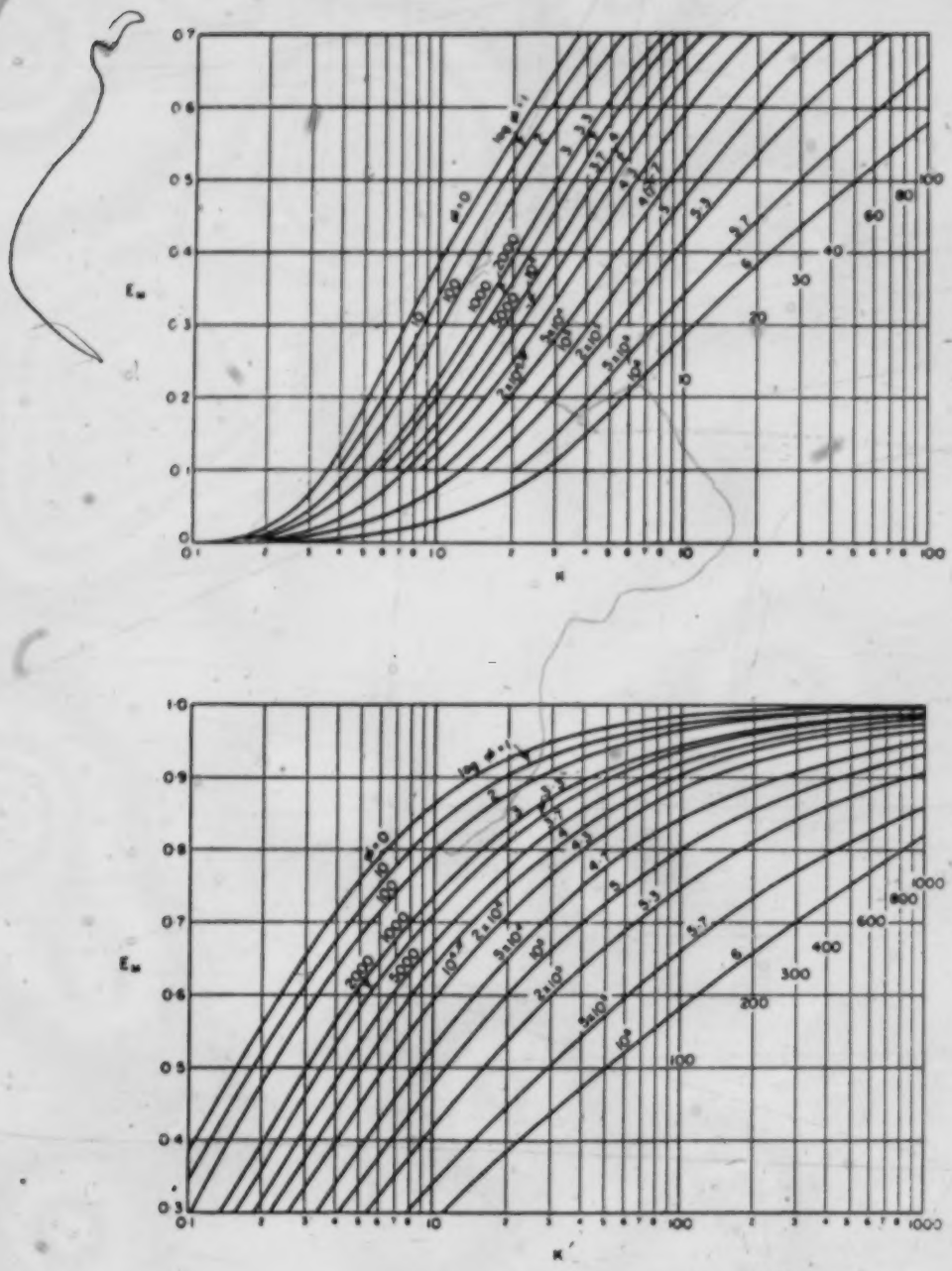

Figure 3.3(a) Family of curves obtained by a differential analyzer for the determination of E_m at any flow condition (Langmuir & Blodgett, 1946).

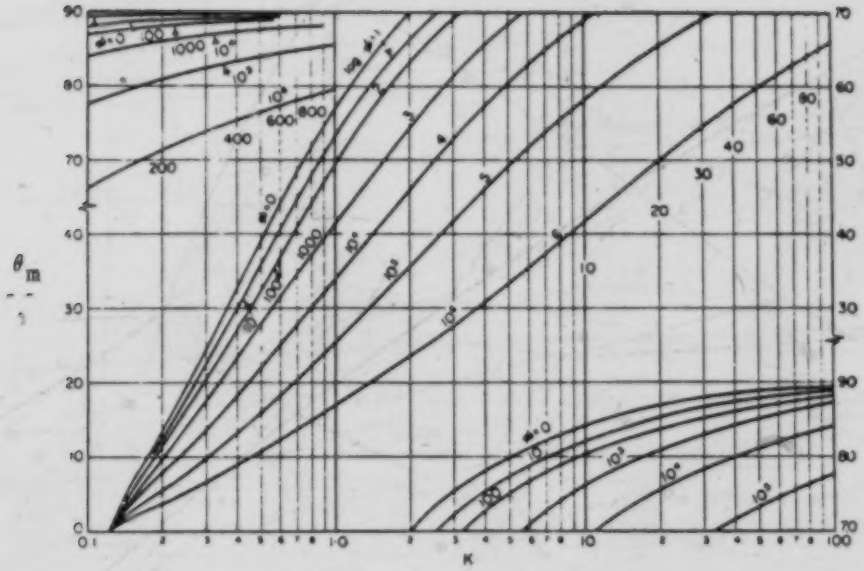

Figure 3.3(b) Family of curves obtained by a differential analyzer for the determination of θ_m at any flow condition (Langmuir & Blodgett, 1946).

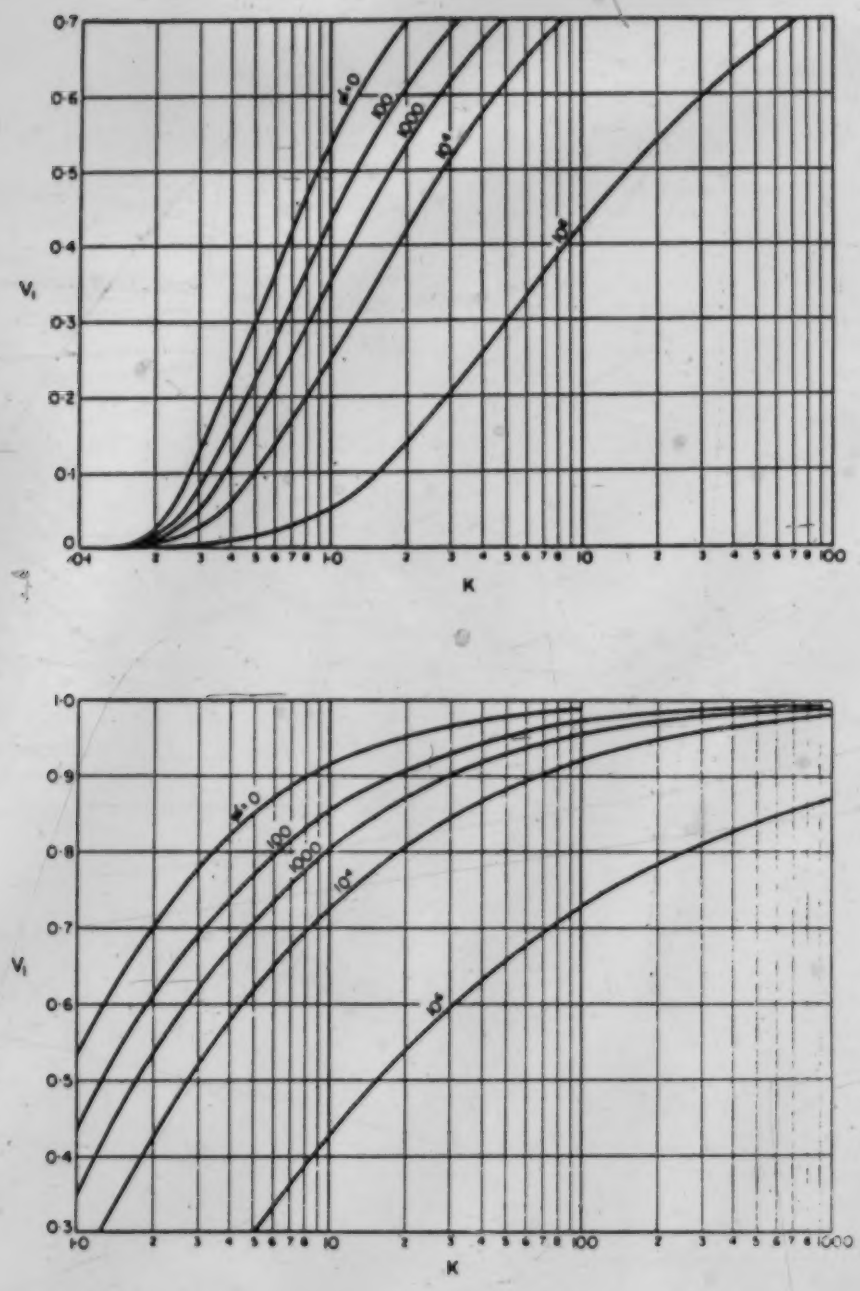

Figure 3.3(c) Family of curves obtained by a differential analyzer for the determination of V_1 at any flow condition (Langmuir & Blodgett, 1946).

Table 3.1 Presentation of θ_m and E_m values calculated by Langmuir & Blodgett (1946) and the curved trajectory model for a bare cylinder. D_c = 2.54 cm.

	CONDITIONS						L & B		MODEL	
Test #	D_d (μm)	U_∞ (m/s)	T_a (°C)	P_a (N/m^2)	K	ϕ	θ_m (°)	E_m	θ_m (°)	E_m
	(1)	(2)	(3)	(4)	(5)	(6)	(7)	(8)	(9)	(10)
A	18.2	10	-15	100,000	0.89	255	45.0	0.26	45.5	0.26
B	27.2	10	-15	100,000	1.94	255	59.7	0.46	59.9	0.46
C	36.9	10	-15	100,000	3.57	255	68.1	0.60	68.7	0.60
D	17.4	20	-15	100,000	1.59	480	54.9	0.39	54.3	0.39
E	30.3	20	-15	100,000	4.81	480	70.2	0.64	72.6	0.66
F	36.4	20	-15	100,000	6.95	480	73.9	0.71	76.7	0.74
G	17.7	30	-15	100,000	2.46	720	60.9	0.48	62.3	0.49
H	27.3	30	-15	100,000	5.86	720	71.5	0.66	74.7	0.70
I	32.4	30	-15	100,000	8.26	720	74.7	0.72	78.3	0.76

order Runge-Kutta numerical method, outline in Appendix 2. The procedure is repeated for various y_s until a limiting trajectory is found. In this case, the y_s is stored as Y_1; the trajectory is plotted; consequently, E_m and θ_m are calculated as defined in Figure 3.2, only $Y_m - Y_1$ in the model. The limiting trajectories for all the conditions in Table 3.1 are calculated in this manner and the results for θ_m and E_m are tabulated in columns (9) and (10) respectively in the table. L & B's results are listed in columns (7) and (8).

The agreement between L & B and model results for E_m and θ_m are conveniently illustrated in Figures 3.4(a) and 3.4(b). In each plot, any point lying on the 45° line represents a good agreement between the two methods of calculation of the appropriate parameter in the plot. Any point located to the left of the line indicates an underestimation by the model, whereas those appearing to the right of the line translates into an overprediction by the model.

In particular, let us examine Figure 3.4(a), 3.4(b), and Table 3.1 to investigate how model predictions of E_m and θ_m compare with those calculated by L & B. It was observed that for cases where K was less than or equal to 3.5, both methods predicted a similar value for E_m and θ_m. With larger K values, the model overestimated L & B's calculation by 5%. The inertia parameter seems to have an effect on the accuracy of the calculation of E_m and θ_m. One reason for this was that all the droplets were released at $x_s = 10D_c$ in the model rather than at $x_s = \infty$ - this was necessary to lower the computing costs by reducing the number of extensive trajectory calculations in the model. The instantaneous drag and inertial forces on the droplet highly depends on where the droplet was initially released into the flow, and on the

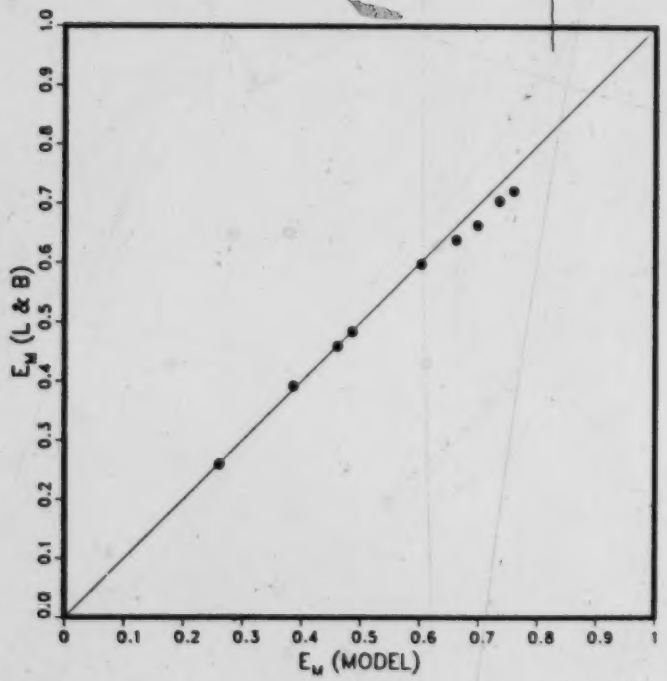

(a)

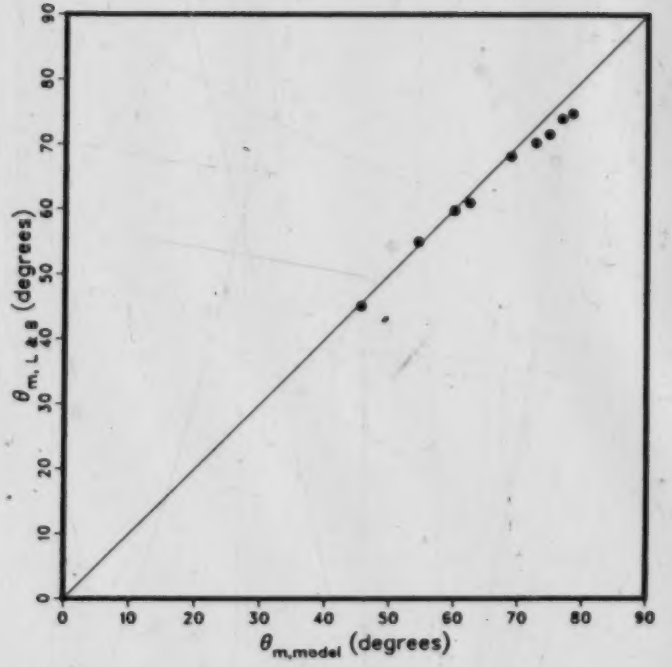

(b)

Figure 3.4 Comparison of (a) E_m and (b) θ_m from the curved trajectory model with those from the curves of Langmuir and Blodgett (1946).

droplet size. L & B realized this and provided a correction to the initial droplet velocity, which effectively releases droplets at $x_s = \infty$. This could have been done in the model, but it was omitted because the error, in doing otherwise, was found to be small. A second reason is that L & B used equation (A.2.23) from Appendix 2 to obtain $C_D Re/24$ for all Re, whereas the model used equations (A.2.20) to (A.2.23), depending on the value for Re.

The two factors contribute to the inaccuracy of the model predictions of E_m and θ_m, but since they are within 5% of L & B's calculations, confidence in the curved trajectory model has been established. Therefore, comparisons between the straightline and curved trajectory model predictions could be made. The next two sections will do this, beginning with a comparison of rime feather growth directions.

3.2 Rime Feathers

Rime feathers are discrete structures with preferred growth directions on ice accretions. The angle of growth of the feathers, ψ, measured relative to the stagnation line as shown in Figure 3.1, influences the drag properties of the entire icing structure. Accurate stochastic model predictions of ψ is important if this result is to be used in models such as that of Lozowski et al. (1983) to produce accurate ice shapes near the edges of the accretion. Therefore, it is desirable to measure these angles from a stochastic model and tabulate them for comparison purposes.

The ability to produce feathers on an icing structure is a credit to the construction of the stochastic models. This section

investigates the manner in which an accretion is built on a two-dimensional cylinder to determine how feathers are formed; it will help explain why they are likely to appear near the edges of an accumulation in the model. Then, based on comparisons between each stochastic model's predictions, the influence of various flow parameters on the growth angles of feathers will be described thoroughly.

3.2.1 Mechanisms for Feather-Growth

Model accretions were produced at nine sets of flow conditions in order to examine the properties of feathers more closely. These conditions are identical to those in Table 3.1 for convenience. At each set of conditions, two accretions were built: one with droplets having straightline trajectories and the other with droplets following curved paths. At the completion of each test, each model was examined and found to exhibit feather development in the vicinity of the edge of the accretions. A reason why feathers consistently appear at the edges of a model accretion is directly related to the impact angle of the impinging droplets, α. The α is defined as the angle between the surface normal and the tangent of a trajectory at the point of impact; it determines whether feathers would form or not.

Figure 3.5 defines α diagrammatically and shows how it could influence feather growth for the straightline trajectory case. Basically, as the droplets accrete on one another, the resulting droplet structure grows in the upstream direction. The feathers have a tendency to originate at some point on the surface of the cylinder and develop into a two-dimensional cone-shaped structure, the head of which

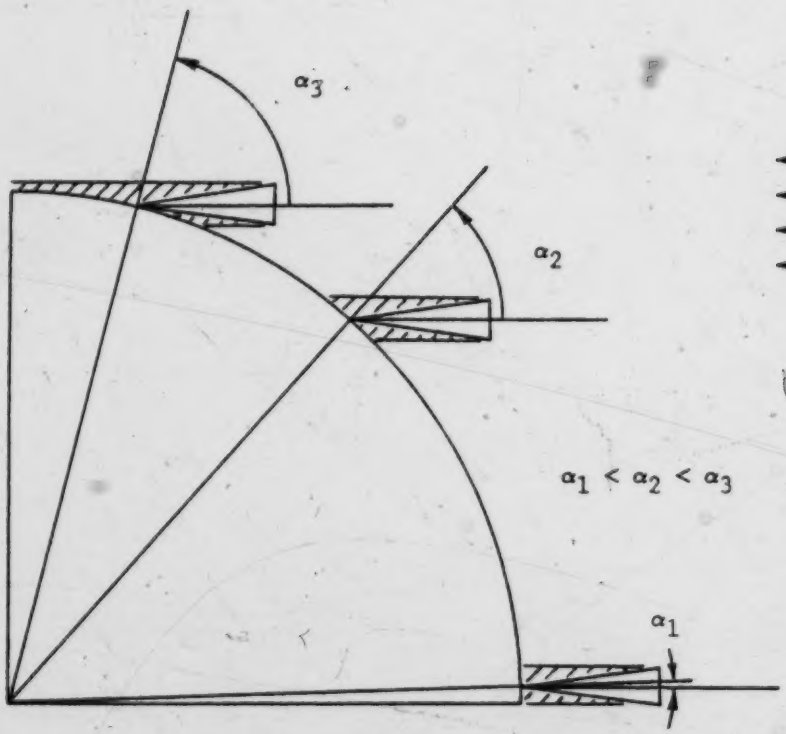

Figure 3.5 Effect of the droplet impact angle on the degree of shading activity downstream from discrete structure, for case with straightline trajectories.

is exposed to the airstream. The head shields the regions on either side of the cone-like structure from the approaching droplets, leaving behind air pockets. This will be referred to as the shading effect. If the collector's surface is everywhere normal to the droplet's trajectory, the feathers would be expected to shade regions on either sides of it equally. When the droplets are collected on a surface whose normal is at some positive angle to the droplet trajectories α, the area downstream from the feather is shaded more than the area upstream from the feather. The imbalance of the shading effect is greater as α increases from 0° at the stagnation line to α_m (defined in the figure) at the point on the cylinder corresponding to θ_m. Minimal shading cccurs at the stagnation line where α is zero. Progressively more shading takes place along the surface of the cylinder, downstream from the stagnation line, as α increases and larger air pockets are produced. There is maximal shading near θ_m where the air pockets have enlarged to the degree that they appear as layers of air, enhancing feather growth. Although this may be an explanation for the existence of rime feathers at the edge of an ice accretion grown on a cylinder, it would be interesting to observe where the feathers develop on accretions produced on other structural shapes. This requires a modification of the two-dimensional straightline model with the insertion of the appropriate equation for the surface of the structure.

For example, the equation for an NACA 0012 airfoil, with a chord length of 30 cm, has been used in the model. The leading edge of the airfoil, consisting of an accretion of 25.4 μm droplets, is shown in Figure 3.6. As in the case of the cylindrical collector, the shading effect increases with the angle of impact, with a resulting formation

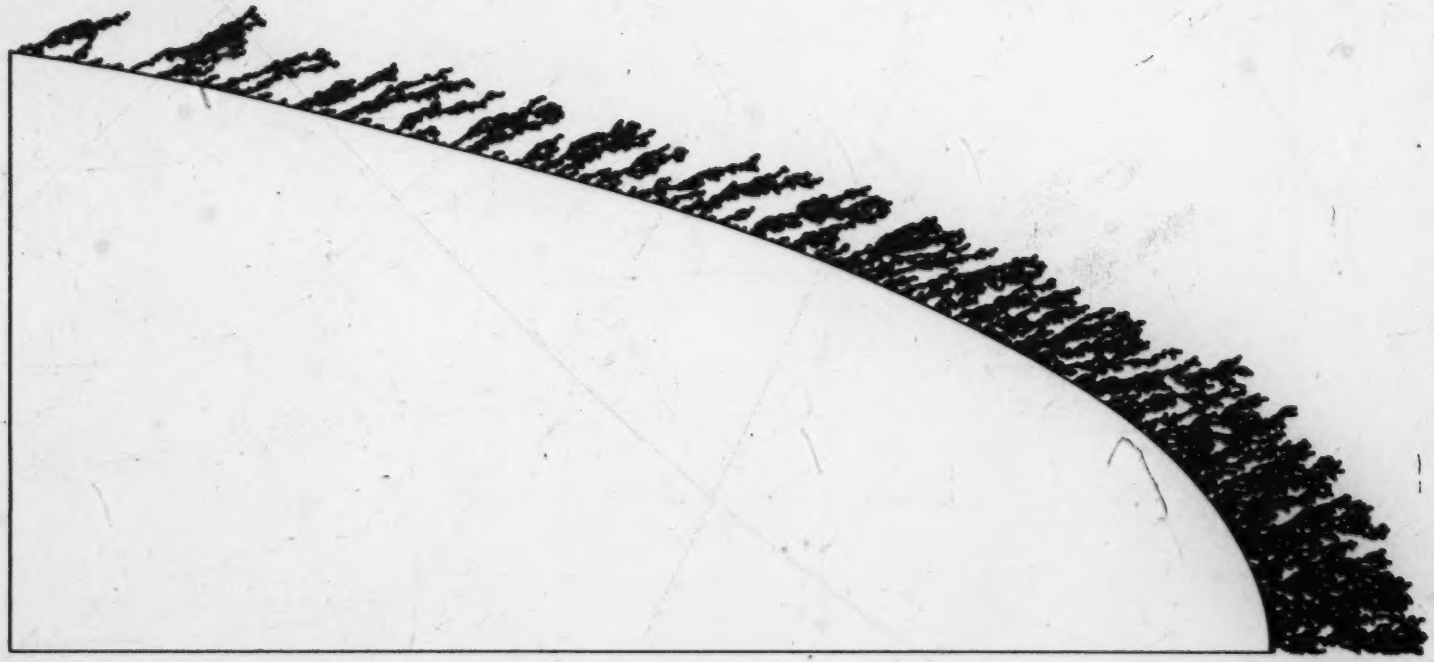

Figure 3.6 A straightline model produced by collecting 10,000 droplets on an NACA 0012 airfoil. D_d = 25.4 μm.

of feathers in regions where α is relatively large. Experimentally, at conditions of U_∞ = 11.2m/s, T_a = -10°C, MVD = 22μm, and LWC = 0.86g/m^3, the growth angle of the feathers were approximately 10°. This compared to a prediction of 20° by the model. The discrepancy was expected because in the actual accretion, the feathers only grew at the tip of the leading edge. In the model, the feathers appeared further downstream on the airfoil. The reason for this is that the model does not take into account for the change in flow field with time.

To observe further if feather-growth is, indeed, dependent on the angle of impact, an analysis of a deposit on a collector whose shape is such that α is constant over the whole surface facing the upstream direction, has been done. Figure 3.7 shows typical accretions on three wedges whose normals are 60°, 45°, and 30° to the straightline trajectories, referred to as 60°-, 45°-, and 30°-wedges respectively.

An important observation from the figure is that feathers are clearly distinguishable over the entire surface when the impact angle is relatively high, as evidenced in Figure 3.7(a). With relatively low α (Figure 3.7(c)), however, the feathers did not appear at all. It is interesting to note that these two results are in agreement with observations found on an accretion on a cylinder where feathers are visible in regions where α is greater than 45°. In fact, measurements of feather growth directions on the wedges are comparable to those grown on a cylinder. For instance, the average growth angles are about 15° and 23° on the 45° and 30° wedges respectively. This corresponds to measurements of about 13° and 25° at points on the surface of a cylinder where the normals were 45° and 30° to the droplet trajectories respectively. The accretions on the cylinder and wedges were produced

(a) 60° - wedge

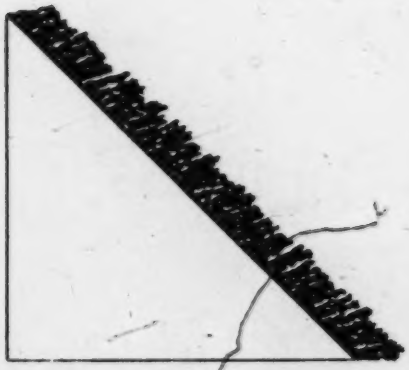

(b) 45° - wedge

(c) 30° - wedge

Figure 3.7 Straightline models produced by collecting 10,000 droplet on various wedges. D_d = 25.4 μm.

with 25.4 μm droplets. The results from the airfoil and wedges confirm that rime feathers develop readily in regions where α is relatively high, where the shading effect is greatest. Also, the growth angles of feathers seem to depend on α.

After establishing how a stochastic model could produce a feather, one is in a position to compare growth angle predictions between each type of stochastic model. The ensuing section deals with this exclusively with an emphasis on the various elements that have an effect on the growth direction of a feather.

3.2.2 Growth Angles

The growth angles of feathers were measured on model accretions produced at the conditions given in Table 3.1. The measurements have an error of ∓2° and are shown in Table 3.2. It should be pointed out that, the growth angles are always measured for the feather located closest to the edge of the accretion, where they are the most distinctive; this practice is followed throughout the study. Also, the random number generator that determines the droplet's initial y distance, y_s, from the stagnation line was unchanged from model to model. In other words, the sequence of y_s values at which the droplets were introduced into the flow was equivalent from model to model. The advantage of assuming the same random number generator throughout the study was to eliminate it as a variable. This was acceptable because it can be shown that each stochastic model could produce the same feather growth angles, at a given flow condition, with different random number generators. For example, the model with straightline trajectories produced feathers with growth angles of 15.5° and 15° when

Table 3.2 Growth angle measurements from straightline and curved trajectory models at various flow conditions. Straightline and curved trajectory models were produced with 20,000 and 10,000 droplets respectively.

	WIND TUNNEL CONDITIONS						ψ	ψ	ζ
Test #	D_d (μm)	U_∞ (m/s)	T_a (°C)	P_a (N/m^2)	D_c/D_d	K	Str. traj. model (∓2°)	Curved traj. model (∓2°)	Curved traj. model (∓2°)
(1)	(2)	(3)	(4)	(5)	(6)	(7)	(8)	(9)	(10)
A	18.2	10	-15	100,000	1396	0.89	16	-27	17
B	27.2	10	-15	100,000	934	1.94	25	-5	25
C	36.9	10	-15	100,000	688	3.57	23	-1	20
D	17.4	20	-15	100,000	1460	1.59	15	-20	15
E	30.3	20	-15	100,000	838	4.81	25	3	20
F	36.4	20	-15	100,000	698	6.95	23	13	26
G	17.7	30	-15	100,000	1435	2.46	15	-10	17
H	27.3	30	-15	100,000	930	5.86	25	14	29
I	32.4	30	-15	100,000	784	8.26	20	9	21

two different random number generators were used for D_c/D_d of 1000. In the curved trajectory model, the two generators produced an angle of -12° at a condition of 10 m/s, -15 °C and D_c/D_d equal to 1000. A change in the sequence of y_s values at which the droplets were introduced into the flow did not appear to have a significant effect on the growth angle. Therefore, a specific random number generator will be applied in the present study.

Another element common to all cases in Table 3.2 is that each model was produced with a monodisperse droplet spectrum. As noted in Section 3.1, it is desirable to optimize the cost of producing a model. Although introducing the droplets into the flow close to the cylinder ($x_s = 10D_c$) in a curved trajectory model minimizes the extensive calculations of the trajectories, they could be further reduced with the use of a monodisperse droplet spectrum.

To show that a monodisperse droplet spectrum does not have a significant effect on the feather growth angles, the straightline model was produced with droplets of equal size ($D_d = 27.2$ μm) in one case and of variable size (MVD = 27.2 μm) in another. In the latter model, the droplets were introduced into the flow one at a time, and their size was determined as follows: Plot probability distribution function (PDF) of the droplet spectrum histogram against the midpoint droplet size value of each of its bins. Then, convert PDF to a cummulative distribution function (CDF). After selecting a number between zero and one with a random number generator, the corresponding droplet size is obtained from the CDF. Model results of the two cases on a 2.54 cm diameter cylinder are shown in Figures 3.8(a) and 3.8(b). Results for local droplet concentration in these two cases will be given in the

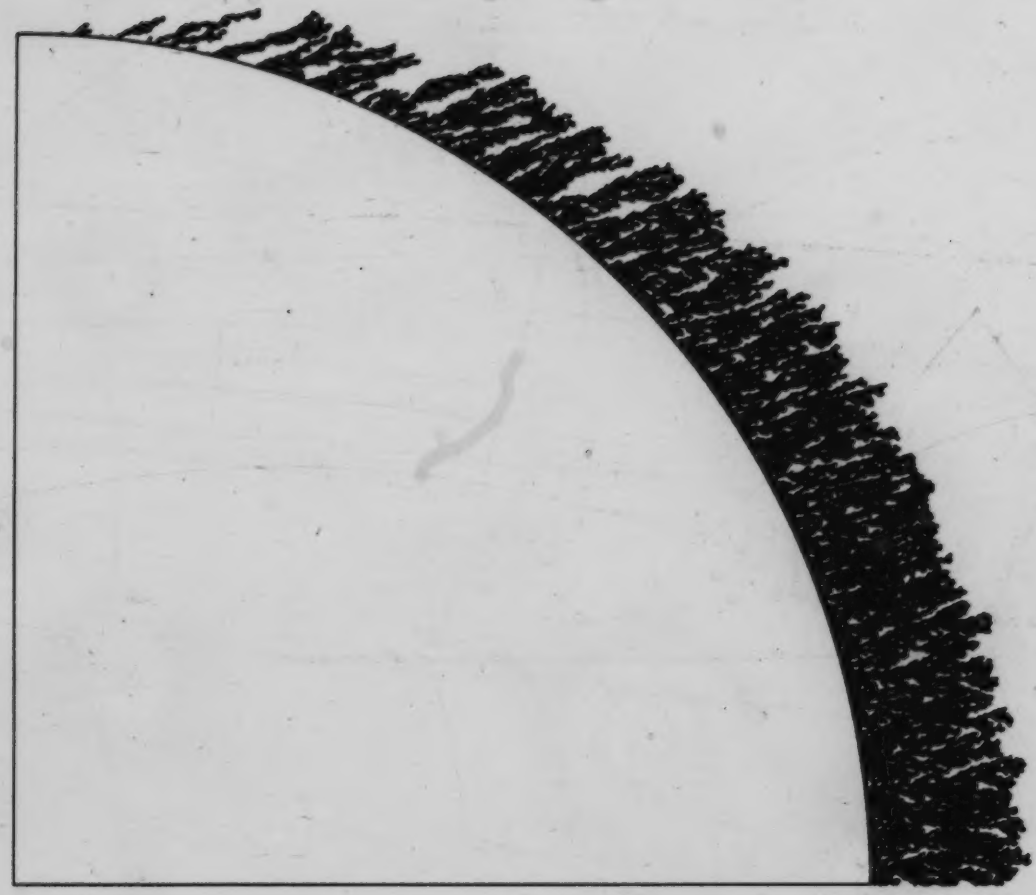

Figure 3.8(a) A straightline model produced by collecting 20,000 droplets on a cylinder. D_d = 27.2 μm.

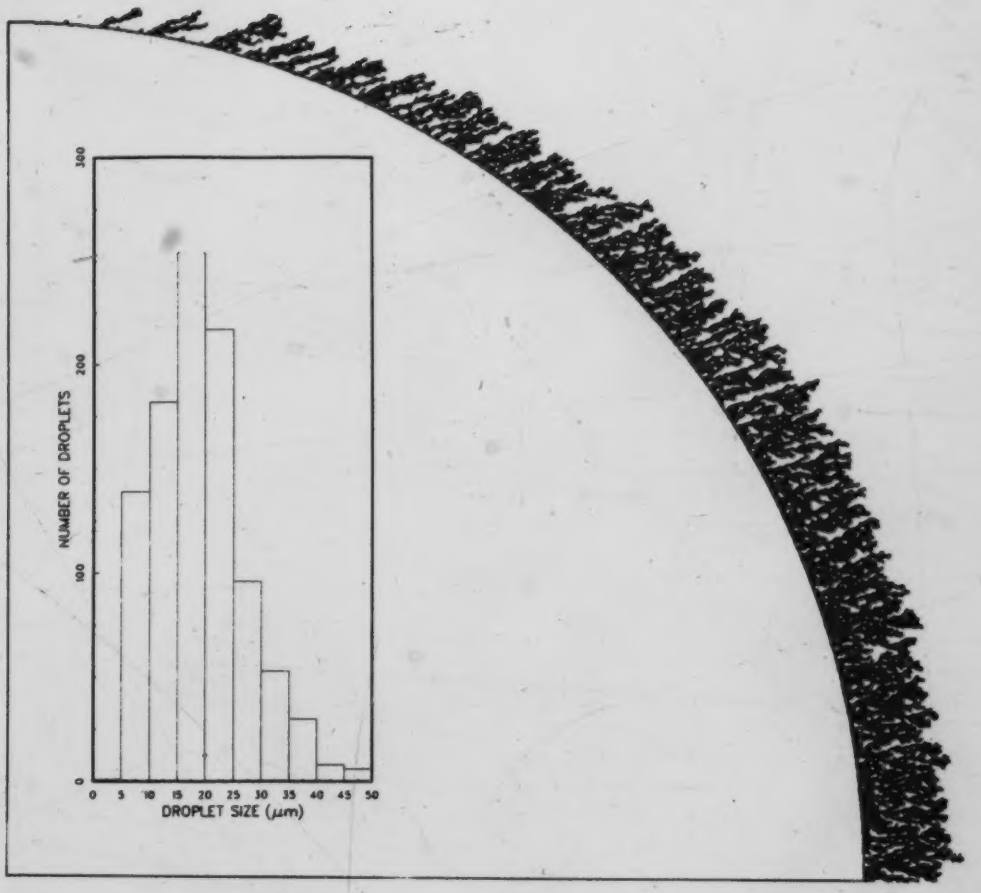

Figure 3.8(b) A straightline model produced by collecting 20,000 droplets on a cylinder. MVD = 27.2 μm.

next section. The growth angles of the feathers were measured to be 25° and 24° in the model composed of monodisperse and variable sized droplets respectively. A difference of 1° represents an error of about 4%, but when compared to the range of growth angle measurements obtained in a curved trajectory model composed of equal-sized droplets (column (9) in Table 3.2), the error is reduced to about 2.5%. This error is small, but unfortunately it cannot be compared with the error in using a monodisperse droplet spectrum in a curved trajectory model. For complexity reasons, a curved trajectory model made with droplets of variable size is not available. Despite this setback, there are several interesting trends observed from Table 3.2 which contains ψ predictions from models produced with equal-sized droplets.

Firstly, attention is directed to the column of straightline model results. From this set of measurements, it is observed that the growth angles were approximately 15° for cases where D_c/D_d was greater than 1400. Then, as D_c/D_d decreases to 700, ψ increases to about 23°. It appears that ψ varies inversely proportional to D_c/D_d, but this notion is incorrect because, in two other cases not presented in the table, the growth angles were 15° and 23° in the models where D_c/D_d was 254 and 508 respectively. Therefore, all that can be said is that in the straightline model, the feathers point away from the stagnation line (positive growth angles) and grow at angles between 15° and 25°. This was also discovered by Lozowski et al. (1983) in whose model single droplet impacts were made on a single frozen droplet. His Monte Carlo simulation model involved a D_c/D_d equal to one and produced a feather with a growth angle of 15° with respect to the mean impingement direction or droplet path. This implies that if the flow field remains

unchanged, as in the stochastic models, the rime feather growth direction depends only on the path of the trajectories, and on D_c/D_d.

The next set of important observations from Table 3.2 originates from the first column (9) of results pertaining to the curved trajectory model. The ψ measurements from this column varied from -27° (feathers pointing towards stagnation line) to 14°. The relatively wide range of growth angles is reflected in the various degrees of droplet trajectory curvature experienced from one curved trajectory model to another. Figure 3.9 clearly illustrates how the curvature of limiting trajectories, in three different flow conditions, influence the location of the feathers by changing the angle, χ, of the approaching droplets, defined as the angle between the tangent of a droplet trajectory and the stagnation line, at the point of droplet impact. When the droplets follow straight trajectories ($\chi = 0$), T_1, droplets are expected to make collisions on the surface of the cylinder up to a maximum impingement angle of 90°. Essentially, E_m is unity. As the curvature of the trajectories increases, to T_2 or T_3, θ_m decreases, because their points of tangency on the cylinder is shifted upstream along its surface and, therefore, the region for feather growth is relocated.

Figure 3.10 shows how an increase in the degree of trajectory curvature could depress the growth angle of the feathers. As mentioned in Section 3.2.1, feathers tend to grow towards the upstream droplet flow direction, indicated by V in the figure. In the straightline model, V is parallel to the freestream direction and feathers were seen to grow at angles between 15° and 25° relative to the stagnation line direction. In the curved trajectory model, V is at

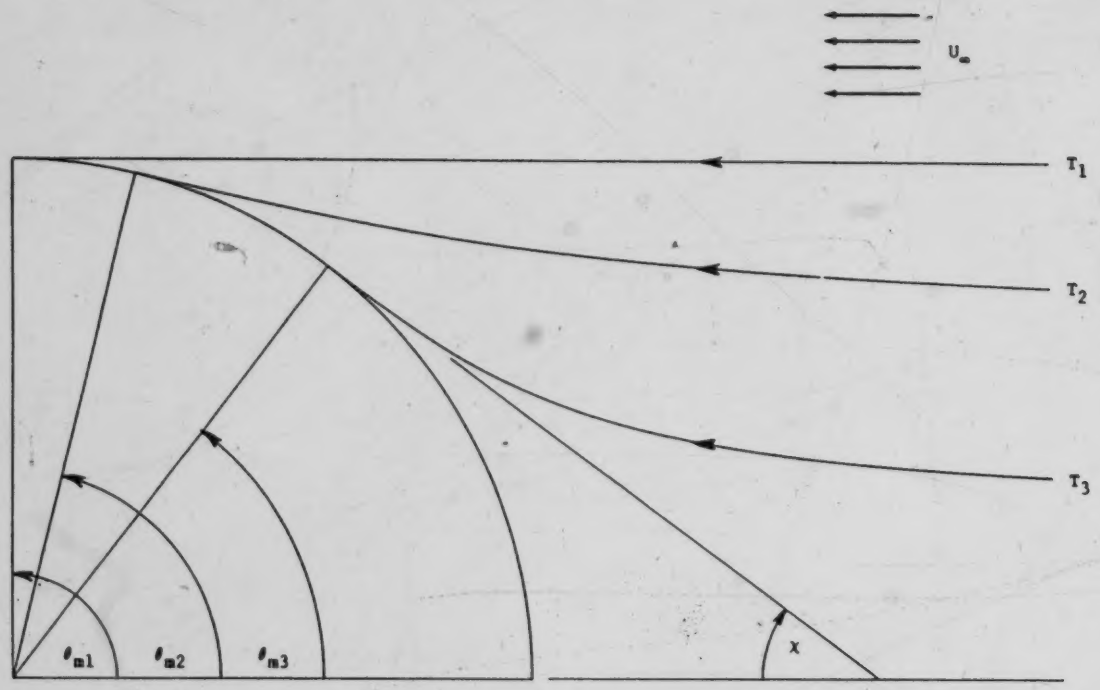

Figure 3.9 Influence of three different limiting trajectories T_1, T_2, and T_3 on the magnitude of θ_m.

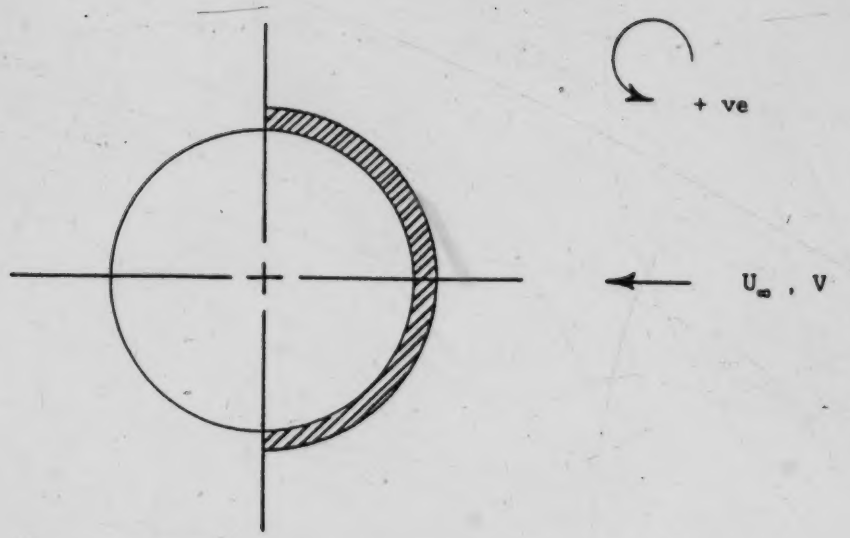

(a) $\chi = 0°$, straightline model

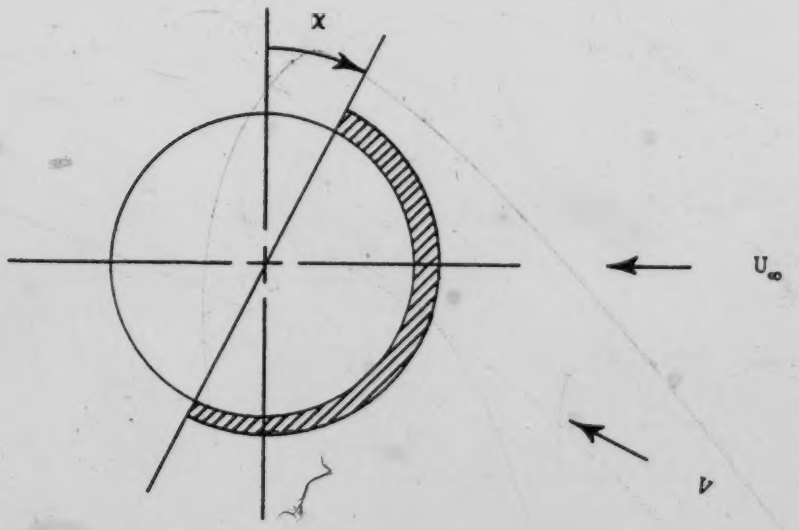

(b) $\chi < 0°$, curved trajectory model

Figure 3.10 Areas (shaded) on a droplet to which approaching droplets could stick.

some angle χ to the freestream direction and this changes the likely area on the accreted droplet to which approaching droplets would stick. The effect of this is a reduction of ψ as compared to those measured in the straightline model. In fact, if χ is large enough, the feathers in the curved trajectory model could point towards the stagnation line. Therefore, the degree of trajectory curvature of the droplets directly affects the growth directions of the feathers. The degree of trajectory curvature is determined by the inertia of the droplets. For this reason, it is desirable to interpret the curved trajectory model results for ψ in terms of the inertia parameter K.

In cases where $K < 3.5$, the growth angles ψ were less than zero. The droplet's inertia was low enough that the droplet tended to follow the airstream. The angle of attack χ of the trajectory was large enough to result in feathers pointing towards the stagnation line. In the remaining cases, K was greater than 3.5 and the trajectories straightened enough to result in droplets producing feathers with positive growth angles. Droplets with relatively large inertia are not easily influenced by the airstream and, therefore, tend to follow straight trajectories. Therefore, the basic difference between the two types of stochastic models lies in the difference between the K values in each model. In the curved trajectory model, K is determined by the flow parameters D_c/D_d and U_∞. A limiting case of the curved trajectory model could be the straightline model, where K is equal to infinity.

In pointing out that the curved trajectory model differed from the straightline case by the degree of curvature of the trajectories, it was expected that the growth angles of the feathers, relative to the path of the trajectory at the point of impact, would be similar between

the two models, provided their flow conditions were similar. Indeed, column (10) shows that the growth angles of the feathers ζ, relative to the tangent of the trajectories at the point of impact, were all positive and within 5° of ψ measurements from the corresponding straightline case. In the simple model, ψ and ζ are interchangable.

Figure 3.11 shows that regardless of whether ψ is positive or negative, ζ remains positive. Interestingly enough, in none of the cases from Table 3.2 was ζ greater than 25°, which could imply that this is approximately the upper limit for ζ on a cylinder in any type of stochastic model. The parallel between the ζ predictions of the two models was expected, because the curvature in the trajectories in the complex model should cause their growth angle predictions ψ to be depressed in comparison with those from the straightline model. The growth angles relative to the tangents of the trajectories, however, should only depend on D_c/D_d when dealing with accretion of spheres. The close agreement between results in columns (8) and (10) confirms that the curved trajectory model is constructed properly.

To summarize, there are various parameters that determine the location and growth angle of two-dimensional rime feathers in a stochastic model. Feathers grow readily along the edges of an accretion on a cylinder where the droplet impact angles are the greatest. The shading effect becomes a prevailing factor at high impact angles and because α is maximal at θ_m, the feathers have a tendency to appear in regions on the cylinder corresponding to θ_m. Since θ_m is relatively lower in a curved trajectory model, it is not surprising their feathers grow on the surface of a cylinder closer to the stagnation line compared to those formed in a straightline model.

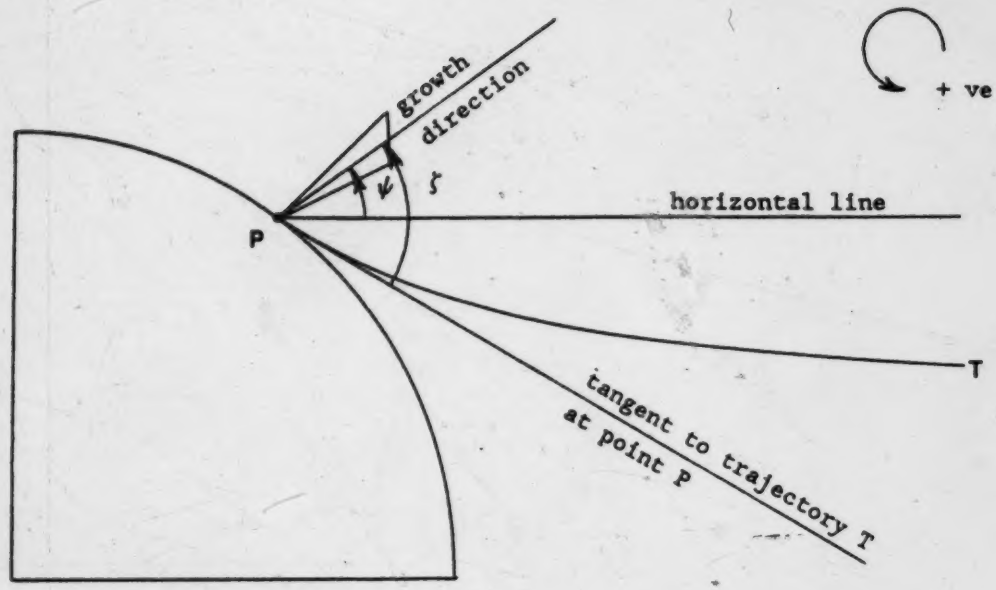

(a) $\psi > 0°$, $\zeta > 0°$

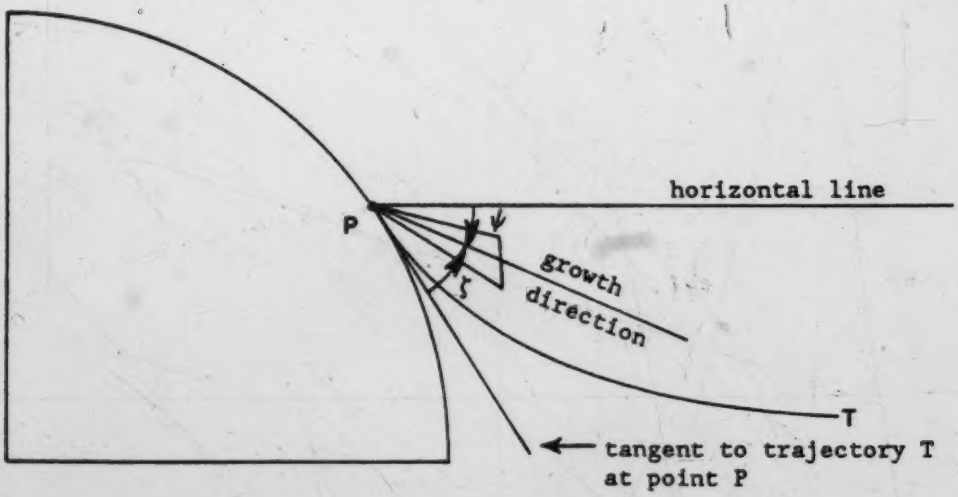

(b) $\psi < 0°$, $\zeta > 0°$

Figure 3.11 Diagrammatical definition of ζ. The ζ has a positive value, regardless of the sign for ψ. Trajectory T is not necessarily the limiting trajectory.

The curvature of the droplet trajectories directly affects the growth angle of the feathers. Droplets with relatively low inertia have a high degree of trajectory curvature. This depresses the growth angle of the feathers. In a simple model, all trajectories are straight and growth angles are positive, relative to the stagnation line, for all D_c/D_d. In the more complex model, however, an increase in D_c/D_d would increase the trajectory curvature and the resulting feathers would tend to point towards the stagnation line. Regardless of the flow conditions, however, ζ should be similar in both models.

The stochastic models have provided a means of analyzing rime feather growth. It would be interesting to observe how the growth angle predictions from the models compare with those measured on rime ice accretions produced on a cylinder in an icing wind tunnel. This will be investigated later in the study.

3.3 Local Droplet Concentration

Figure 3.1 shows a typical microstructure of a droplet accretion produced by a stochastic model. The existence of voids within the droplet accretion structure is an attribute unique to the present models. By examining the area occupied by the droplets within a certain boundary, one is able to obtain an estimate of the local droplet concentration. The current section begins with a look into the nature of the accretion processes occurring in the stochastic models to understand how air is trapped inside the model deposits; this information will help explain why the droplet concentration varies along the surface of a cylinder. Then, based on comparisons between the simple and complex model predictions for density, the effect that

various flow parameters have on the density predictions will be analyzed completely.

3.3.1 Mechanisms for Developing Porous Accretions.

The two stochastic models were produced with a size ratio D_c/D_d equal to 1000: a straightline model and a curved trajectory model. The concentration of droplets along the surface of the cylinder was calculated for each case and plotted in Figure 3.12. For convenience, the droplet concentration and density will be used interchangably when reference is made to the stochastic models. The quantity ρ/ρ_o is nondimensional and is refers to the density normalized by the density at the stagnation point.

A major observation from the figure is that the droplet concentration, in both models, decreases along the cylinder surface from the stagnation line to the edge of the accretion. This was also found to be true for any D_c/D_d, as will be shown in the next section. To see why this is so requires an explanation of how air inclusions are formed in the first place.

The basic feature of a stochastic model that enables air to be trapped within its structure lies in the shape that each droplet assumes following its impact on the accretion. The model forces droplets to remain spherical on impact. This prevents droplets from deforming, from coalescing, and from forming a dense structure. In fact, regardless of how droplets are packed together, the maximum attainable packing factor for spheres in 3-D accretions is 0.74 (Van Vlack, 1980). In two-dimensional packing, the maximum value for packing is 0.91 (See Appendix 8). In other words, there will always be

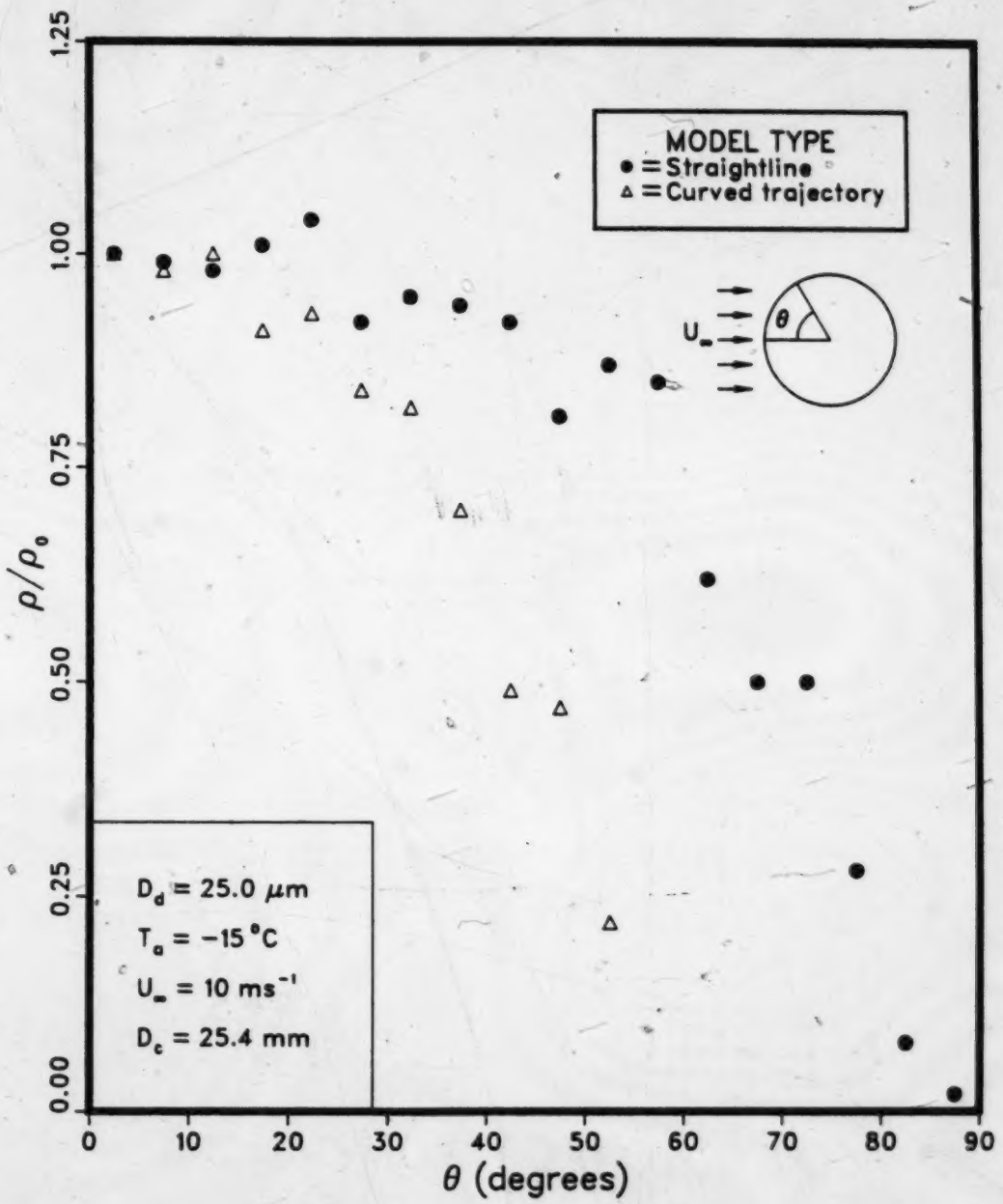

Figure 3.12 Plot of density variations produced by two stochastic models. D_c/D_d = 1000.

some space created in the structure when droplets do not deform upon impact with the structure.

3.3.2 Density Variation

Having established how air is trapped inside a rime structure, it is easy to explain how the shape of a collector affects the concentration of droplets along its surface. As discovered in Section 3.2.1, it is the impact angle, α, of the approaching droplets that determines the amount of shading along the entire surface of the structure. An increase in α results in the production of progressively larger air inclusions, because of droplet shading activity, with the effect of reducing the density, along the surface of the cylinder. Since the shading effect is minimal at the stagnation line, the density in its vicinity is the greatest. Rime feather growth at the edge of the accretion provides maximal shading with the effect of lowering the concentration of the droplets there.

Although this explains the general decrease in density from the stagnation line to the edge of the accretion on a cylinder, it should be noted that the dependence of density on α applies to all types of collectors. Regardless of the shape of the collector, the density is expected to be relatively low in regions where α is relatively high. The converse is also true. A glance at Figure 3.6, for instance, shows this to be valid for an NACA 0012 airfoil. Therefore, a stochastic model automatically produces a density variation because droplets remain spherical upon impact and the shape of the collector is such that α varies along its surface.

3.3.3 Influence of Flow Parameters on Density

An analysis of the density predictions from each type of stochastic model is essential to point out the differences between the simple and complex models. From Figure 3.12, it is apparent that the density in the straightline model is relatively constant along the surface of the cylinder from the stagnation line to an angular position of about 20°. Thereafter, the density decreases to zero at the edge of the accretion. The density variation predicted by the curved trajectory model, however, shows that the rate of change of density was greater than that produced by the simple model. To observe if D_c/D_d had an effect on the difference in the rate of density change between the two models, both models were subjected to three different size ratios and their resulting density predictions are shown in Figures 3.13(a), 3.14(a), and 3.15(a).

In general, both model density predictions were similar with one another when accretions were built with relatively low D_c/D_d such as 508. With larger size ratios, the difference in the rate of change of density between the two models increased. The implication of these results is that the manner in which the deposit was formed in both models was similar when accretion droplets are relatively large. Large droplets have large inertia and their trajectories would approach straight lines when the inertia parameter is large enough.

On the other hand, when dealing with relatively small droplets, the effect of trajectory curvature comes into play. The droplet impact angle α is high at θ_m, where shading is maximal and density is minimal. In both stochastic models, the density decreases from a maximum at the stagnation line to a minimum at θ_m. Because the trajectory of smaller

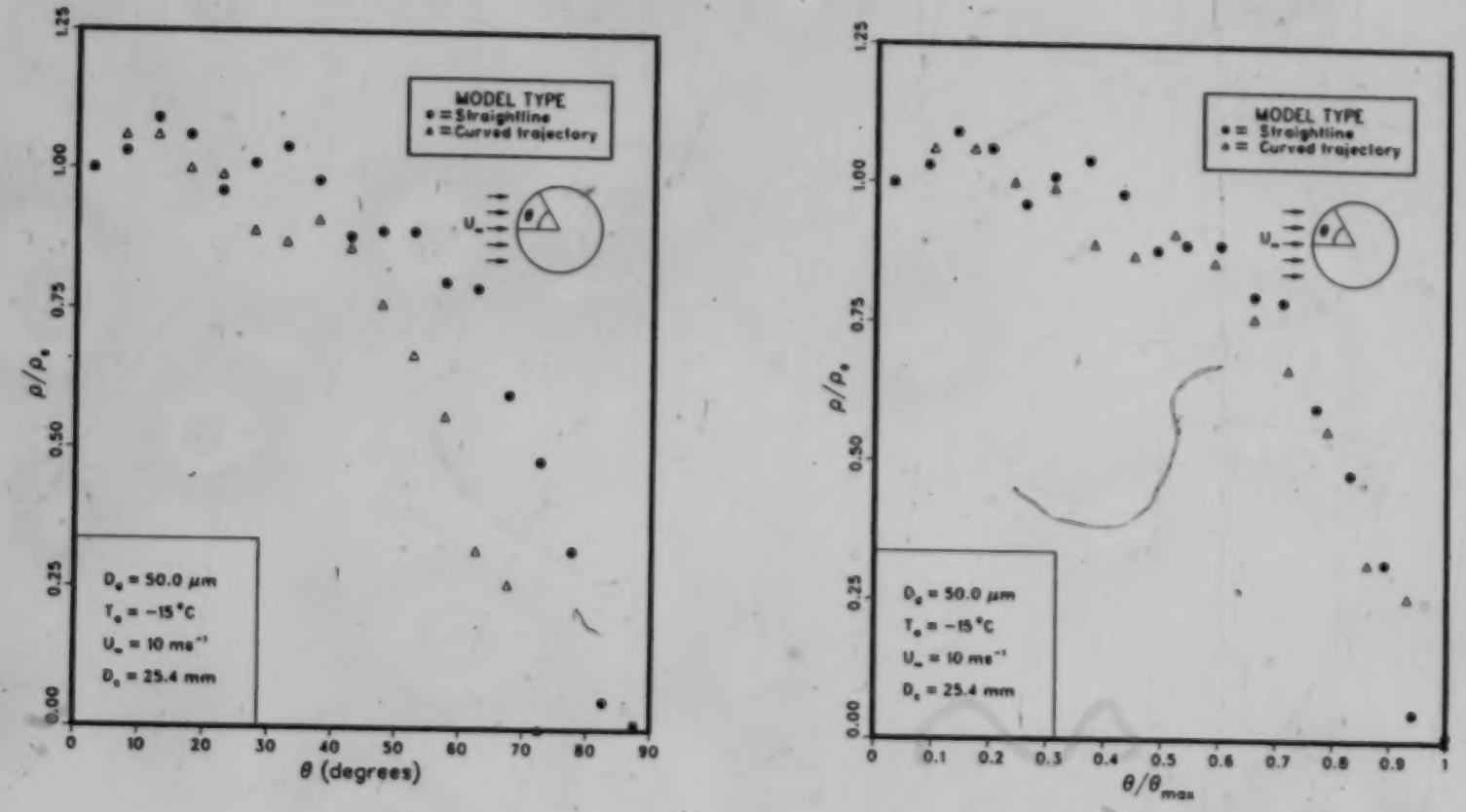

Figure 3.13 Comparison of density predictions by two types of stochastic models. D_c/D_d = 508.

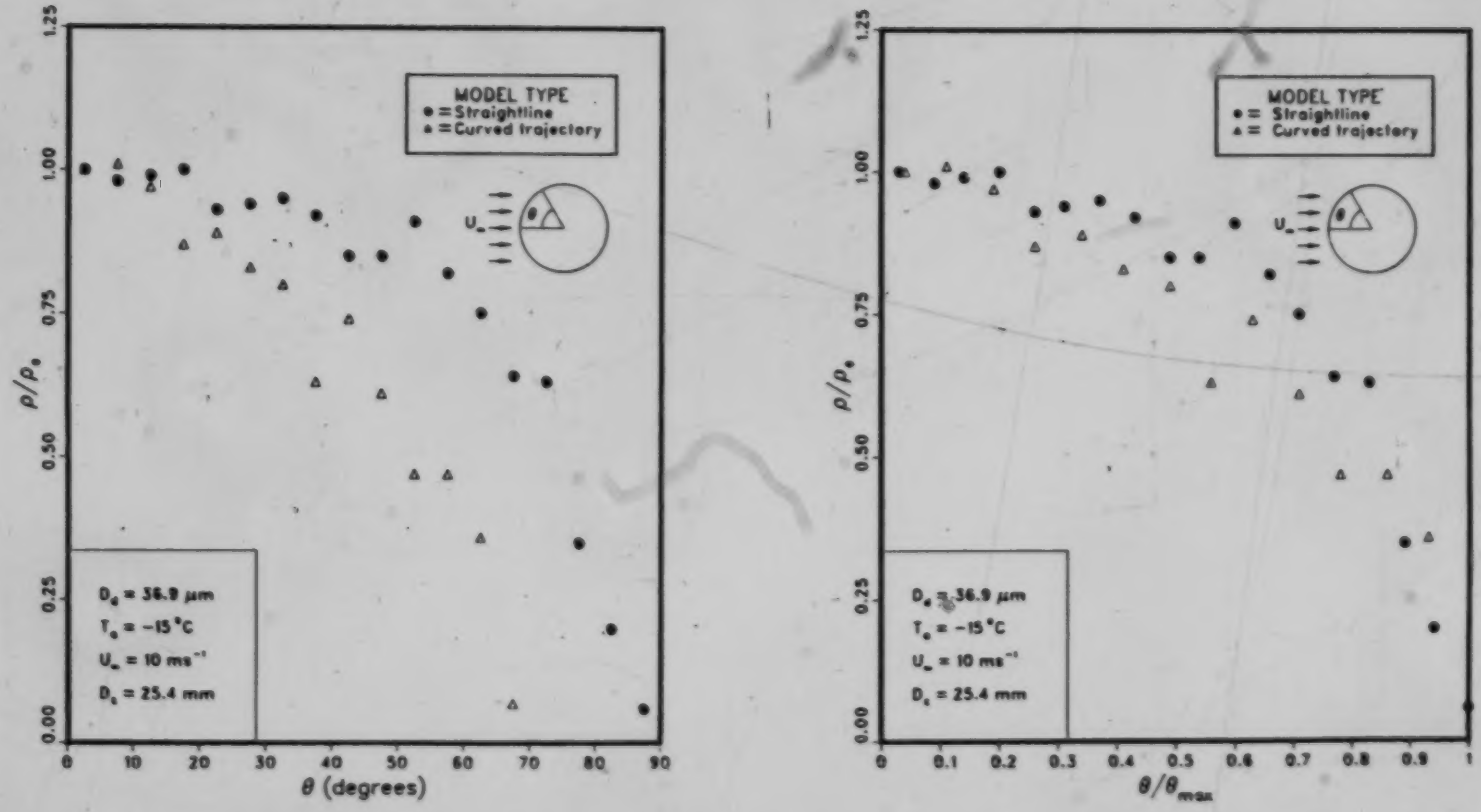

Figure 3.14 Comparison of density predictions by two types of stochastic models. D_c/D_d = 688.

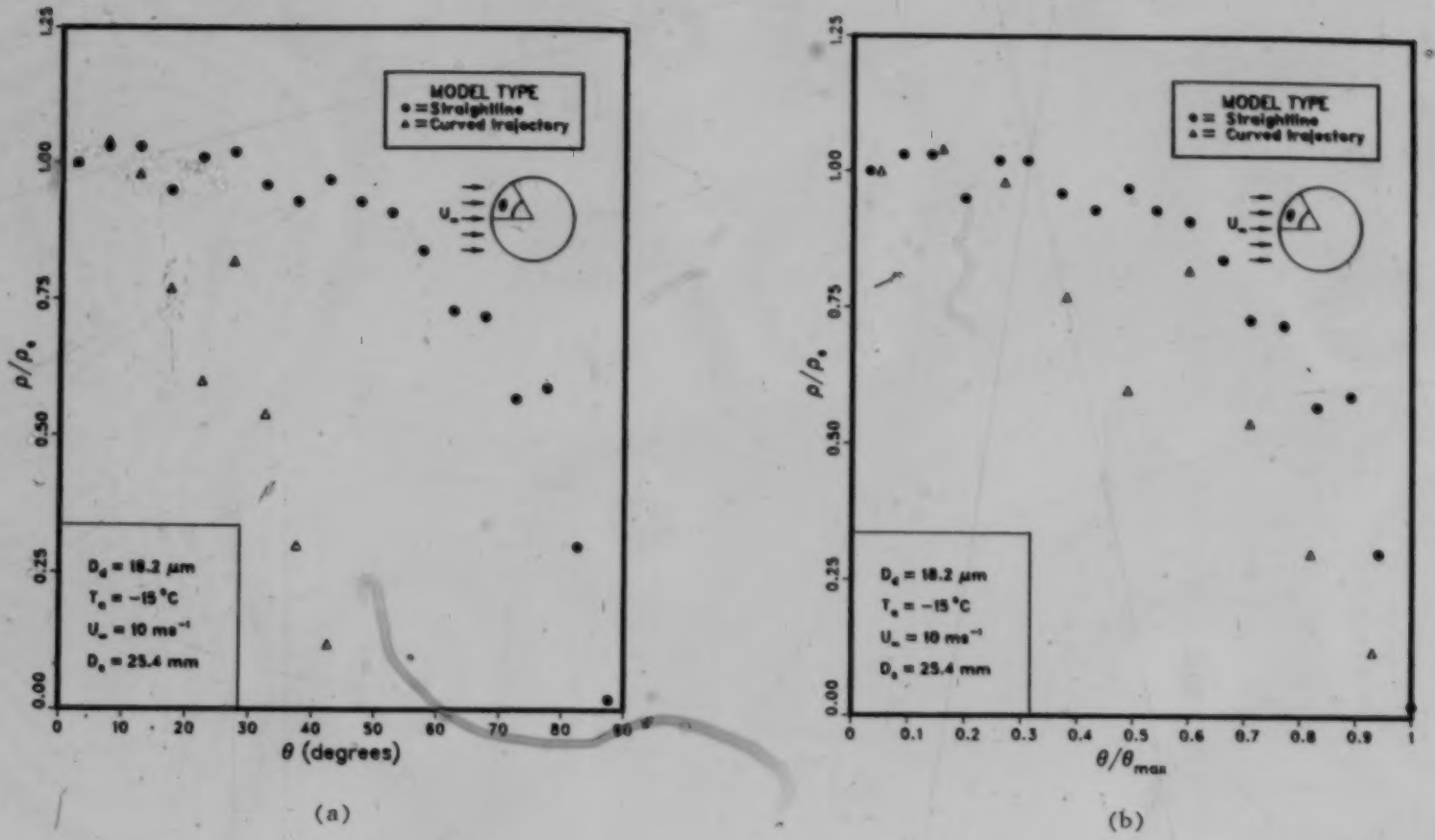

Figure 3.15 Comparison of density predictions by two types of stochastic models. D_c/D_d = 1396.

droplets has a tendency to lower the θ_m, the local density of the resulting deposit decreases to a minimum value over a shorter surface area on the cylinder, as compared to the relatively larger surface area in a straightline model on which to build the accretion. This gives rise to a larger rate of change of density along the surface of a cylinder in the curved trajectory model.

If one compared ρ/ρ_o from a straightline model with that of a curved trajectory model, at a position θ/θ_m, however, the discrepancies between the model predictions would appear to be reduced. This observation is clear in Figures 3.13(b), 3.14(b), and 3.15(b) which are reproductions of the results from the (a) portion of the respective figures; only this time, the non-dimensional densities were plotted against θ/θ_m.

Although the (b) portion of Figures 3.13 to 3.15 show that the discrepancies in the density predictions between each model were less, the densities from the complex model were, again, relatively lower than those of the simple model. This suggests that the structure produced with curved trajectories is, in general, more porous than that produced with straight trajectories. This assumption appears to be valid for D_c/D_d greater than 508. In these cases, it is suspected that the curvature of the trajectories in the complex model was sufficient to result in relatively heavy shading activity on areas on the surface of the cylinder close to the stagnation line. This has a tendency to create open structures closer to the stagnation line in the curved trajectory model, compared to that in the simple model. Thus, at a given position θ/θ_m on the cylinder, the density is expected to be lower in the complex model.

In the case where D_c/D_d was equal to 508, both model predictions in Figure 3.13(b) appear to coincide. Since the simple model ($K = \infty$) is an extreme case of the curved trajectory model, it was expected that if K was large enough, both models' accretions would be similar. Figure 3.13(b) confirms that when the droplets' inertia exceeds a certain value, yet unknown, droplets follow approximately straight lines. Therefore, D_c/D_d has an effect on the discrepancies between the two types of stochastic model in terms of density predictions. The disagreements, however, vanish for situations where D_c/D_d is less than about 508.

The discrepancies are reduced further when one plots ρ/ρ_o against α. Figure 3.16 shows that both model predictions for the case with $D_c/D_d = 1396$ were similar. The plot suggests that the local droplet concentration depends on the local droplet shading activity, given by α.

A second element that could have an effect on the density predictions is the type of droplet spectrum assumed in the models. In this study, a monodisperse droplet spectrum was utilized. To investigate whether a variable-size droplet spectrum has an effect on the density predictions, a 2-D straightline model was produced with droplets of variable size. The MVD was 27.2 μm. The density variation was obtained and plotted, along with those obtained from a monodisperse droplet spectrum, in Figure 3.17. The packing factors at the stagnation line were 0.39 and 0.4 in the models built with variable-sized and monodisperse droplets respectively. Although the effects of a real droplet spectrum were observed for only one case, the figure indicates that the application of a monodisperse droplet

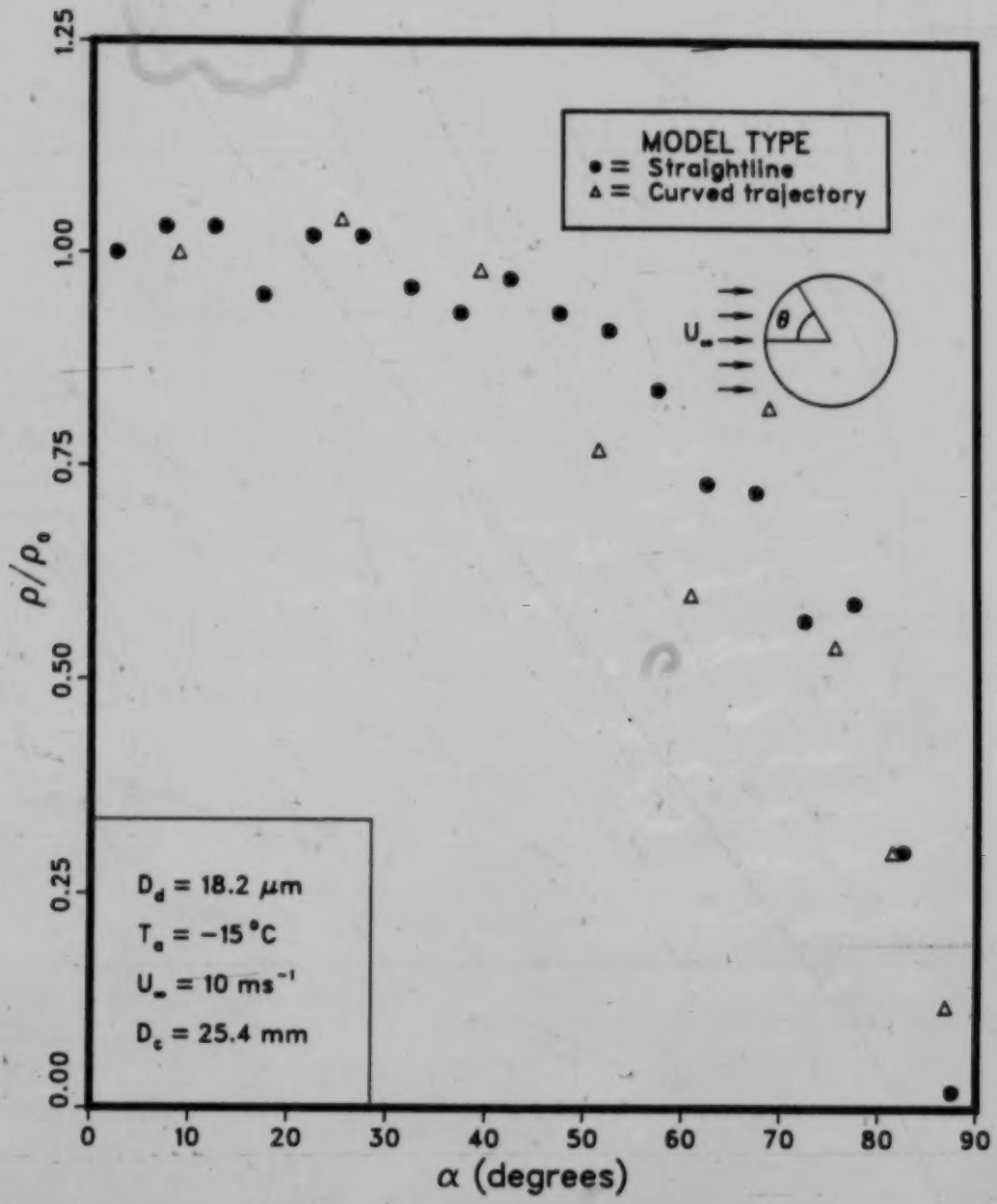

Figure 3.16 Model predictions of ρ/ρ_o versus α for test A from Table 3.1.

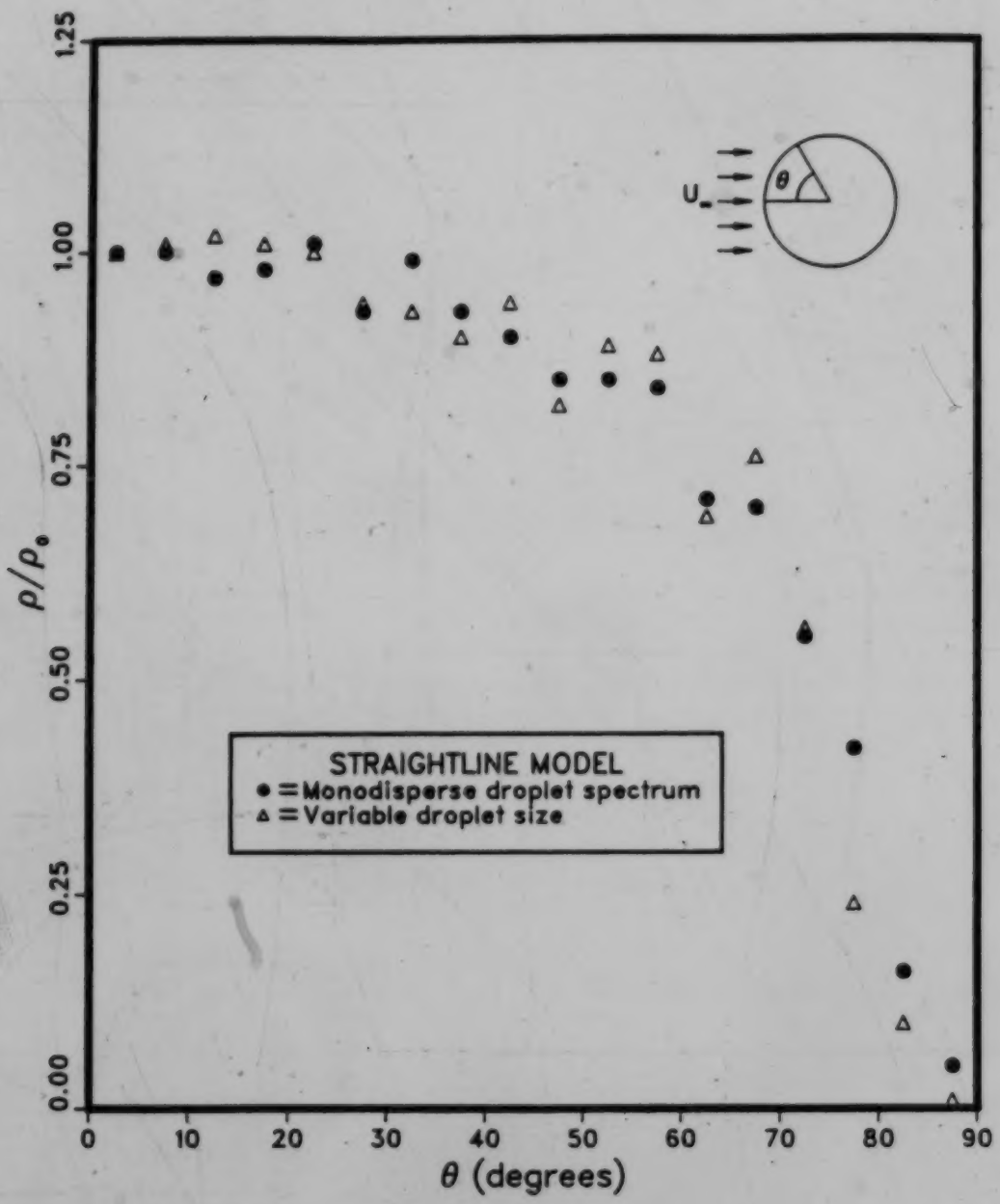

Figure 3.17 Effect of a variable droplet spectrum on the density predictions by a straightline model. D_c/D_d = 934.

spectrum does not have a significant effect on the density predictions from a simple model. Unfortunately, nothing could be concluded about the complex model, because a curved trajectory model produced with droplets having different size is not available.

The third, and final, factor that has an influence on the stochastic model's predictions for density is the 2-D nature of the accretions. Therefore, it would be useful to observe the behaviour of the simple model in three dimensions. In one example, a 3-D accretion was produced and the density analysis was confined to a 3-D annular region on the surface of a cylinder. The thickness of the region was $20D_d$, and the depth was $8D_d$. All sectors were again 5°-sectors, and D_c/D_d was 1000. The density predictions from the 3-D model, along with those from the 2-D model, are plotted in Figure 3.18. It was found that the packing factor at the stagnation line was 0.2 and 0.4 in the 3-D and 2-D accretions respectively. There was no apparent reason for this discrepancy, but the figure shows that the variation in density along the cylinder surface was similar in the two cases. The implication of these two findings is that it would suffice to create 2-D model accretions to obtain correlations for density that would be representative of the 3-D case. Although the 2-D and 3-D models could produce similar correlations for density, the 2-D model should be used with a precaution: the 2-D model generally overpredicts the absolute density of a 3-D case by a factor of about two.

Unfortunately, due to the extensive calculations involved, a 3-D curved trajectory model is not available. Also, a graphical presentation of a 3-D straightline accretion could not be produced with the existing computer facility.

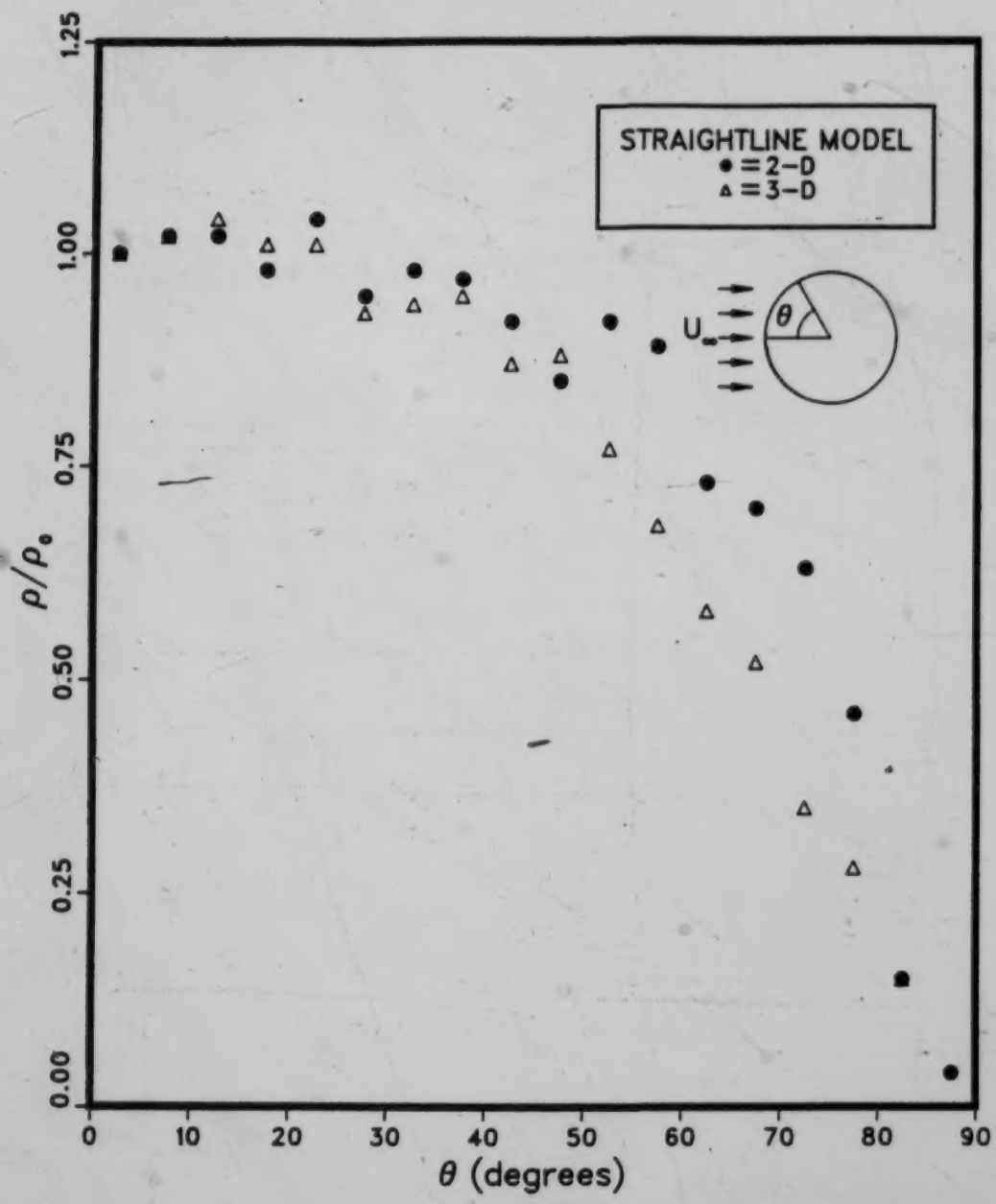

Figure 3.18 Comparison of density predictions from a 2-D model with those from a 3-D model. $D_c/D_d = 1000$.

Pursuit of the stochastic approach to the modelling of rime icing has provided an avenue for obtaining a local density prediction. Unlike previous icing models, the density prediction in a stochastic model is arrived at without recourse to empirical correlations. The next step is to investigate the accuracy of the predictions by comparison with some experimental results. Before this could be accomplished, however, the experimental technique should be outlined. This will be provided in the following chapter.

4. EXPERIMENTAL INVESTIGATION

4.1 Experimental Apparatus and Technique

Experimental measurements of rime feather growth angles and local ice densities on ice samples are needed to verify the predictions by the stochastic models. A facility for producing rime ice samples on cylinders and a technique for measuring local ice densities is essential to further our present research. The current section will outline the equipment and techniques required for the production and preparation of ice samples for the measurement of local ice densities and rime feather growth angles.

The simulation of atmospheric rime icing on structures is carried out in the FROST [1] tunnel at the Department of Mechanical Engineering at the University of Alberta. The closed-loop icing wind tunnel provides an environment in which the four basic icing parameters of windspeed, air temperature, liquid water content, and the water droplet spectrum can be controlled. Figure 4.1 shows a layout of the facility illustrating the essential components.

Air movement inside the tunnel is produced by a fan located downstream from the test section. The airspeed is controlled by adjusting a set of vanes situated immediately downstream from the fan. From the fan, the air circulates past a heat exchanger and through the spray bar section. There, the air carries the water droplets from the spray through a contraction and into the test section, where a cylinder is mounted horizontally. The air then returns to the fan and another

---

[1] Acronym for the Facility for Research on Solidification and Thawing.

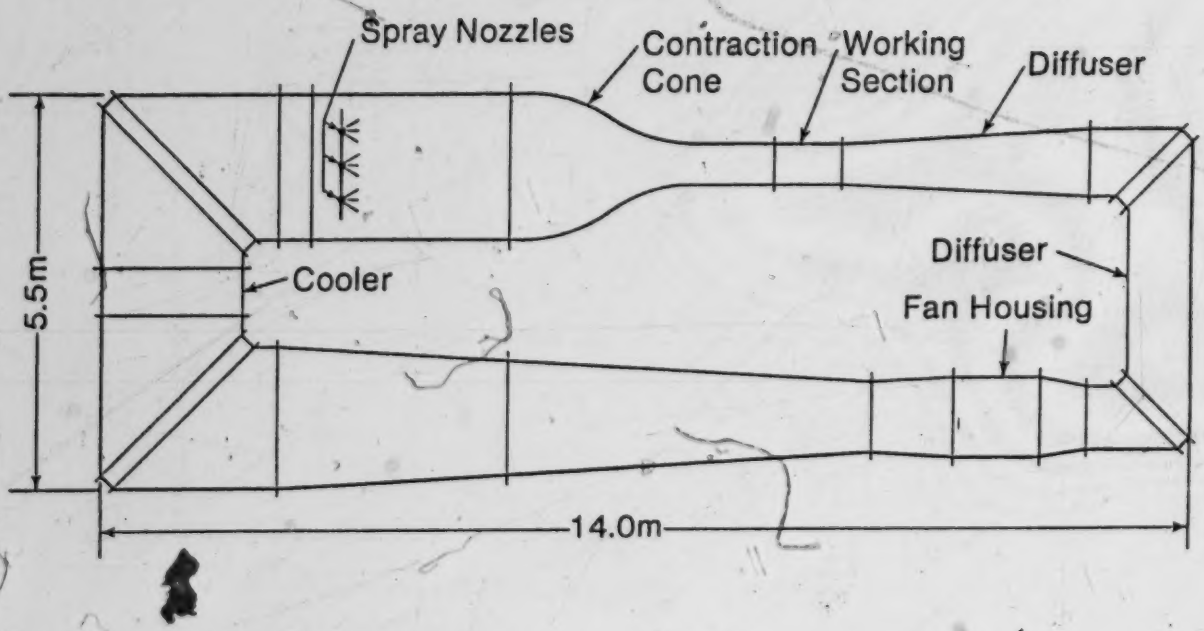

Figure 4.1 Horizontal layout of FROST tunnel and its essential components.

cycle begins.

The tunnel is instrumented to measure several icing parameters. A shielded copper-constantan thermocouple is placed in the test section and a control system is set up to regulate the air temperature to within 1 °C at large system loads. i.e. high air speeds, low temperatures. The refrigeration unit has the capacity to bring the air temperature to as low as -15 °C.

A spray bar is located upstream from the contraction and consists of a pneumatic nozzle which atomizes the water flowing through the nozzle to produce water droplets. The droplet spectrum of the spray is determined using an oil slide technique from which the median volume diameter (MVD) can be calculated. The technique involves a brief introduction of a glass slide, coated with oil, into the test section to collect a sample of about 200 droplets from the airstream. After taking a photograph of the slide containing the water droplets, the droplet sizes can be measured from the projection of the developed film onto a screen. A droplet spectrum could then be obtained whereby the MVD could be calculated.

The tunnel is also instrumented with a manometer to measure the pressure change through the contraction. The measurement is conveniently converted into a velocity reading using Bernoulli's equation. A maximum airspeed of 60 m/s is attainable in the test section.

For the feather growth angle and local ice density tests, the flow conditions were set in a range in which rime feathers can grow. For example, if a 2.54 cm diameter cylinder is the substrate, the MVD and windspeed must not exceed 40 microns and 30 m/s respectively. This was

determined by trial and error. Also, the air temperature should be below 0 °C to promote dry growth.

Measuring growth angles require minimal equipment. Basically, ice is grown on a cylinder. Following the test, a cross-sectional photogragh of the accretion is taken and developed. From the prints, the rime feather growth angles can be measured.

A few more essential pieces of equipment are needed for the measurement of local ice densities. Following the accretion of an ice sample on a cylinder, the sample is separated from the cylinder and a thin cross-sectional slice is required for use with X rays. A coarse thickness of the slice is obtained with a band saw, but when utilizing an X-ray technique to measure the variation in local ice density, it is important that the ice thickness remains constant. This is obtained with a sledge microtome, which is a precision-mechanical instrument that may be used for shaving an ice slice down to a uniform thickness. Plate 4.1 shows the type that was used in the experiments. The microtoming procedure is accomplished first, by gluing one side of a thin ice slice onto a flat plate. The plate is then mounted in a vice-like clamp, and the specimen is shaved by moving the holder assembly across a stationary knife repetitively. The microtoming technique is straightforward, but a careful choice of the glue type, the plate material, the operating room temperature, and the thickness of the ice to be removed in each cycle will determine the overall success in microtoming an ice sample to the required thickness. After experimenting with different types of glue, it was found that bondfast white glue exhibited excellent bonding characteristics when used with an aluminum plate in an environment of -12 °C - the glue did not soak

Plate 4.1 A sledge microtome.

into the ice structure.

After securing an ice sample onto a plate, a preset thickness of up to 40 μm could be removed from the ice surface each time the holder assembly is moved across the knife. The duration of the shaving process would be reduced when relatively thick sections are removed, but it was found that the adhesive forces provided by the glue was able to sustain the forces from the cutting action only when less than 10 microns is removed per cutting cycle.

The first face of the ice slice is microtomed until it is entirely smooth. Typically a total of about 1 mm thickness should be removed. Then, the bond between the glue and the plate is weakened to separate the slice from the plate. Then, the remaining side of the slice was then shaved until the overall thickness reached 1 mm. Finally, the thin slice was separated from the plate by manually chipping the glue from the plate with a razor blade.

At this time, it is important to note that in order to obtain "local" ice densities, it would be appropriate to minimize the ice thickness. Therefore, the sample should be microtomed to as thin a slice as possible. With rime ice, however, the minimum attainable thickness was found to be about 1 mm before the normal forces from the cutting action could initiate a crack within the weak ice sample. Following the microtoming procedure, the rime ice slice is ready to be X-rayed.

4.2 Measurement of Local Ice Density

The local ice densities within an ice sample were measured by transmitting an X-ray beam through the ice structure and onto a film.

The principle behind the technique is that the reduction in intensity of the original beam is dependent on the variation in absorptivity within the sample, which could be related to the variation in local ice density.

The X-ray unit used in the experiments consisted of a Kristalloflex 2H generator, a cooling unit, and the X-ray tube itself. The generator has a rating of 60kv, and the cooling unit is connected to the X-ray tube to extract as much heat from the anode as possible. The X-ray unit in shown in Plate 4.2. The penetration of an X-ray beam, generated at 60kv with a tube current of 10ma and exposed for 9 seconds, through a 1 mm ice sample, placed on an X-ray film 60 cm from the focus, was found to produce optimum radiographic quality. Since the density of ice is similar to that of the human tissue, therapy verification film, which was used successfully in mammography, was appropriate for the present study.

A 30 X 30 X 72 cm wooden box lined with 3 mm lead on the interior was used to enclose the X-ray tube, the film, and the ice sample, to protect the operator and to keep the film from exposure to light. Also, without the box, scattered radiation from nearby objects may reach the film.

The X-ray of an ice sample produces a latent image on the film which, when developed, shows up as a variation in film darkness. A microdensitometer is an optical device consisting of a light beam that traverses across a radiograph and plots its film density. The type used in the study is shown in Plate 4.3. The basic principle of operation of a microdensitometer is based on a true double-beam light system, in which two beams from a single light source are switched

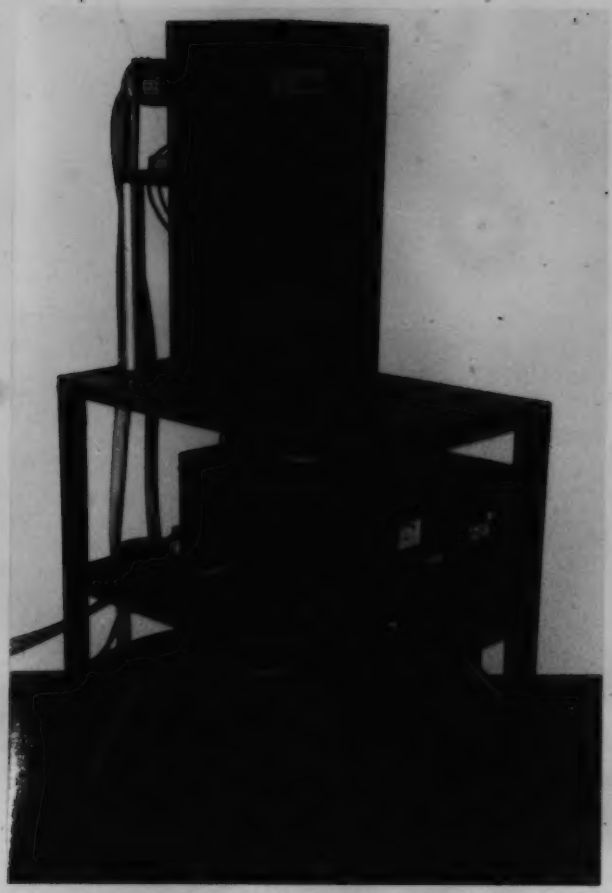

Plate 4.2 A Kristalloflex 2H X-ray generator with lead-lined box.

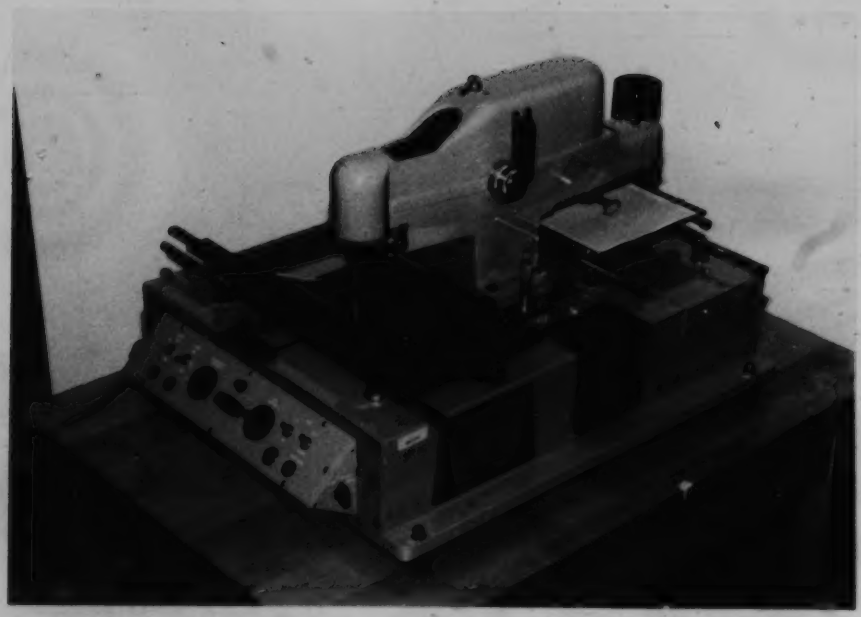

Plate 4.3 A double-beam recording microdensitometer - model MK III C S.

alternately to a single photomultiplier. One beam passes through the film while the other is used as a reference. If the two beams are of different intensity, a signal is produced by the photomultiplier, which, after amplification, causes a servomotor to move an optical attenuator, to which a direct-writing pen is attached, so as to reduce the intensity difference to zero. The position of the optical attenuator records the film density of any area on the radiograph. The film density is an average value for the darkness of an effective illuminated area on the film. A smaller effective illuminated area would result in a better approximation for local film density.

Prodi (1970) showed that the local ice densities could be obtained from a densitometer trace by using the following fomula,

$$\rho_h = \rho_i \frac{D_o - D_b}{D_o - D_a} \qquad (4.2.1)$$

where,

ρ_i - reference ice density
ρ_h - local ice density in test sample
D_a - film density in reference ice sample
D_b - local film density in test sample
D_o - background film density

Figure 4.2 illustrates the typical areas on a radiogragh through which a densitometer beam would traverse. The accompanying density plot is also shown in the figure. If the densitometer is calibrated to provide film densities directly on the plot, then Prodi's formulation can be used to calculate local ice densities for any point on the images in the radiogragh. Because there is a linear variation between the densitometer's pen displacement (X's in the figure) and the film density, the calibration technique is straightforward and is as follows: Firstly, a reference ice sample of known density, ρ_i, was be

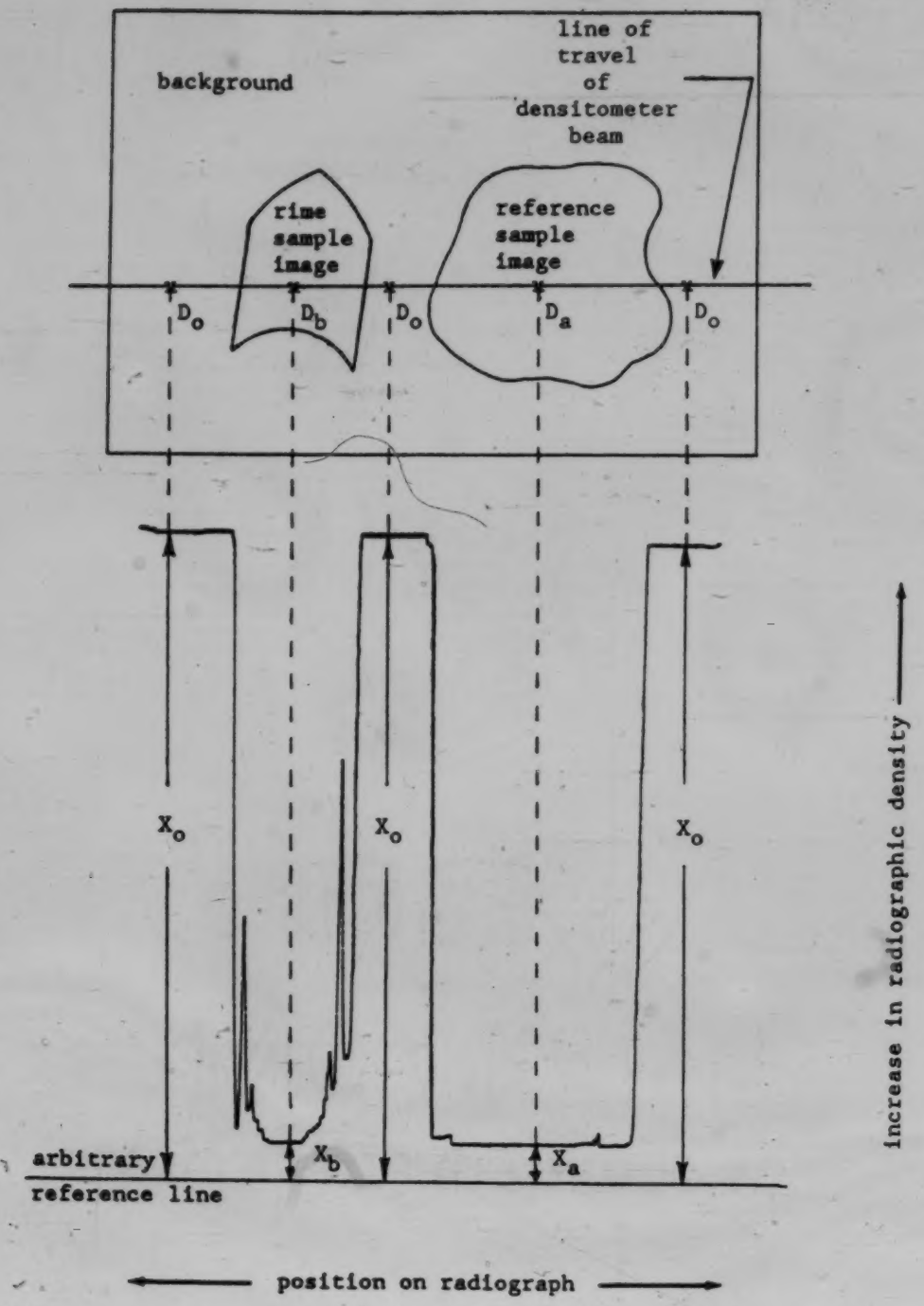

Figure 4.2 Variation of film density with position on the film. The pen displacement is proportional to the film darkness.

placed on the film, next to the rime ice sample. An X-ray is taken to produce two images, as shown in Figure 4.2. Then, as the densitometer beam passes through the image corresponding to the reference sample, the pen will move a distance of $(X_o - X_a)$. After performing this calibration, an alternate expression,

$$\rho_h = \rho_i \frac{X_o - X_b}{X_o - X_a} \qquad (4.2.2)$$

is used to calculate local ice densities. In fact, the traces could be inverted and an absolute ice density scale could be constructed based on $(X_o - X_a) = \rho_i$. This practice was used in the experiments when measuring local ice densities.

4.3 Experimental Procedure

In the first of two sets of experiments carried out in the present study, the growth directions of rime feathers were measured from accretions formed on a 2.54 cm diameter cylinder. Three different droplet size distributions with median volume diameters of approximately 20,30, and 40 μm and three windspeeds of 10, 20, and 30 m/s were used to run the tests. The nine different combinations of airspeed and spray represented the range of the FROST tunnel conditions in which rime could grow. Air temperature in the test section was kept at -15 °C, and the duration of each test was in the range of 10 to 45 minutes. The sole criteria for the test duration was that the rime feathers must appear clearly distinguishable in the viewfinder of the Nikon camera.

Following each test, a picture of the cross section of the accretion was taken and when the experiment was completed, the roll of black and white film was developed. A print of each accretion was made on which the growth angles of the rime feathers were measured. Predictions from the two stochastic models at the experimental conditions and the growth angle of the two-dimensional rime feathers were obtained.

A second set of experiments was conducted in which the local ice densities were to be measured on fifteen rime ice samples collected on a 2.54 cm diameter cylinder. Unfortunately, only five samples survived the microtoming procedure without cracking. These samples were produced under tunnel conditions listed in Table 4.1. The reference ice sample, however, was accreted under wet icing conditions in order to form ice having a uniform, but high, density. The density of the reference sample was measured to be 900 kg/m^3 using the oil displacement technique whereby the sample was first weighed and its volume was determined by the amount of oil that was displaced. The error in the measurement was estimated to be 20 kg/m^3.

Each rime icing test was completed when the accretion attained a size that was compatible with the X-ray technique. Typically, a minimum stagnation line ice thickness of about 2.54 cm is required to produce a radiographic image large enough on which to perform density measurements with a microdensitometer. At the completion of each test, the ice sample was separated from the cylinder and stored in a room where the operating temperature was -12 °C. In the cold room, the rime and reference ice slices were microtomed to a uniform thickness of 1mm.

The next phase of the experiment consisted of placing a rime

Table 4.1 FROST tunnel conditions at which ice samples were produced on a cylinder for local ice density measurements.

Test #	D_d (μm)	U_∞ (m/s)	Ta (°C)	P_a (N/m^2)
1	17.1	20	-10	100,000
2	17.0	20	-14	100,000
3	18.4	10	-10	100,000
4	25.0	10	-15	100,000
5	18.7	30	-10	100,000

sample beside a reference ice sample on an X-ray film and exposing them to an X-ray beam. In setting up the X-ray technique, the two ice samples were placed flush on a 10 by 12.5 cm therapy verification film which was contained in a wooden tray used for handling purposes. The tray was placed on the floor of the lead box 60 cm from the anode and in a position such that when the X-ray beam is applied, it would be perpendicular to the plane of the samples and the sheet of film. This setup is shown in Plate 4.4.

The samples were irradiated with an X-ray beam generated at 60kv and 10ma, for 9 seconds. Following the exposure, the X-ray film was developed and the radiograph, consisting of two images, was clipped onto the specimen table of the microdensitometer, where the local film densities could be measured.

A beam of light scans the X-ray images along a straight line path and the effective illuminated area on the film was a 0.1 mm diameter light spot. For the rime sample, the area on its image representing the area on the sample closest to the cylinder surface was examined by the light beam. This provided an approximation for the local ice densities along the surface of the cylinder.

Plate 4.4 Positioning of X-ray film with respect to the X-ray tube.

5. EXPERIMENTAL RESULTS AND COMPARISON WITH MODEL PREDICTIONS

5.1 Rime Feathers

In Chapter 3, the stochastic model predictions of rime feather growth for several arbitrary collector geometries were examined. The model was found to be useful in estimating the growth angle of the feathers which were produced on cylindrical structures under various flow conditions. Although there was no doubt the model was capable of producing feathers on structures of arbitrary shape, there was concern over the accuracy of the model predictions of feather growth angles. In this section, the flow conditions under which rime feathers grow, in the real world, will be discussed. Then, the model predictions of Chapter 3 will be compared with growth angle measurements obtained from nine ice accretions produced in an icing wind tunnel. Any discrepancies between predicted and actual growth angles will be explained in terms of the assumptions made in the models.

Before making any growth angle comparisons, let us discuss a major assumption made in the stochastic models: droplets remain spherical upon impact. This has enabled the models to produce feathers on cylindrical structures under any flow condition. On ice accretions, however, rime feathers develop only when droplets freeze individually, with minimal deformation, following impact with a surface. This was concluded by Macklin (1962) who has used the quantity $(-rv_o/T_s)$ as an indicator of the tendency of droplets to freeze together as spheres. The parameters were previously defined in Section 2.3. Basically, in flow conditions where $(-rv_o/T_s)$ is relatively low, less than ten,

Macklin (1962) observed that droplets tended to freeze spherically on a surface, with little deformation. At the other extreme, with $(-rv_o/T_s)$ greater than about fifty, droplets tend to coalesce, splash, and run back along the surface of the ice deposit. There was a smooth transition in structural ice appearance from the white, distinctive rime feather growth, at low $(-rv_o/T_s)$, to the grey, clear, and featherless ice deposit, at high $(-rv_o/T_s)$. It is not known precisely what value for $(-rv_o/T_s)$ is the dividing line between droplets freezing individually and droplets coalescing, but it is estimated to be around ten (Macklin, 1962).

To observe whether $(-rv_o/T_s)$ could be related to the general appearance of accretions produced in the FROST tunnel, $(-rv_o/T_s)$ was calculated for each of the nine flow conditions of Table 3.2. The results are tabulated in Table 5.1. The v_o was calculated by, first, obtaining the normalized impact velocity at the stagnation point, V_1, from the curves of L & B (Figure 3.3(c)). Then V_1 was multiplied to U_∞. The mean surface temperature was calculated from the model of Lozowski et al. (1983). Plates 5.1 to 5.3 illustrate the cross-sections of the accretions grown in the tunnel. From these plates and Table 5.1, one would note that, although there was rime-feather development in each case, the feathers were more whitish and discrete when $(-rv_o/T_s)$ was less than about ten (Plates 5.1(a) and (b), 5.2(a), and 5.3(a)), similar to Macklin's findings. As $(-rv_o/T_s)$ increased, the accretions were feathery near the edges of the accretion but greyish near the stagnation point (Plates 5.1(c) and 5.2(b)). In fact, the feathers appeared greyish and were not clearly defined for values of $(-rv_o/T_s)$ greater than fifteen (Plates 5.2(c), 5.3(b), and

Table 5.1 Calculation of $(-r\upsilon_o/T_s)$ at various flow conditions.

	FROST TUNNEL CONDITIONS											MACKLIN
Test #	D_d (μm)	U_∞ $\frac{m}{s}$	T_a (°C)	P_a (N/m^2)	D_C/D_d	K	ϕ	V_l	υ_o $\frac{m}{s}$	T_s (°C)	T_o (°C)	$-r\upsilon_o/T_s$ $\frac{\mu m \cdot ms^{-1}}{°C}$
A	18.2	10	-15	1E05	1396	0.9	240	0.37	3.7	-12.9	-10.5	4.6
B	27.2	10	-15	1E05	934	1.9	240	0.57	5.7	-8.6	-0.9	6.8
C	36.9	10	-15	1E05	688	3.6	240	0.70	7.0	-6.3	0.0	9.2
D	17.4	20	-15	1E05	1460	1.6	480	0.50	10.0	-12.4	-9.4	8.7
E	30.3	20	-15	1E05	838	4.8	480	0.74	14.8	-6.6	0.0	15.2
F	36.4	20	-15	1E05	698	6.9	480	0.79	15.8	-4.5	0.0	18.2
G	17.7	30	-15	1E05	1435	2.5	720	0.61	18.3	-12.4	-8.9	13.2
H	27.3	30	-15	1E05	930	5.9	720	0.75	22.5	-6.2	0.0	20.4
I	32.4	30	-15	1E05	784	8.3	720	0.80	24.0	-4.8	0.0	24.3

(a) MVD = 18.2 μm

(b) MVD = 27.2 μm

(c) MVD = 36.9 μm

Plate 5.1 Cross-sections of ice accretions produced at U_∞ = 10 m/s and T_a = -15 °C.

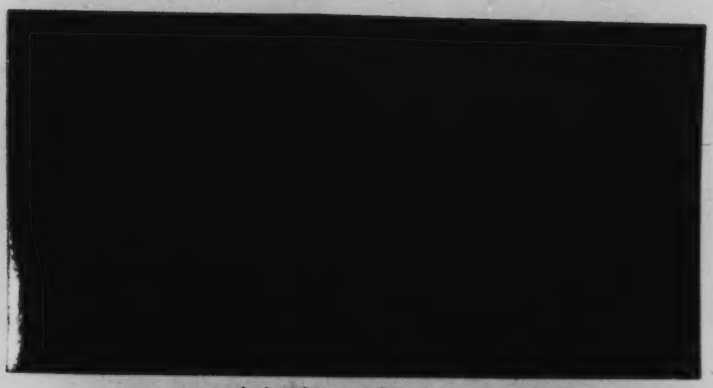

(a) MVD = 17.4 μm

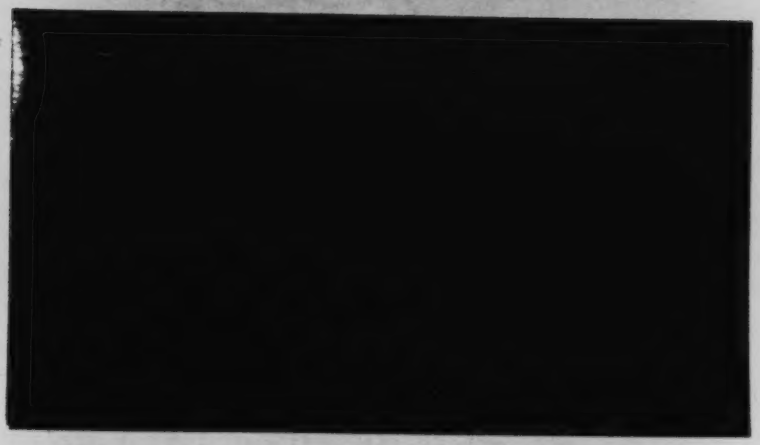

(b) MVD = 30.3 μm

(c) MVD = 36.4 μm

Plate 5.2 Cross-sections of ice accretions produced at U_∞ = 20 m/s and T_a = -15 °C.

(a) MVD = 17.7 μm

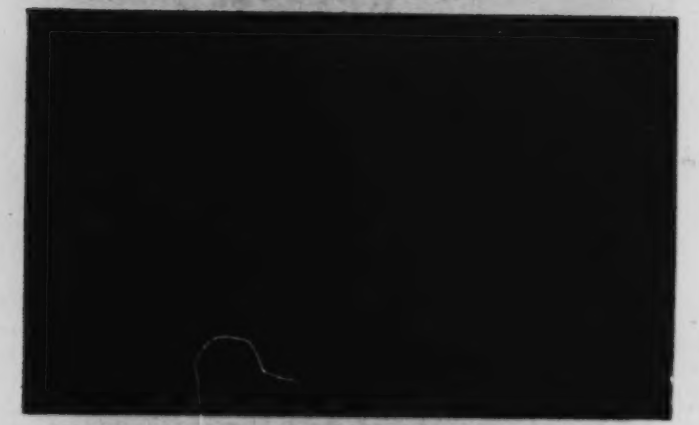

(b) MVD = 27.3 μm

(c) MVD = 32.4 μm

Plate 5.3 Cross-sections of ice accretions produced at U_∞ = 30 m/s and T_a = -15 °C.

5.3(c)). Table 5.1 also shows that wet icing occurred at the stagnation point (T_o = 0 °C) in five cases. In these cases, partial coalescence of droplets probably occurred with runback, and thus, produced greyish feathers. Inspite of droplet spreading activity, the growth direction of the feathers was still noticeable. Therefore, to assure rime feather growth, $(-rv_o/T_s)$ must be less than about ten. This could be accomplished by reducing the quantity rv_o or decreasing T_s. In either case, droplet deformation would be minimized, with enhanced spherical droplet accretions. Consequently, open structures of low density could be produced.

At this time, it should be realized that the observations and $(-rv_o/T_s)$ values presented, thus far, were general and pertain to the overall appearance of the ice accretion on a cylinder. A more appropriate quantity $(-rv_r/T_{su})$, applied to local areas, could be calculated for anywhere on the surface of the accretion. Low values of $(-rv_r/T_{su})$ would represent favorable areas in which rime feathers could develop. Here, v_r is the normal component of the droplet's impact velocity, referred to as the local impact speed, and T_{su} is the local surface temperature. In regions where v_r and T_{su} are moderately low, droplet spreading and freezing time would be reduced.

The value for v_r depends on the overall flow conditions. Simple fluid flow theory (Streeter and Wylie, 1979) shows that as air flows around a cylinder, the air velocity increases. This tends to speed up the droplet, increasing its velocity in the direction tangent to its trajectory. This also reduces the normal component of the impact speed from v_o at the stagnation point to some value v_r at a point on the cylinder further downstream. Therefore, v_r is minimal near the edges

of any ice accumulation.

The surface temperature T_{su}, on the other hand, is also minimal near the edges of the accretion. There, the curvature of the droplet trajectories is relatively high, and the trajectories are further apart from one another, resulting in infrequent impacts and preventing coalescence of droplets. In addition, the region is closer to the airstream than to the relatively warmer stagnation point. These two factors enhance spherical droplet accretions. Therefore, since $(-rv_r/T_{su})$ has the lowest value in the vicinity of the edges of the ice accretion, if they develop at all, rime feathers would be expected to grow there first. In fact, Plates 5.1 to 5.3 clearly illustrate that rime feathers grow solely near the edges.

With the favorable conditions for the growth of rime feathers established, the next step is to determine the accuracy of the model predictions of growth angles by comparing them with those measured on ice accretions. This comparison would aid in narrowing the set of flow conditions under which the model could provide accurate predictions of growth directions. From Section 3.2.2, the growth angle of the feathers from the curved trajectory model generally increases with droplet inertia. Basically, as the droplet inertia increases, the droplets follow increasingly straighter trajectories, producing feathers with positive growth angles. The growth angles were extremely sensitive to the curvature of the trajectories, provided the droplets remained spherical upon impact.

In the experimental situation, the results are not as predictable because the droplet distribution consists of droplets of variable size, and although droplet-spreading was minimized by the selection of the

appropriate flow conditions ($-rv_o/T_s$ optimized), the droplets will always deform to a certain degree. To observe the impact of these two factors, the growth angles of rime feathers were measured on nine different ice deposits and tabulated, along with stochastic model predictions, in Table 5.2.

From the table, one can immediately see that the range of the rime feather growth angle measurements was relatively small in comparison with that from the curved trajectory model (-7° to 11° versus -27° to 14°). More importantly, the growth angle measurements generally have a positive value. These observations suggest that the large droplets are the main contributors to rime feather growth. Let us investigate experimental tests A,D and G to explain this.

In tests A and D, the smaller droplets (< 18 μm) in the spectrum have high angles of attack, χ, but the droplets have low inertia (K < 0.9) and are easily carried away by the airstream. The larger droplets, on the other hand, have more inertia and are able to resist a change in direction - their paths could deviate from the path of the airstream and collide with the icing object. So, the large droplets from the spectrum would contribute more to the icing process near the edge of the accretions in tests A and D. This is confirmed by Table 5.2 results which show that the measured θ_m was greater than the predicted θ_m when the inertia parameter, K, was less than two. Because these large droplets have a much lower angle of attack than those of 18 μm droplets (the MVD), it is then not surprising that the rime feathers they form tend to point away from the stagnation line (8°).

As the windspeed increased, the smaller droplets, in the spectrum, have higher collision efficiencies and contribute more to the icing

Table 5.2 Model predictions and rime feather growth angle measurements (degrees) at various flow conditions. Straightline and curved trajectory models were produced with 20,000 and 10,000 droplets respectively.

	FROST TUNNEL CONDITIONS						GROWTH ANGLE, ψ			θ_m	
Test #	D_d (μm)	U_∞ (m/s)	T_a (°C)	P_a (N/m^2)	D_c/D_d	K	MODEL TYPE Simple (∓2°)	Curved (∓2°)	ACTUAL Expt (∓2°)	Curved traj. model	Expt (∓1°)
A	18.2	10	-15	1E05	1396	0.9	16	-27	8	45.5	62
B	27.2	10	-15	1E05	934	1.9	25	-5	8	59.9	60
C	36.9	10	-15	1E05	688	3.6	23	-1	8	68.7	64
D	17.4	20	-15	1E05	1460	1.6	15	-20	-3	54.3	64
E	30.3	20	-15	1E05	838	4.8	25	3	6.5	72.6	72
F	36.4	20	-15	1E05	698	6.9	23	13	11	76.7	72
G	17.7	30	-15	1E05	1435	2.5	15	-10	-7	62.3	60
H	27.3	30	-15	1E05	930	5.9	25	14	5.5	74.7	68
I	32.4	30	-15	1E05	784	8.3	20	9	11	78.3	75

process (test G) than the ones in tests A and D did. Since they have high angles of attack, and they outnumber large droplets from the spectrum, the small droplets make more surface collisions and form rime feathers with a relatively low angle of growth (-7°). This explains the decrease of growth angle with windspeed when dealing with a droplet spectrum with a relatively low MVD (< 18 μm).

Since a large percentage of small droplets (< 18 μm) contribute to the accretion process in test G, it is not surprising that, of the three tests (A,D, and G), measurements from test G were the closest to the predicted value (-7° vs -10°, with an error of 2° in the measurements). This is because, in this test, the curved trajectory model also assumed very small droplets formed the accretion (17.7 μm).

A second observation from the experimental results in Table 5.2 is that, by keeping the windspeed constant and increasing the MVD, the rime feathers grew at increasingly positive angles from the stagnation line. This is easy to see, because large droplets tend to follow straighter trajectories, as explained in Section 3.2.2.

Contrary to observations from tests A,D,and G, experimental tests C,F,and I show that as the windspeed increases, the rime feathers point increasingly away from the stagnation line. Possibly, when the MVD is large enough (> 30 μm), the droplet inertia is such that straight line trajectories prevailed, regardless of the curvature of the streamlines. As tests F and I show, the best agreement between model and experiment exists when droplet inertia is high. In test I, even though the droplet inertia was the greatest of the nine cases, the growth angle did not exceed 11°. Perhaps, this is because droplets have difficulty remaining spherical when impact speeds increase.

5.2 Local Ice Density

In Chapter 3, it was shown that the stochastic rime icing models produced structures of variable density. The structure of the curved trajectory model accretion was found to be relatively more porous than that formed by the straightline model at similar flow conditions. In this section, the accuracy of the stochastic models and that of the model of Bain and Gayet (1983), will be determined by comparing their predictions with X-ray measurements of local ice densities in ice accretions produced in the FROST tunnel. This analysis will lead to a comparison of the stochastic models with experimental results from Prodi (1985). Finally, based on model comparisons with experiment, a suitable empirical correlation for local ice density on a cylindrical collector will be sought.

5.2.1 Description of Model of Bain and Gayet

The only previous attempt to model the dependence of local ice density with angular position on a fixed cylinder was by Bain and Gayet (1983). In their formulation, they proposed that the local ice density $\rho(\theta)$ could be represented as a mean value of the discrete densities contributed by each of the droplet categories, from a real droplet spectrum, weighted by the liquid water content of these droplets:

$$\rho(\theta) = \frac{\sum_{j=1}^{n} \rho_j(\theta) \times G_j(\theta) \times f_j \times m_j}{\sum_{j=1}^{n} G_j(\theta) \times f_j \times m_j}$$

The droplet spectrum was assumed to be formed by n droplet categories, each characterized by a radius, r_j, a liquid water mass per droplet,

m_j, a local collection efficiency, $G_j(\theta)$, and a number, f_j, representing the fraction of droplets in the spectrum consisting of the jth size category. Now, $\rho_j(\theta)$ was calculated for each droplet category and assumed to be,

$$\rho_j(\theta) = \rho(r_j v_r(\theta)/T_{su}(\theta))$$

which is basically Macklin's assumption applied to local regions on the cylinder surface - recalling, Macklin assumed the bulk ice density on a rotating cylinder was related to the parameter $(-rv_o/T_s)$. In Bain and Gayet's model, $v_r(\theta)$ is the normal component of the droplet impact velocity, $V(\theta)$, calculated at the angle θ. i.e. $v_r(\theta) = V(\theta)\cos(\alpha)$, where θ and α are as previously defined. One could see that $v_r(\theta)$ varies from $v_o = V_1 U_\infty$, at the stagnation point, to 0 at the maximum impingement angle, θ_m, in accordance with theory. For any j, $G_j(\theta)$ and the normalized impact velocity at the stagnation point, V_1, could be obtained from the curves of Langmuir and Blodgett (1946). The local surface temperature, $T_{su}(\theta)$, and f_j could be determined from the model of Lozowski et al. (1983) and from the droplet spectrum respectively. When $r_j v_r(\theta)/T_{su}(\theta)$ was less than 10, Bain and Gayet used Macklin's equation,

$$\rho = 110(-rv_r/T_{su})^{0.76} \quad kg/m^3$$

to obtain $\rho_j(\theta)$; otherwise, a different expression for $\rho_j(\theta)$ was employed:

$$\rho = 1000(-rv_r/T_{su})/(-rv_r/T_{su} + 5.61) \quad kg/m^3$$

5.2.2 Model Predictions Versus Experiment

In the experimental tests, local ice densities were measured successfully from five different ice samples. The accretions are shown in Plates 5.4 and 5.5. The microdensitometer traces are provided in Figures 5.1(a) to (e), along with the respective pictures of the radiographs with the path of the densitometer beam illustrated. The calibration technique outline in Section 4.2 was perfomed to produce an absolute ice density scale for direct density read-off. The reference ice density (900 $\mp$ 20 kg/m^3) was the standard density used in the calibration.

Local ice densities from each test were obtained from Figure 5.1 and plotted along with model predictions in Figures 5.2(a) to (e). Before analyzing these plots, there are several items worthy of note. Firstly, the area of examination on the x-ray images of the thin ice slices were slightly away from the cylinder surface, and the densitometer scan was in a linear direction; this limits the range of angular positions in which density measurements were obtained to only $\mp$ 30° from the stagnation line, approximately half of θ_m in some of the tests. Also, the radial distances of these measurements ranged from 2.8 cm to 3.2 cm from the center of the cylinder, as Figure 5.3 indicates. Secondly, the experimental densities in Figure 5.2 are averaged values, obtained by drawing smooth curves through the small fluctuations in the traces from Figure 5.1. This is done because we are interested in the general variation in density along the surface of the cylinder. Thirdly, due to the symmetric nature of the accretions, density measurements from only half of the rime sample image were used for comparison with models. This half is indicated on the traces by

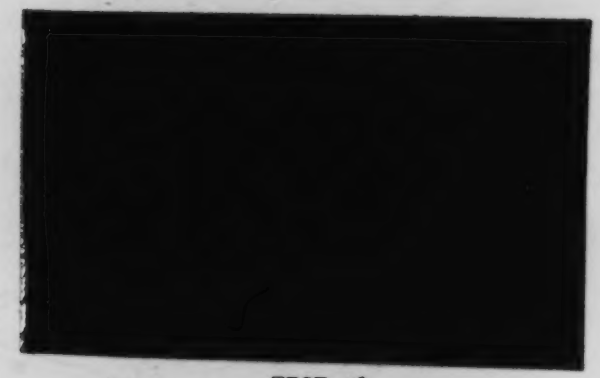

TEST #1

TEST #2

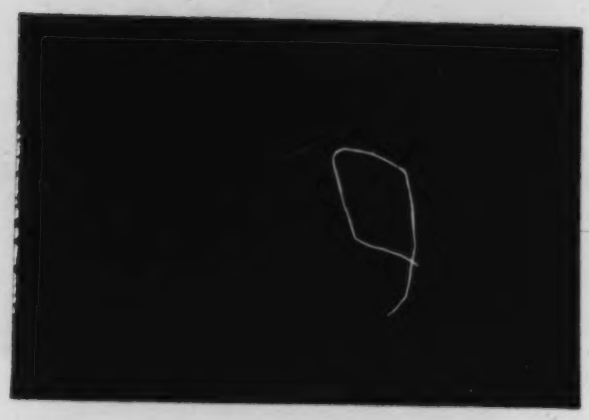

TEST #3

Plate 5.4 Ice accretions from tests 1-3 in Table 4.1.

TEST #4

TEST # 5

Plate 5.5 Ice accretions from tests 4 and 5 in Table 4.1.

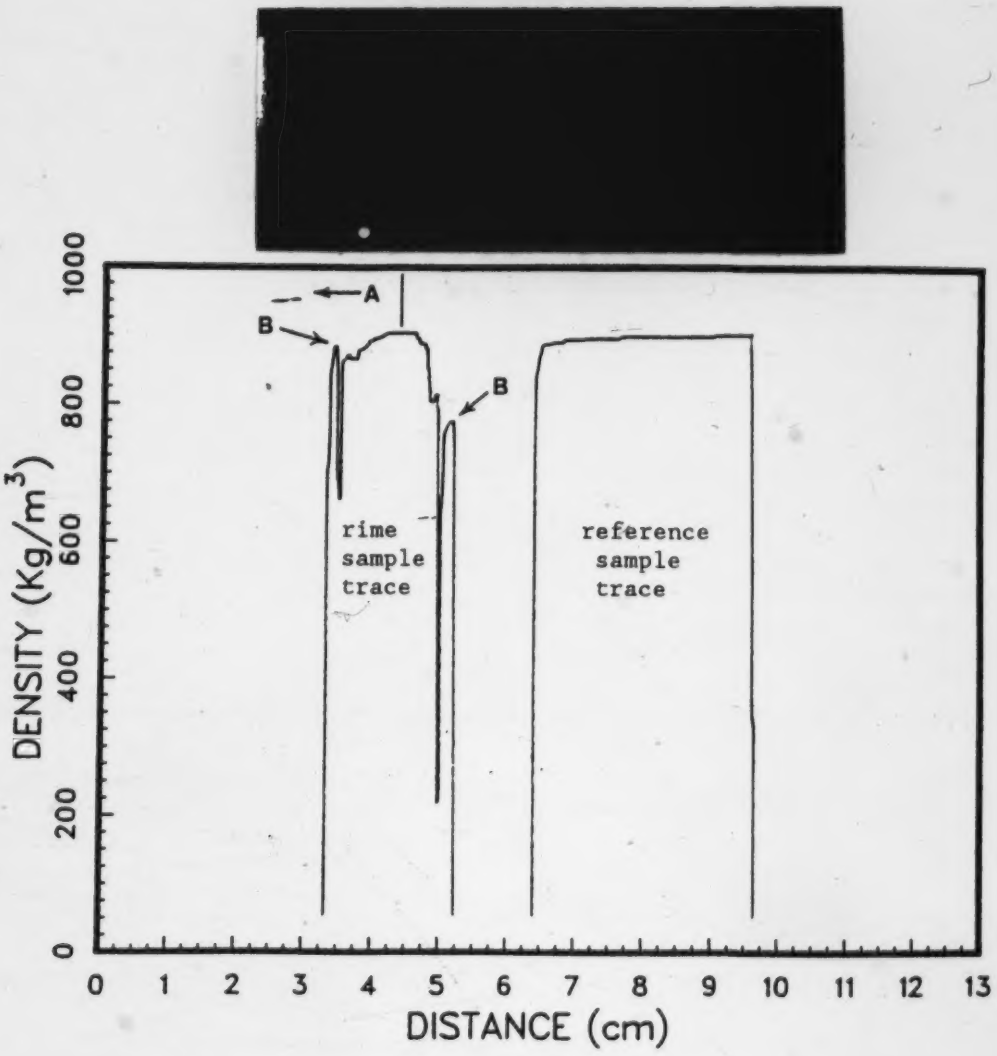

Figure 5.1(a) Densitometer trace for test #1.

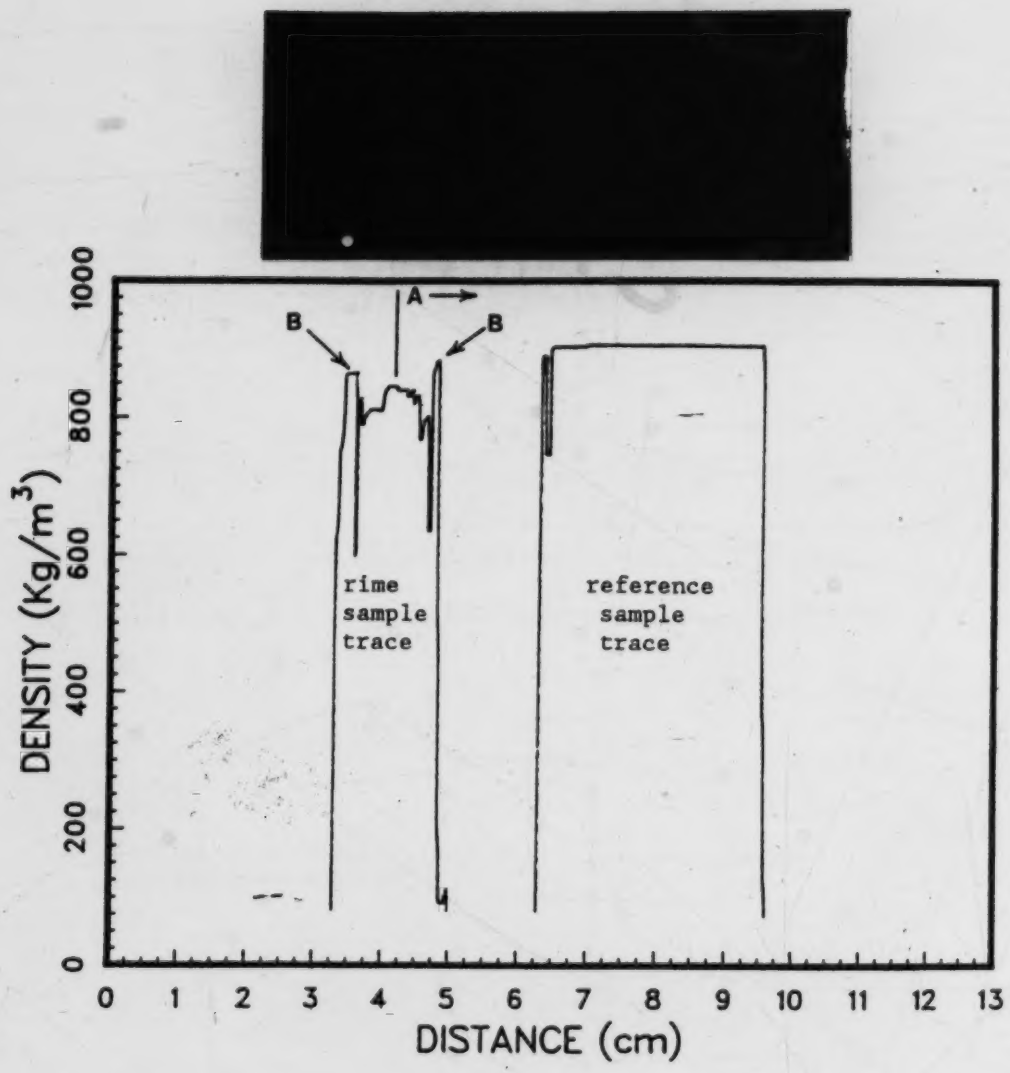

Figure 5.1(b) Densitometer trace for test #2.

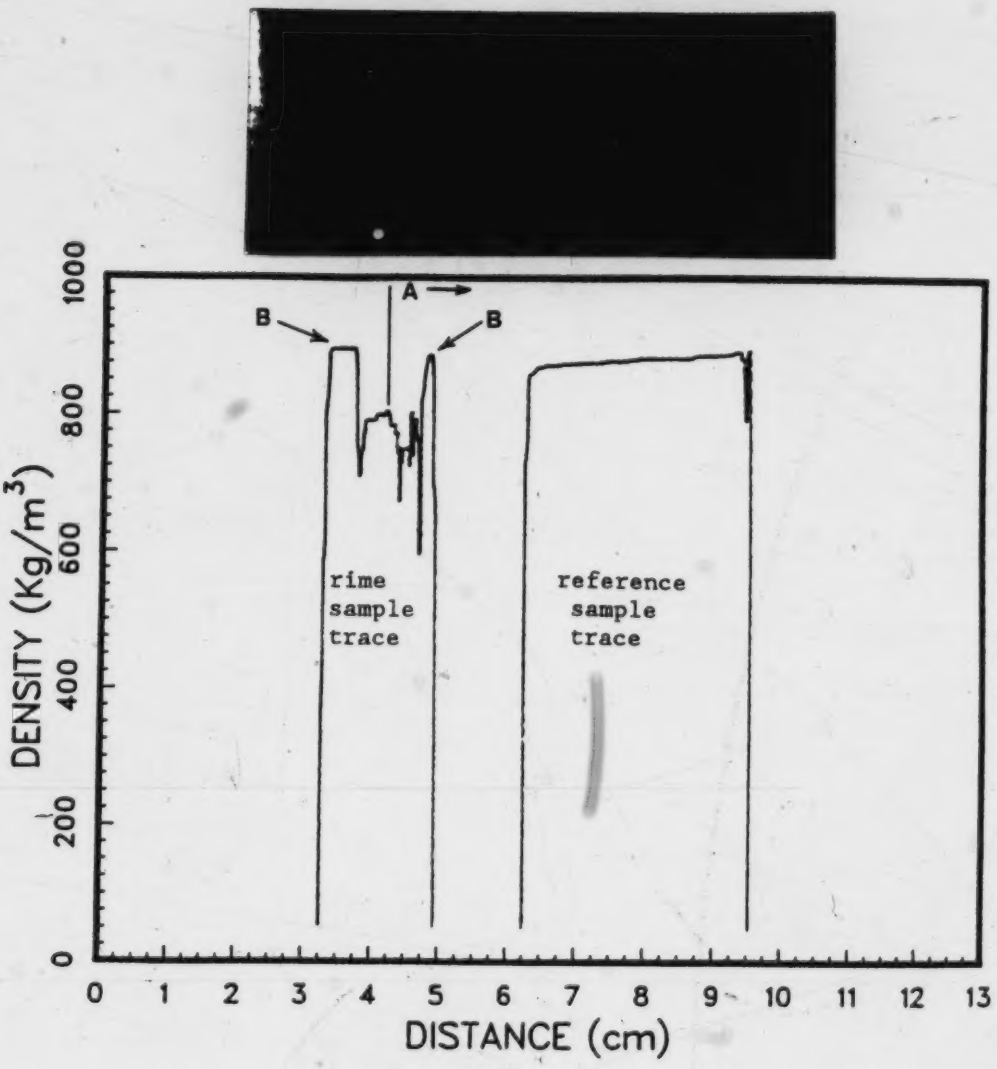

Figure 5.1(c) Densitometer trace for test #3.

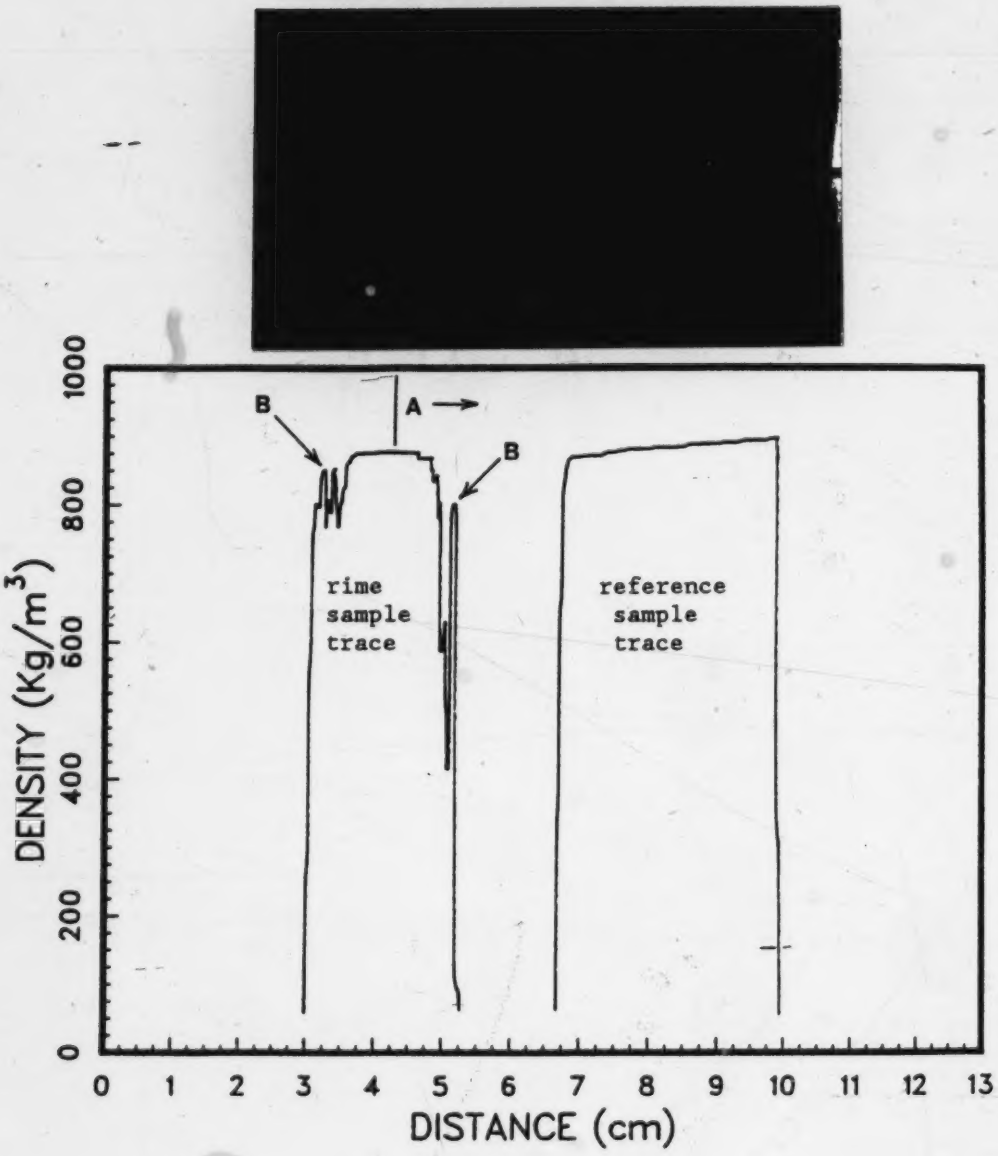

Figure 5.1(d) Densitometer trace for test #4.

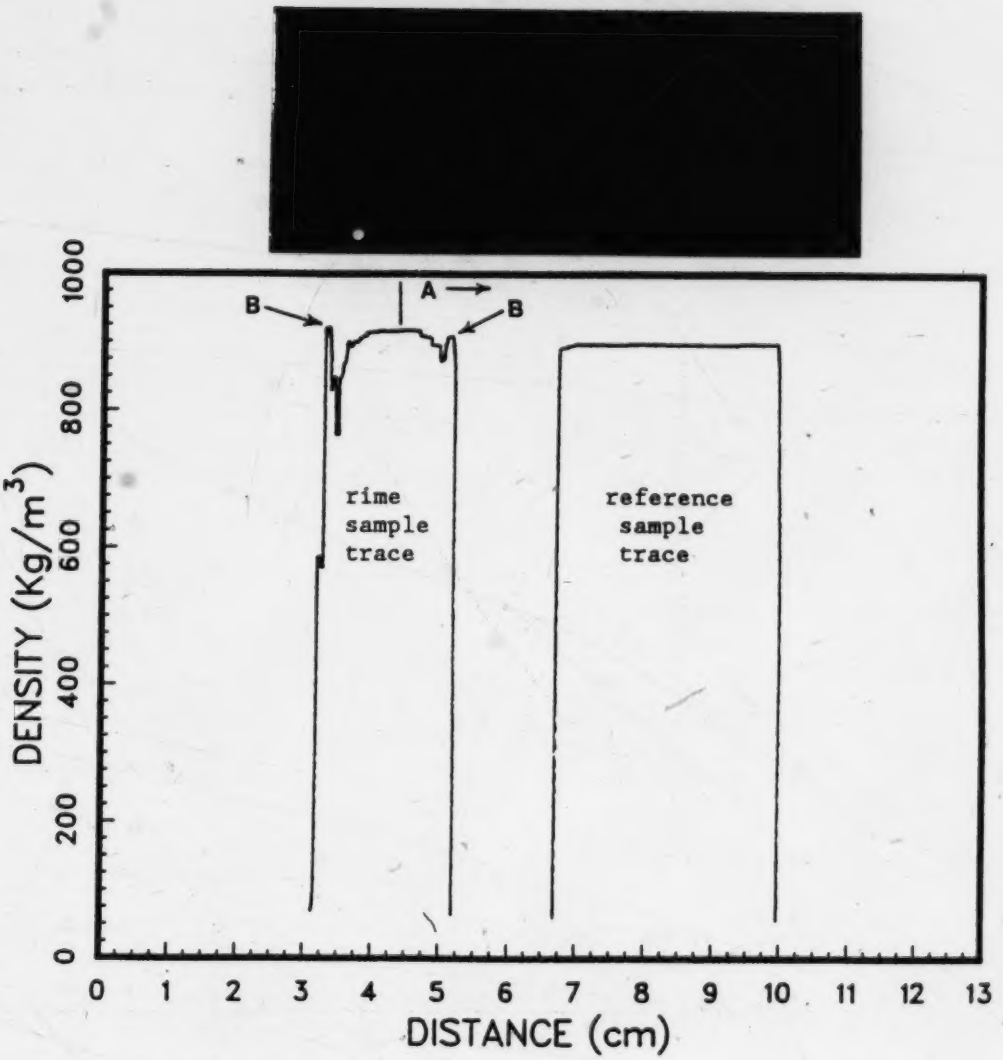

Figure 5.1(e) Densitometer trace for test #5.

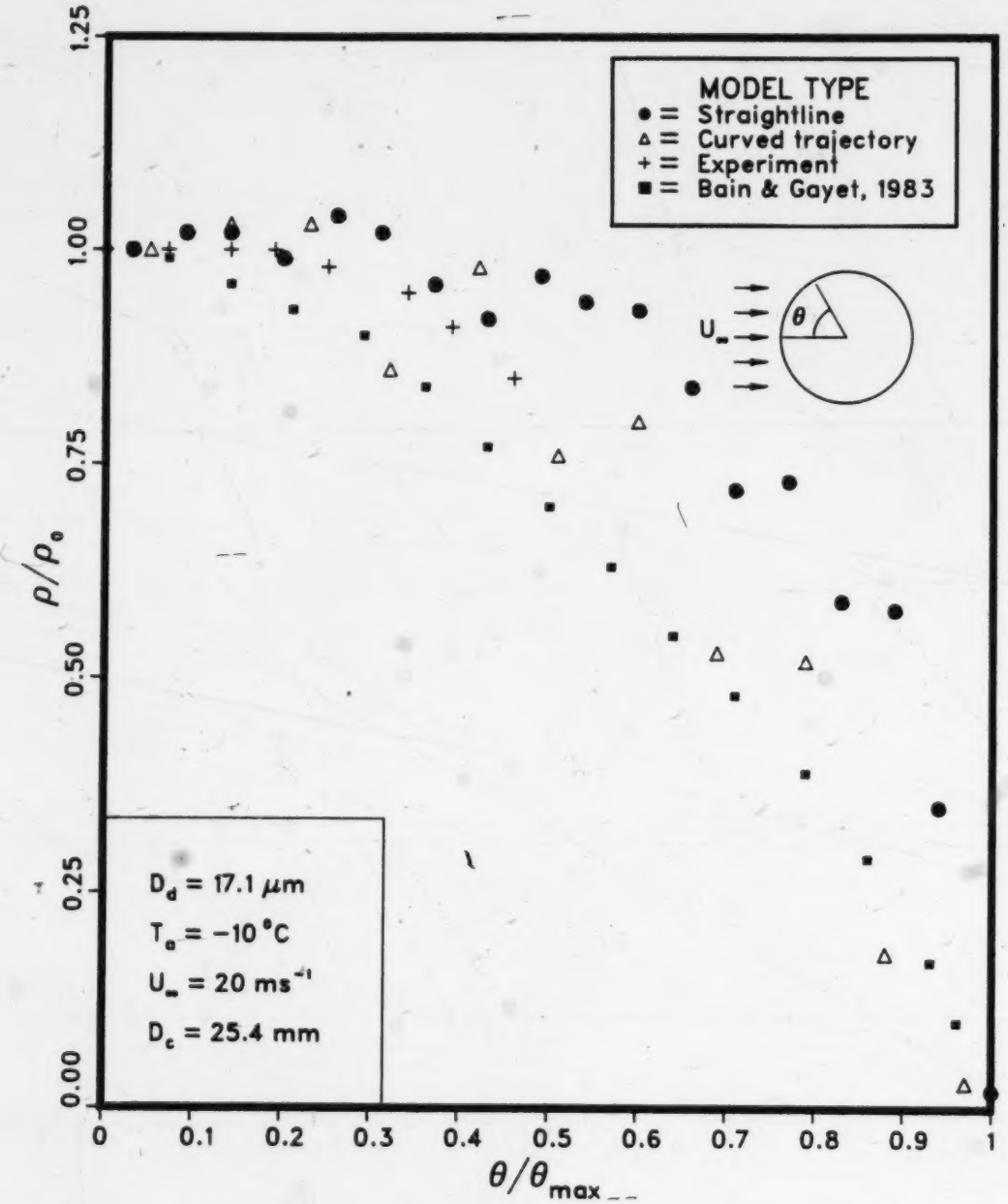

Figure 5.2(a) Comparison between experiment and several models at test condition #1.

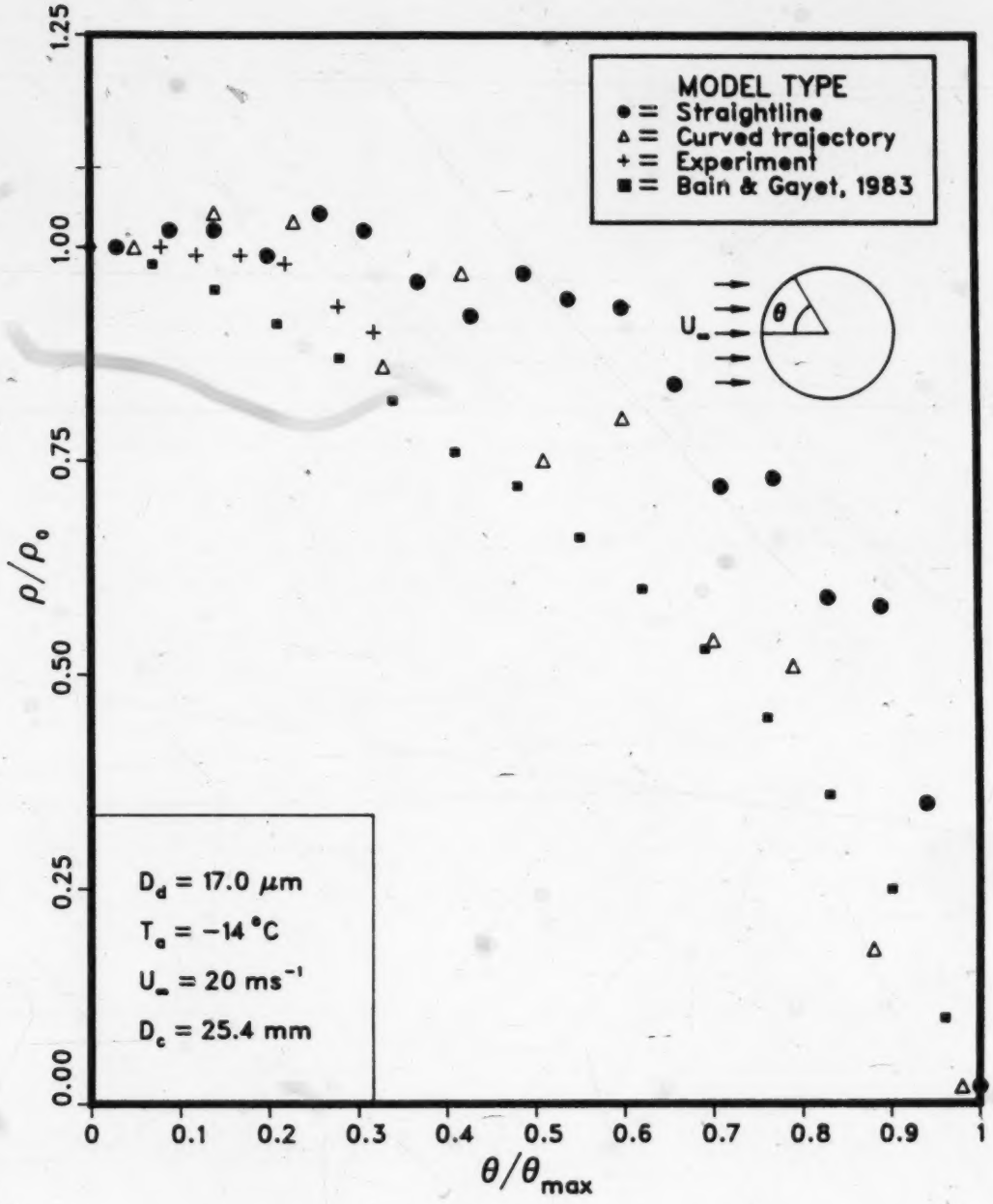

Figure 5.2(b) Comparison between experiment and several models at test condition #2.

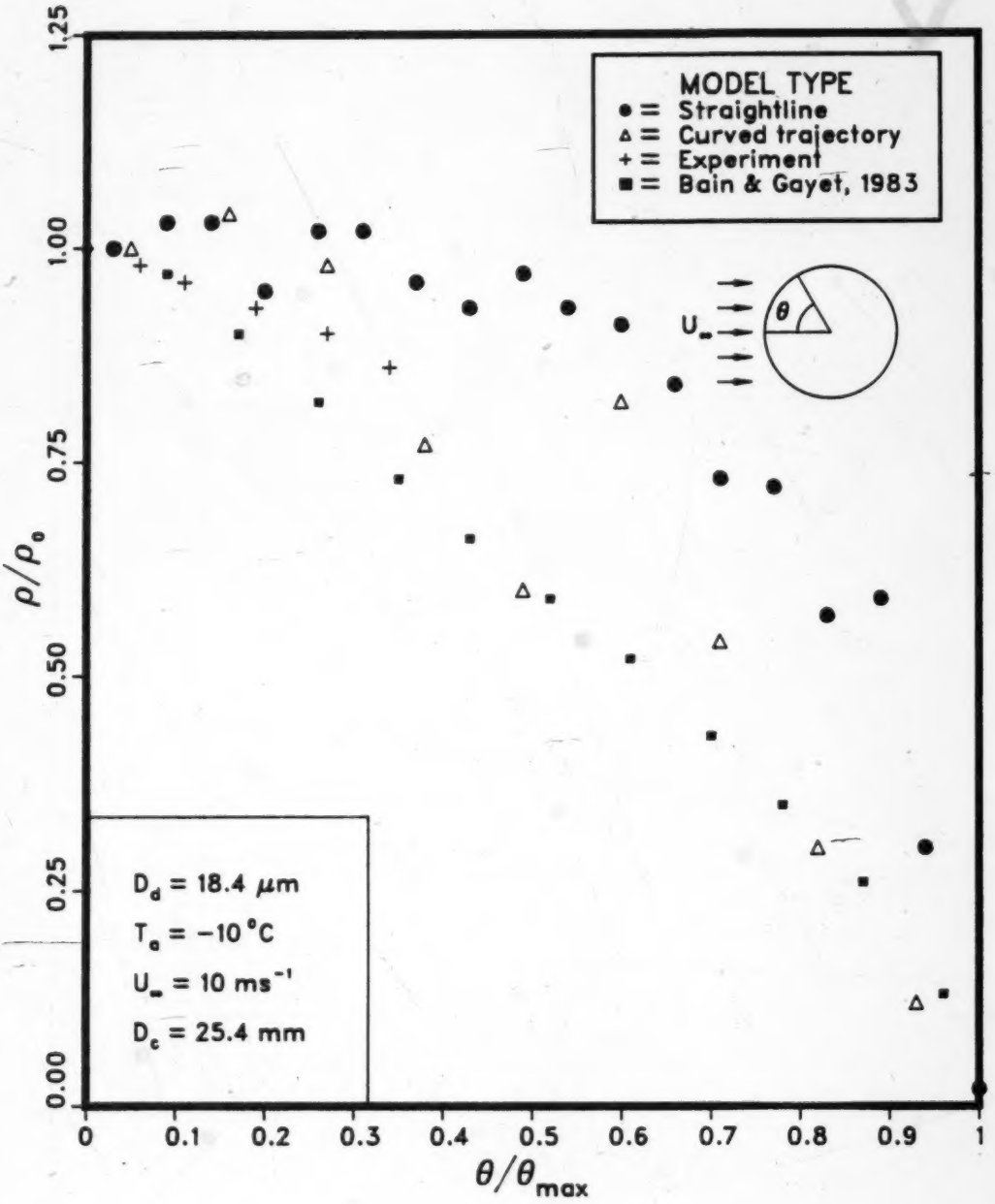

Figure 5.2(c) Comparison between experiment and several models at test condition #3.

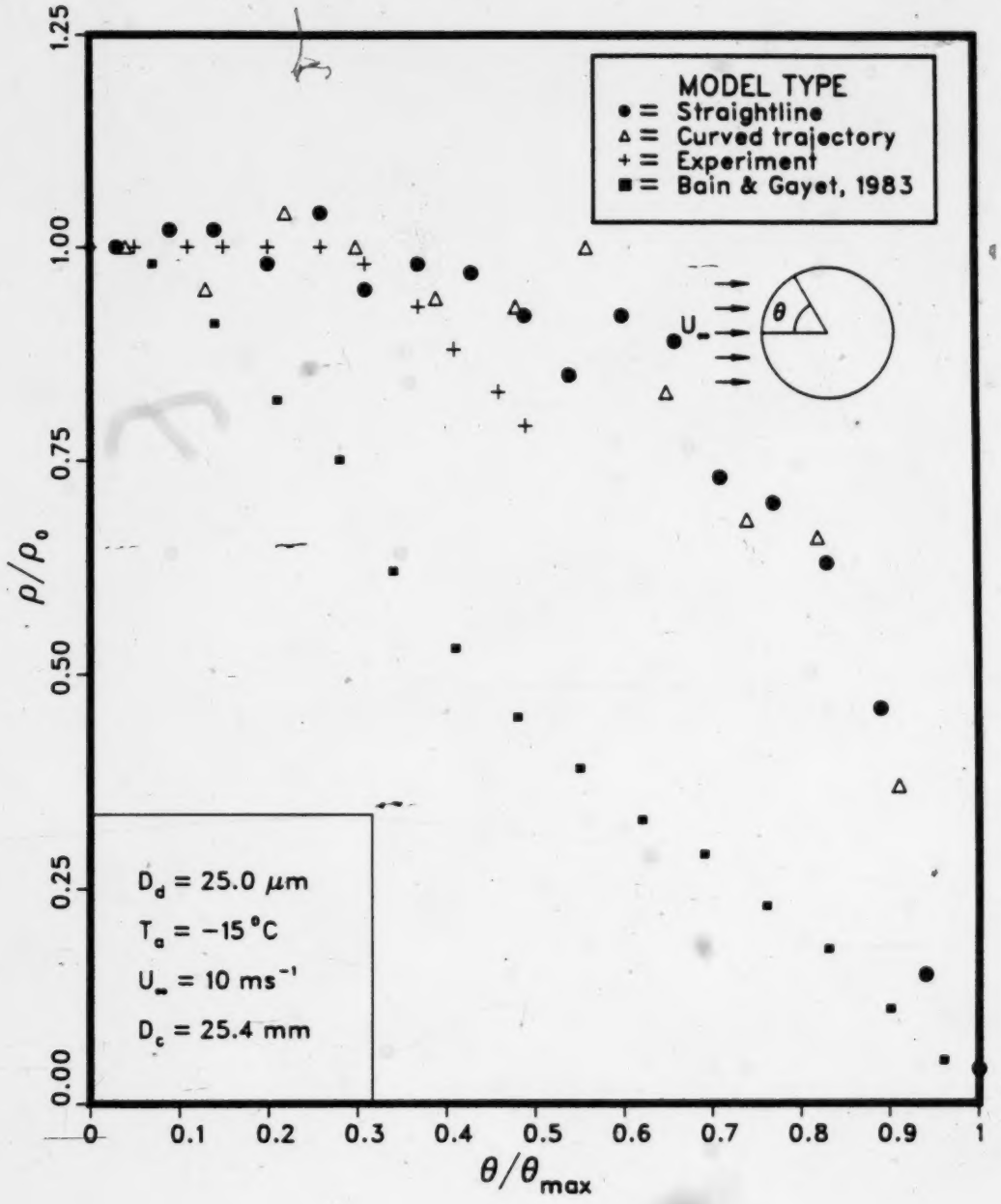

Figure 5.2(d) Comparison between experiment and several models at test condition #4.

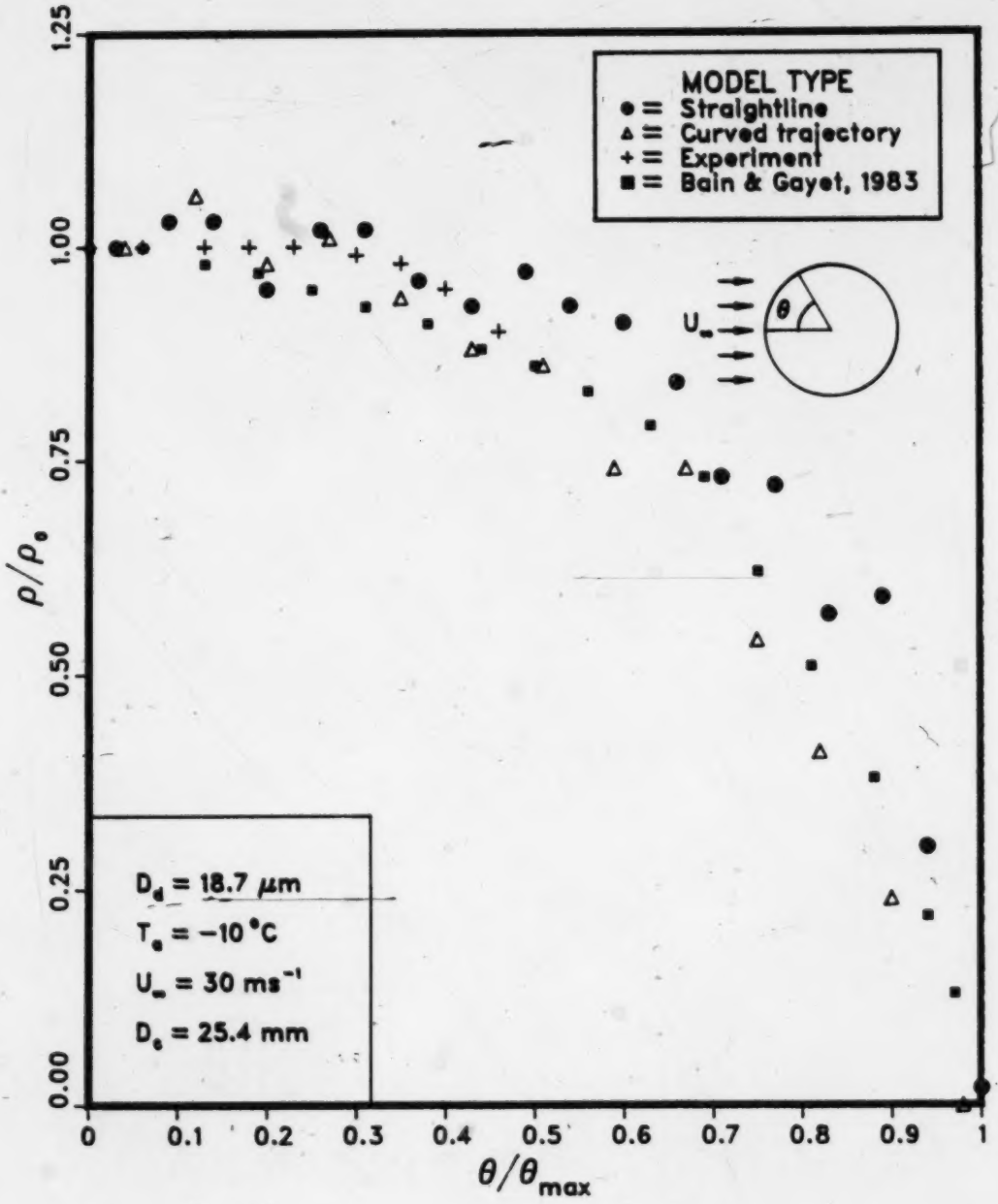

Figure 5.2(e) Comparison between experiment and several models at test condition #5.

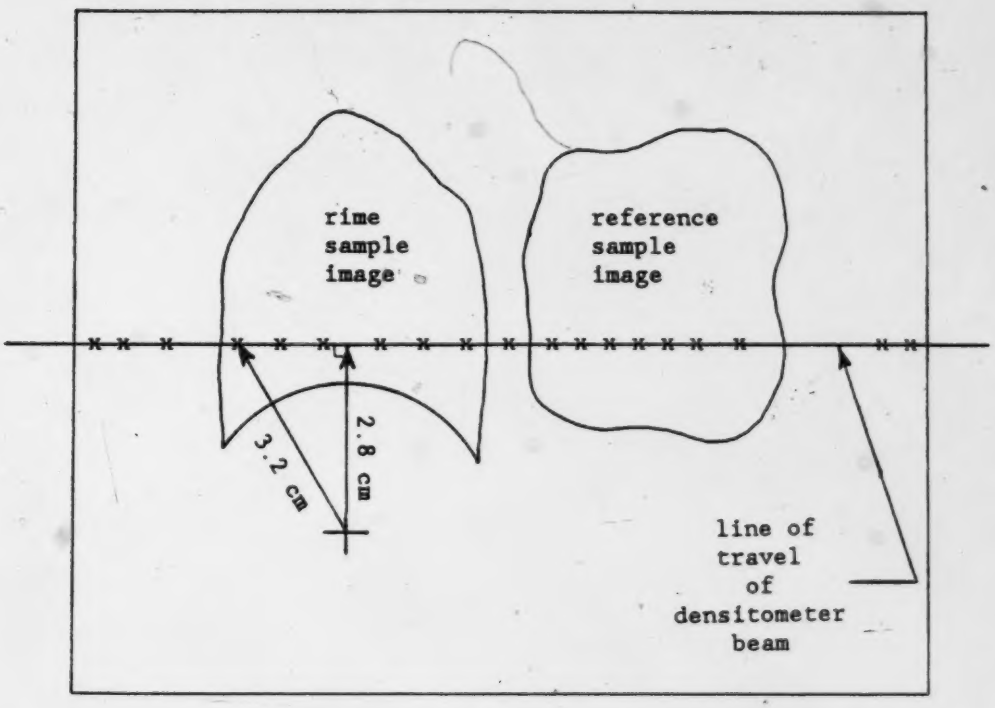

Figure 5.3 Areas (denoted by x) on the ice sample images from which densities were obtained.

the letter A with an arrow. Finally, the edges of the rime sample traces were omitted, because they represent densities of the bondfast glue. These areas are located on the traces with the letter B.

The three models were produced with a monodisperse spectrum. For Bain and Gayet's model, then, the density formulation is reduced to $\rho(\theta) = \rho_J(\theta)$. Figure 5.2 shows that, in the actual ice accretions, the maximum ice density is in the area of the stagnation point. Thereafter, the ice density generally decreases along the cylinder surface, reaching a minimum value at the accretion edges. This result agrees with the type of density variations found in the models. In fact, the five experimental results fall in the region bounded by the model predictions. The reasons for this will be explained shortly, but the results by Bain and Gayet should be excluded from the remainder of the discussion because they used density results from a rotating cylinder and applied them in their formulation for local ice density. One would expect the density of the accretion on a rotating cylinder to be uniform since the droplets are distributed uniformly over the entire icing surface. Therefore, Bain and Gayet's predictions represent averaged values and should not be used for further comparison in this study. Therefore, only the stochastic model predictions will be compared with the experimental results.

Figure 5.2 shows that the closest agreement between experiment and the straightline model results occurred in case #5. There, the ice density was uniform along the cylinder surface, up to θ/θ_m equal to about 0.3, before declining. As mentioned earlier, the surface of the cylinder near the stagnation point is approximately normal to the trajectories ($\alpha \approx 0°$) in a straightline model. The collection of

droplets on such a surface is analogous to the accretion of droplets on a vertical flat plate - minimal droplet shading activity occurs and the resulting accretion density is expected to be uniform. In the actual ice accretions, when the icing is dry, the uniform density results from droplet spreading activity near the stagnation point, provided the impact velocity and local surface temperature are moderately low. Table 5.3 shows that the quantity $-rv_o/T_o$ was quite high for case #5 ($\approx$32). Since the median volume radius, r, and the stagnation point temperature, T_o, were relatively small and below zero respectively, it was the high impact speeds (v_o = 19 m/s) of the droplets that probably led to the occurence of droplet spreading upon collision. When droplets spread, they have a tendency to fill nearby vacancies and produce a relatively dense structure.

The deformation of droplets also occurred in case #4 but, unlike case #5, v_o was relatively low (5.5 m/s). Table 5.3 clearly indicates T_o was -1.3 °C. Wet icing conditions exist in areas where the surface temperature is about 0°C, resulting in partial water runback along the icing surface. This has the effect of smearing droplets onto the surface, creating a dense ice structure, free from air entrapment. Therefore, in this case, uniform density in the vicinity of the stagnation point is the result of wet icing in that region.

An interesting case is that of number three (Figure 5.2(c)) where the experimental results are closely matched by the curved trajectory model predictions. The ice density at the stagnation point was the lowest in this case ($\approx$ 780 kg/m^3 $\mp$ 20 kg/m^3), which was expected, because $-rv_o/T_o$ (6) was the lowest for this case, indicating minimal droplet spreading activity. The v_o (3.9 m/s) and MVD (18 μm) were also

Table 5.3 Various parameters calculated for the experiments performed in the FROST tunnel.

	FLOW CONDITIONS					LANGMUIR & BLODGETT			MODEL		MODEL		LOZOWSKI			MACKLIN		X-RAY
CASE	D_d	U_∞	T_a	P_a	LWC	K	ϕ	V_l	θ_m	E_m	θ_m	E_m	T_s	T_o	v_o	$-\frac{rv_o}{T_s}-\frac{rv_o}{T_o}$		ρ_o
#	(μm)	$\frac{m}{s}$	(°C)	$\frac{N}{m^2}$	$\frac{g}{m^3}$				(°)		(°)		(°C)	(°C)	(m/s)	$\frac{\mu m \bullet m}{s \bullet °C}$	$\frac{\mu m \bullet m}{s \bullet °C}$	$\mp 20\frac{kg}{m^3}$
1	17.1	20	-10	1E05	0.50	1.55	299	0.51	54	0.37	54.1	0.38	-8.0	-5.6	10.2	10.8	15.5	909
2	17.0	20	-14	1E05	0.35	1.54	302	0.51	54	0.37	53.8	0.37	-12.6	-10.9	10.2	6.9	8.0	853
3	18.4	10	-10	1E05	0.8	0.89	149	0.39	46	0.26	45.5	0.26	-8.1	-6.0	3.9	4.4	6.0	785
4	25.0	10	-15	1E05	2.23	1.68	152	0.55	58	0.40	57.6	0.42	-8.5	-1.3	5.5	8.1	52.9	872
5	18.7	30	-10	1E05	0.36	2.77	447	0.64	65	0.51	63.7	0.51	-8.2	-5.7	19.2	22.0	31.7	917

relatively low, enhancing spherical droplet accretions. Also, the small droplets tend to follow the airstream. Since the physics of the accretion process resembled those in a curved trajectory model, it is not surprising the model provided a better agreement with experiment than the straightline model did, for this test.

The remaining two cases in Figure 5.2 are extremely interesting, because there is a fine line between the two. In case #1, the ice density was uniform near the stagnation point, but only up to θ/θ_m about 0.2. The density in case #2, however, decreased steadily as θ/θ_m increased from zero. Table 5.3 shows that rime icing prevailed in both cases ($T_o < 0°C$) and their $-rv_o/T_o$ values were much lower than those of cases #4 and #5. The major difference between cases #1 and #2 is their T_o values. Hence, it appears that the border line distinguishing uniform and nonuniform ice density near the stagnation point lies in the critical value for $-rv_o/T_o$, which appears to be between eight and fifteen and a half.

In an effort to confirm this, a comparison of model predictions with three sets of experiments by Prodi (1985) is presented in Figures 5.4(a) to (c). These results are the only ones made available by Prodi to date. The mean volume radius of the droplet spectrums were 15 μm, and this was assumed to be the droplet size in the models. Because θ_m was not available, θ/θ_m was not calculated for each case. Inspite of this, the figures clearly depict that, whether the actual ice density is uniform or not near the stagnation point depends on the value of $-rv_o/T_o$. Specifically, Figure 5.4 and Table 5.4 show that the curved trajectory model provides good agreement with experiment in conditions where $-rv_o/T_o$ is less than about 6; otherwise, the

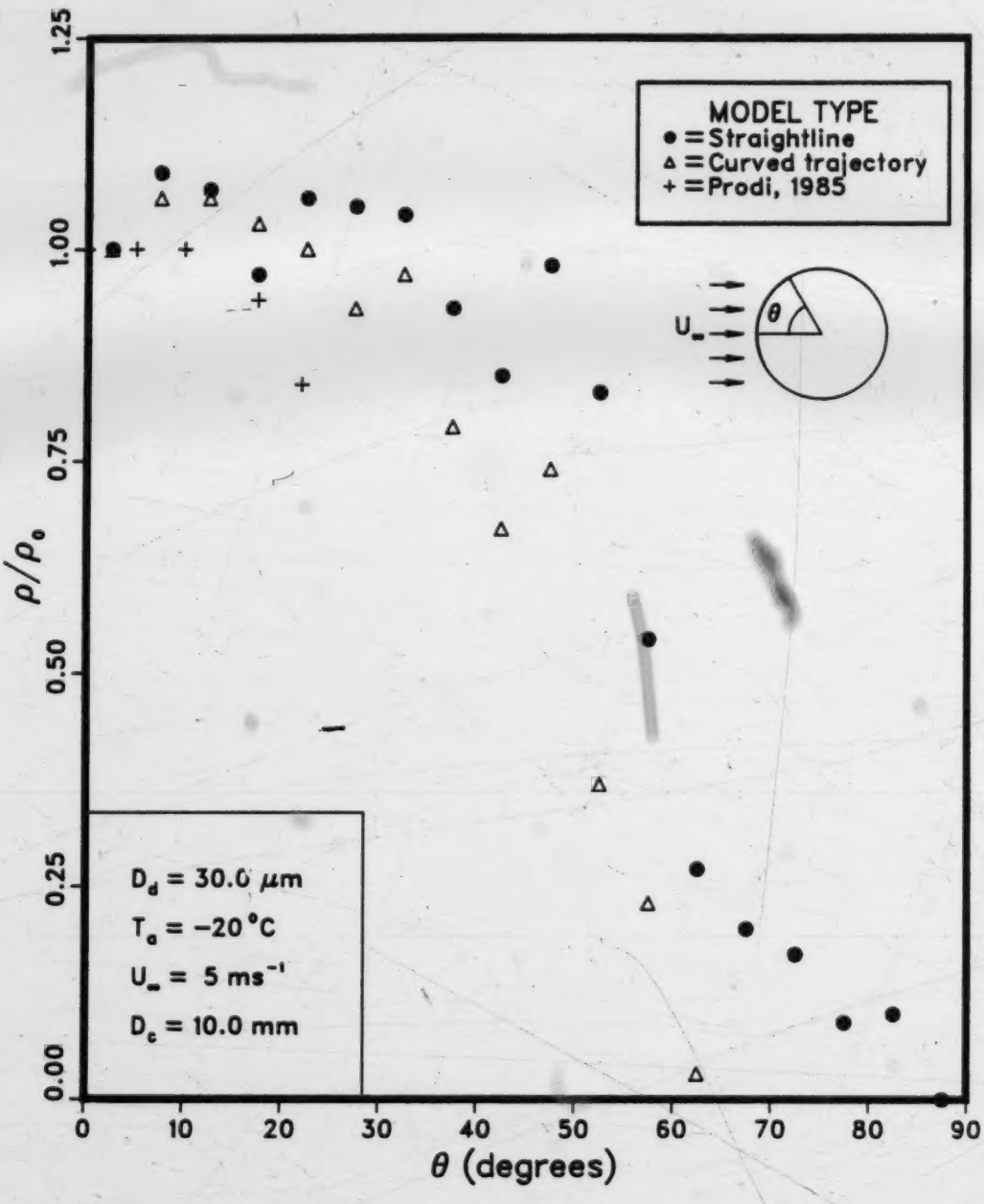

Figure 5.4(a) Comparison between Prodi's results and the stochastic models at test condition I from Table 5.4.

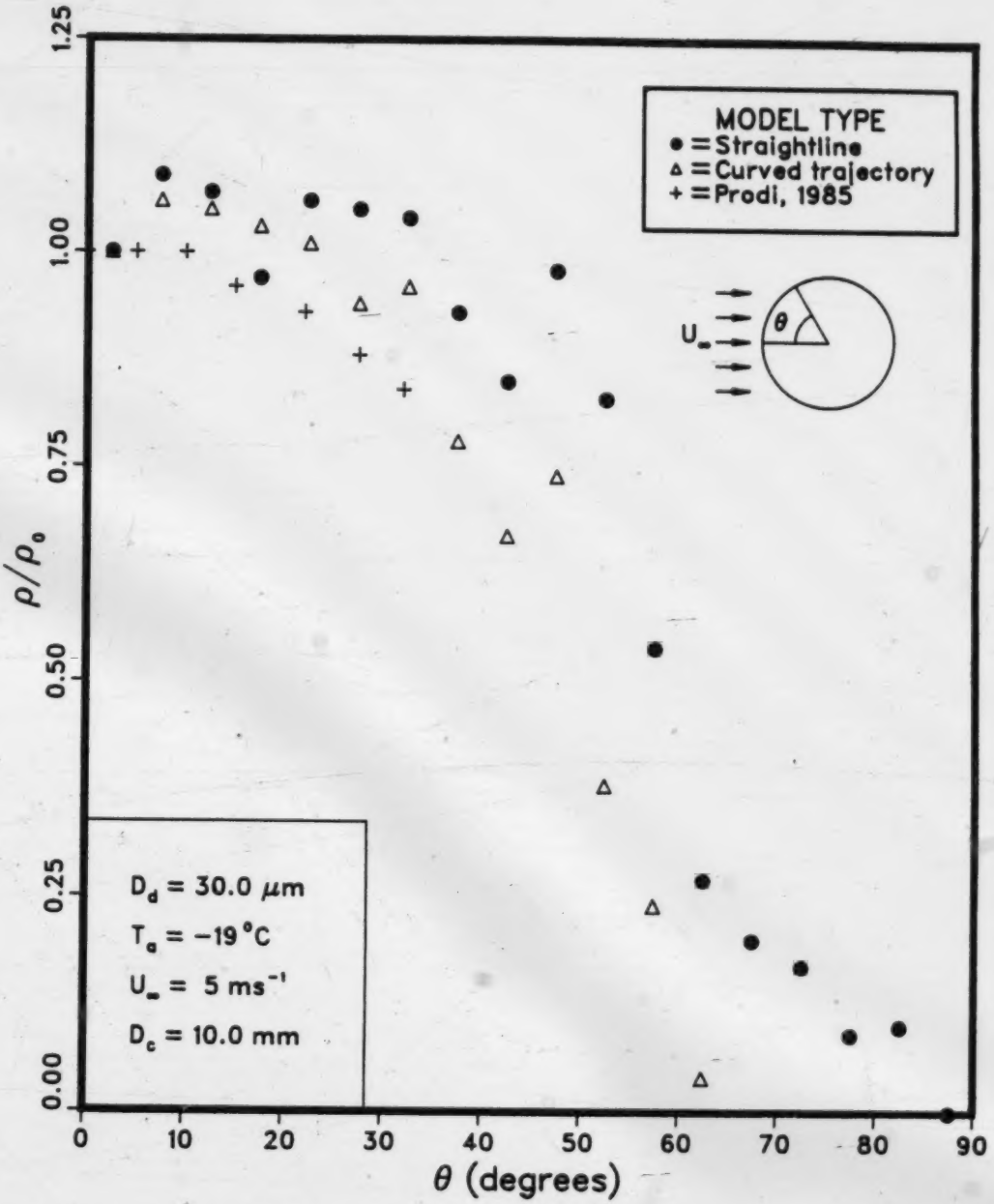

Figure 5.4(b) Comparison between Prodi's results and the stochastic models at test condition II from Table 5.4.

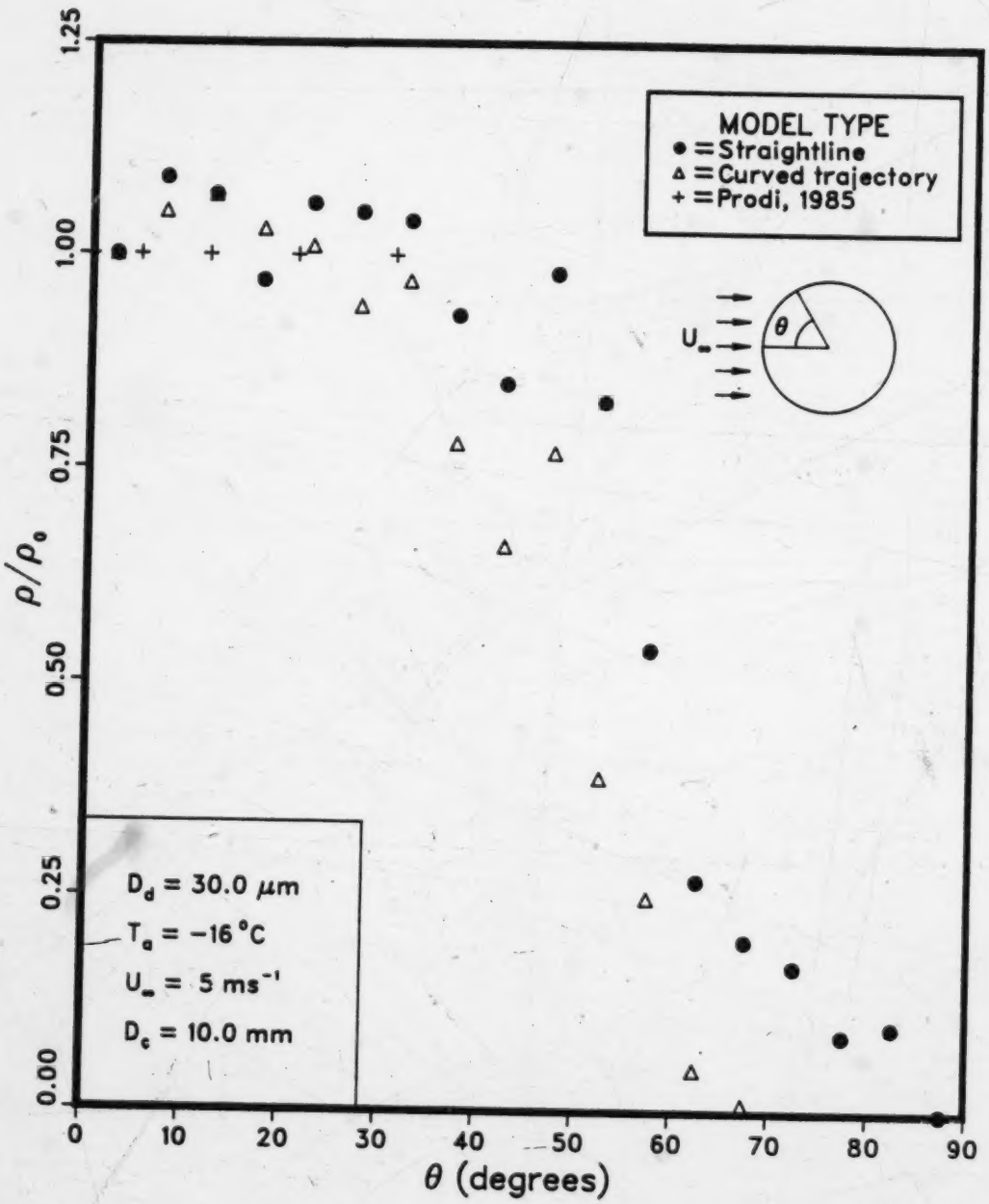

Figure 5.4(c) Comparison between Prodi's results and the stochastic models at test condition III from Table 5.4.

Table 5.4 Various parameters calculated for the experiments performed by Prodi (1985). The ice accretions were grown on a 1 cm diameter cylinder.

	FLOW CONDITIONS					LANGMUIR & BLODGETT MODEL							LOZOWSKI			MACKLIN		X-RAY
Test	D_d	U_∞	T_a	P_a	LWC	K	ϕ	V_1	θ_m	E_m	θ_m	E_m	T_s	T_o	v_o	$-\frac{rv_o}{T_s}$	$-\frac{rv_o}{T_o}$	ρ_o
#	(μm)	$\frac{m}{s}$	(°C)	$\frac{N}{m^2}$	$\frac{g}{m^3}$				(°)		(°)		(°C)	(°C)	(m/s)	$\frac{\mu m \bullet m}{s \bullet °C}$	$\frac{\mu m \bullet m}{s \bullet °C}$	$\frac{kg}{m^3}$
I	30.0	5	-20	1E05	1.5	3.1	53	0.74	71	0.6	64.5	0.62	-17.4	-13.6	3.7	3.2	4.1	620
II	30.0	5	-19	1E05	1.5	3.1	52	0.74	71	0.6	64.5	0.62	-16.5	-12.6	3.7	3.4	4.4	695
III	30.0	5	-16	1E05	1.5	3.1	51	0.74	71	0.6	65.5	0.61	-13.6	-9.9	3.7	4.1	5.6	917

straightline model provides a better agreement.

Because the straightline model provides accurate predictions of density variations in cases where $-rv_o/T_o$ is greater than or equal to 6, it is useful to obtain a correlation for density for these flow conditions. In Figure 5.5, the simple model predictions, for three different D_c/D_d values, were fitted with the curve having the equation,

$$\frac{\rho}{\rho_o} = \frac{76 - \exp(4.2\theta/\theta_m)}{75}$$

The coefficients of scatter in the vertical direction were 0.1, 0.06, and 0.05 for cases with D_c/D_d equal to 508, 1000, and 2540 respectively. The largest error (0.1) occurred in the case where D_c/D_d was 508. This corresponds to about 90 kg/m^3 if ρ_o was 900 kg/m^3. The empirical correlation is expected to be valid only for $D_c/D_d \geq 508$, in which cases the assumption of spherical droplet accretions is most likely. In cases #1,2,4, and 5 from the FROST tunnel experiments, and III from Prodi, in the area where the ice density was measured to be uniform (θ/θ_m up to about 0.25), the straightline model predictions were not greater than 3% from the measured values. This corresponds to an error of about 30 kg/m^3. The model predictions were off by as much as 15% in some cases, as θ/θ_m increased to about 0.4 - an error of about 140 kg/m^3. With the above correlation, all that is required is ρ_o. Makkonen (1984) proposed that the following relationship could be used to estimate ρ_o,

$$\rho = 0.378 + 0.425(\log R) - 0.0823(\log R)^2 \ g/cm^3$$

where,

$$R = -rv_o/T_s$$

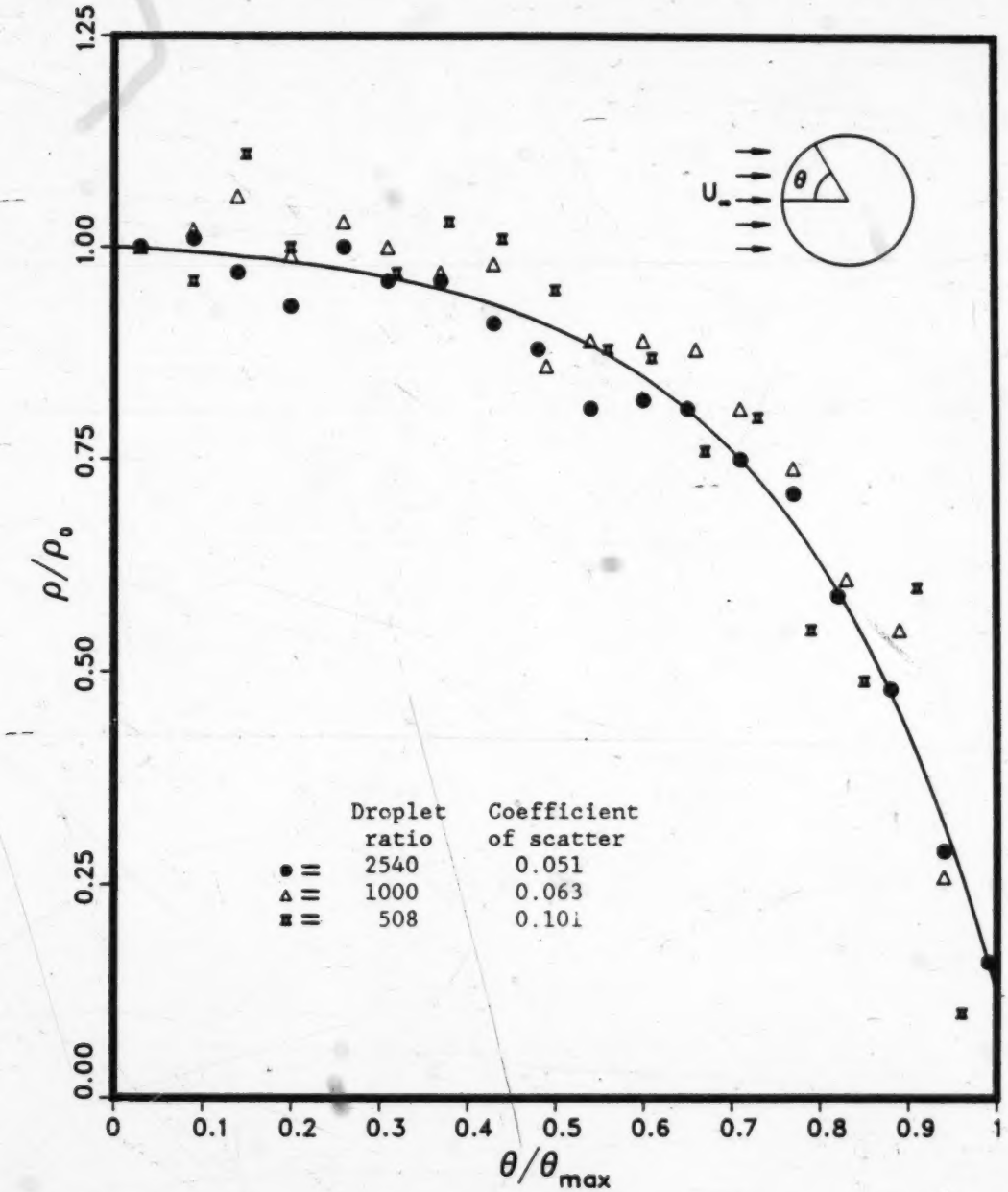

Figure 5.5 Curve fit for several straightline model predictions.

All parameters are defined as previously. Table 5.5 shows typical ρ_o values obtained with this equation for the 8 experimental cases. The calculated values were significantly different from the measured values, but the calculated densities were in the same proportion from test to test as the measured densities were. Perhaps the absolute stagnation point density by Makkonen is an averaged value, because it was obtained from experiments with a rotating cylinder.

In conditions where $-rv_o/T_o < 6$, in the FROST tunnel and in Prodi's tests, the density was nonuniform near the stagnation point, and the curved trajectory model was a better predictor of density. Because this model's predictions vary with flow conditions, unlike the behavior of the simple model, it is not easy to determine a correlation for density that would be a representative for all the curved trajectory model predictions. Despite this, the agreement between model and experimental cases #3 from the FROST tunnel, and I and II from Prodi, were within 3%.

Regardless of which stochastic model is being concerned, once a correlation is found, it would be ideal to be able to produce ρ_o directly from a stochastic model, for use with the correlation. In flow conditions where $-rv_o/T_o$ is less than ten, a relationship between the packing factor at the stagnation point in the model and the measured values for ρ_o could be obtained. Unfortunately, only two of the five density experiments from the FROST tunnel cover these conditions. Further experiments performed under these conditions are required to observe if there is a relation between ρ_o and $-rv_o/T_o$.

Table 5.5 Average values for absolute stagnation point density (ρ_o) as calculated by Makkonen (1984) and by Macklin (1962) for a rotating cylinder. The calculations pertained to flow conditions from (a) FROST tunnel and (b) Prodi (1985).

CASE	$(-rv_o/T_s)$ $\frac{\mu m \cdot ms^{-1}}{°C}$	ρ_o (Makkonen) $\frac{kg}{m^3}$	ρ_o (Macklin) $\frac{kg}{m^3}$	ρ_o (X-ray) $\mp 20 \frac{kg}{m^3}$	packing factor at stagnation point
1	10.8	723	734	909	0.38
2	6.9	677	534	853	0.38
3	4.4	617	429	785	0.37
4	8.1	696	904	872	0.40
5	22.0	800	848	917	0.40

(a)

TEST	$(-rv_o/T_s)$ $\frac{\mu m \cdot ms^{-1}}{°C}$	ρ_o (Makkonen) $\frac{kg}{m^3}$	ρ_o (Macklin) $\frac{kg}{m^3}$	ρ_o (X-ray) $\frac{kg}{m^3}$	packing factor at stagnation point
1	3.2	572	266	620	0.39
2	3.4	580	279	695	0.39
3	4.1	608	321	917	0.38

(b)

6. CONCLUSIONS

6.1 Rime Feather Growth Angles

Between the two stochastic models, the curved trajectory model predictions of growth angles were in closer agreement with experiment. This was because the growth directions depend directly on the path of the droplet trajectories. The curved trajectory model predictions provided better agreement with actual results when K was greater than about 3.5 because, in these flow conditions, droplets of all size in the real droplet spectrum tend to follow straight trajectories and contribute to the growth of rime feathers. One should note, however, the agreement is expected to be poor whenever $(-rv_o/T_{su})$ at the accretion edges exceeds a certain value. Such conditions promote droplet deformation and rime feathers may not develop on the actual ice accretion.

With K less than 3.5, the problem of using a monodisperse droplet spectrum in the models exists because, for these cases, large droplets from the spectrum contribute to the icing processes near the edges of the actual accretion. Thus, for small K values, a droplet diameter, D_d, greater than the spectrum MVD should be applied in the models.

6.2 Local Ice Densities

The basic difference between the two models' predictions is that the straightline model produces a uniform density near the stagnation point, while the curved trajectory model does not. The simple model provides good agreement with experiment in flow conditions where

$(-rv_o/T_o)$ is greater than about six. The curve fit in Figure 5.5 shows that the empirical correlation for density is accurate when D_c/D_d is greater than 508.

In flow conditions where $(-rv_o/T_o)$ is less than six, the curved trajectory model produced more accurate predictions for density.

6.3 Applications

The curved trajectory model may prove useful in predicting ice accretion shapes in models such as that of Lozowski et al. In dry icing conditions, and when K is greater than 3.5, but $(-rv_r/T_{su})$ at the accretion edges is low, the model provides accurate predictions for the feather growth angles. The model, however, is limited for use in a small time interval at the beginning of the accretion process, because the droplet trajectories vary with the change of the ice profile.

As for the density variation along the surface of the cylinder, both models could provide accurate density variations for the model of Lozowski et al. When $(-rv_o/T_o)$ is greater than about six and D_c/D_d is greater than 508, the density correlation from the straightline model could be applied. When $(-rv_o/T_o)$ is less than six, the curved trajectory model provides a better correlation for density.

REFERENCES

Beard, K.V., and H.R. Pruppacher, 1969: A determination of the terminal velocity and of small water drops by means of a wind tunnel. J. Atmos. Sci., 26, 1066-1077.

Bain, M., and J.F. Gayet, 1983: Contribution to the modelling of the ice accretion process: ice density variation with the impacted surface angle. Proc., First Int. Workshop on Atmospheric Icing of Structures. CRREL, Hanover, NH, 13-20.

Dolezell, A.C., R.J. Cunningham, and R.E. Katz, 1946: Bull. Amer. Soc., 27, p. 261.

Finstad, K., 1986: Numerical and experimental studies of rime ice accretion on cylinders and airfoils. Unpublished Ph.D. thesis, University of Alberta, 229pp.

Fraser, D., C.K. Rush, and D. Baxter, 1952: Thermodynamic limitations of ice accretion instruments. Lab. Rep. LR-32, N.A.E. Canada.

Langmuir, I., and K.B. Blodgett, 1946: A mathematical investigation of water droplet trajectories. Collected Works of I. Langmuir. Pergamon Press, 10, 348-393.

Lozowski, E.P., and R. d'Amours, 1980: A time-dependent numerical model for spherically symmetric hailstone growth thermodynamics under constant ambient conditions. J. Atmos. Sci., 37, 1808-1820.

Lozowski, E.P., and M.M. Oleskiw, 1981: Computer simulation of airfoil icing without runback. Pap. AIAA-81-0404, Amer. Inst. of Aeronaut. and Astronaut. 8pp.

Lozowski, E.P., J.R. Stallabrass, and P.F. Hearty, 1983a: The icing of an unheated, nonrotating cylinder. Part 1: A simulation model. J. Climate Appl. Met., 22, 2053-2062.

Ludlam, F.H., 1951: The heat economy of a rimed cylinder. Quart. J. R. Met. Soc., 77, p. 663.

Macklin, W.C., 1962: The density and structure of ice formed by accretion. Quart. J. Roy. Meteor. Soc., 88, 30-50.

Makkonen, L.J., and J.R. Stallabrass, 1984: Ice accretion on cylinders and wires. National Research Council of Canada Report TR-LT-005.

McComber, P., 1982: Numerical simulation of ice accretion on cables. Proc. First Int. Workshop on Atmospheric Icing of Structures, CRREL, Hanover, NH, 51-58.

Messinger, B.L., 1953: Equilibrium temperature of an unheated icing surface as a function of airspeed. J. Aeronaut. Sci., 20, 29-42.

Prodi, F., 1970: Measurements of local density in artificial and natural hailstones. J. Appl. Met., 9, 903-910.

Prodi, F., L. Levi, and V. Levizzani, 1985: Ice accretions on fixed cylinders. Submitted to Quart. J. Roy. Meteor. Soc.

Schlichting, H., 1979: Boundary-Layer Theory. McGraw-Hill Book Company, seventh edition.

Stallabrass, J.R., 1980: Trawler icing: A compilation of work done at NRC. National Research Council of Canada Report DM-EMD-56, 113pp.

Streeter, V.L., and E.B. Wylie, 1979: Fluid Mechanics. McGraw-Hill Book Company, seventh edition.

Tribus, M., G.B.W. Young, and L.M.K. Boelter, 1948: Limitations and mathematical basis for predicting aircraft icing characteristics from scale-model studies. Am. Soc. Mech. Engrs. - Trans., 70, 977-982.

Van Vlack, L.H., 1980: Elements of materials science and engineering. Fourth edition. p.76.

APPENDIX 1

PROGRAM FOR STRAIGHTLINE TRAJECTORY MODEL

```
C
C SET FLOW PARAMETERS DC AND DD BEFORE EXECUTING
C
 DIMENSION A(20000),B(20000),C(20000),R1(20000),X(50000),Y(50000)
 INTEGER COUNT,DROPLT,DROPS,K(110)
 DOUBLE PRECISION DSEED
C
 CALL PLOTS
 CALL METRIC(0)
 CALL FACTOR(5.0/D)
 DIST = 0.0
 D = 100.0
 DC = 0.0254
 DD = 0.0000254
 RATIO = DC/DD
 R = D/RATIO
 NDROP = 20000
 NSECT = 110
 DSEED = 13957.D0
 CALL GGUBS(DSEED,NDROP,RI)
 CALL CIRCLE(D,0.0,0.0,90.0,D,D,0.0)
 CALL CIREP1(10.0)
 CALL PLOT(0.0,0.0,2)
 CALL PLOT(D,0.0,2)
 DO 20 M = 1,NSECT
20 K(M) = M
 COUNT = 1
 DO 77 J = 1,50000
 X(J) = 0.0
77 Y(J) = 0.0
 Z = 0.0
 DO 50 DROPLT = 1,NDROP
 YR = (D*1.1)*RI(DROPLT)
 IF(YR.GT.(D+R)) XH = -1.0
 IF(YR.LE.(D+R)) XH = SQRT((D+R)**2 -(YR**2))
 M = YR+1.0
 IF(M.EQ.111) M = D*1.1
 L = K(M)
  DO 100 N = M,L,NSECT
  XP = X(N)
  YP = Y(N)
  IF(N.EQ.L) GOTO 99
  IF(ABS(YP-YR).GT.(2*R)) GOTO 99
  Z = SQRT((2*R)**2 - (YP-YR)**2) + XP
99  IF(Z.GT.XH) XH = Z
  Z = 0.0
100  CONTINUE
 IF(XH.EQ.0) GOTO 50
 CALL CIRCL2(XH,YH,0.0,360.0,R)
 X(L) = XH
```

```
      Y(L) = YR
      K(M) = L+NSECT
      IF(M.GE.NSECT .OR. YR.LT.(M - 2*R)) GOTO 200
      L = K(M+1)
      X(L) = XH
      Y(L) = YR
      K(M+1) = L+NSECT
  200 CONTINUE
      IF(M.LE.1 .OR. YR.GT.((M-1) + 2*R)) GOTO 300
      L = K(M-1)
      X(L) = XH
      Y(L) = YR
      K(M-1) = L+NSECT
  300 CONTINUE
      COUNT = COUNT+1
   50 CONTINUE
      CALL PLOT(0.0,0.0,999)
      DROPS = COUNT-1
      WRITE(6,1) DROPS
    1 FORMAT(1X,'#DROPLETS IN RIME STRUCTURE=',I5)
      STOP
      END
```

APPENDIX 2

DROPLET TRAJECTORY CALCULATIONS

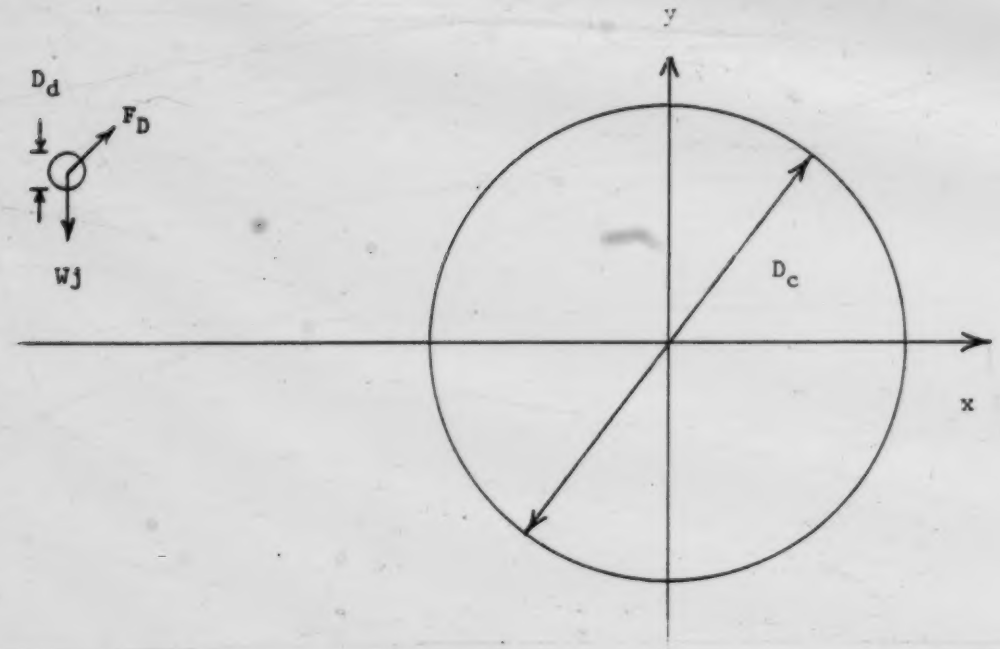

The equation of motion for the droplet in an airstream is,

$$\Sigma F = ma \tag{A.2.1}$$

and the forces acting on the droplet are the gravitational and drag forces. So,

$$m_d \frac{dv_d}{dt} = -Wj + F_D \tag{A.2.2}$$

$$m_d \frac{dv_d}{dt} = -Wj + \frac{1}{2}\rho_a A_d C_D \cdot |v_a - v_d|^2 \cdot \lambda \tag{A.2.3}$$

The directional vector λ can be written as,

$$\lambda = \frac{v_a - v_d}{|v_a - v_d|} \tag{A.2.4}$$

Substituting (A.2.4) into (A.2.3),

$$m_d \frac{dv_d}{dt} = -Wj + \frac{1}{2}\rho_a A_d C_D |v_a - v_d| (v_a - v_d) \qquad (A.2.5)$$

Introducing the following nondimensional variables,

$$v^* = \frac{v}{U_\infty} \qquad (A.2.6)$$

$$x^* = \frac{x}{D_c} \qquad (A.2.7)$$

$$t^* = \frac{tU_\infty}{D_c} \qquad (A.2.8)$$

and substituting,

$$m_d = \frac{1}{6}\pi D_d^3 \rho_w \qquad (A.2.9)$$

and

$$A_d = \frac{\pi D_d^2}{4} \qquad (A.2.9)$$

into (A.2.5), one obtains

$$\frac{1}{6}\pi D_d^3 \rho_w \frac{U_\infty^2}{D_c} \frac{dv_d^*}{dt^*} = -\frac{1}{6}\pi D_d^3 \rho_w gj + \frac{1}{2}\rho_a \frac{\pi D_d^2}{4} C_D U_\infty^2 |v_a - v_d|(v_a - v_d) \qquad (A.2.10)$$

which reduces to,

$$K\frac{dv_d^*}{dt^*} = -Hj + \frac{ReC_D}{24}(v_a^* - v_d^*) \qquad (A.2.11)$$

where,

$$K = \frac{D_d^2 \rho_w U_\infty}{18 D_c \eta_a}, \quad H = \frac{D_d^2 \rho_w g}{18 U_\infty \eta_a}, \quad \text{and } Re = \frac{\rho_a D_d U_\infty |v_a^* - v_d^*|}{\eta_a}$$

Rewriting (A.2.11) in x and y components and dropping the * notation,

$$K\frac{dv_{d_x}}{dt} = \frac{ReC_D}{24}(v_{a_x} - v_{d_x}) \tag{A.2.12}$$

$$\frac{dx_d}{dt} = v_{d_x} \tag{A.2.13}$$

$$K\frac{dv_{d_y}}{dt} = \frac{ReC_D}{24}(v_{a_y} - v_{d_y}) \tag{A.2.14}$$

$$\frac{dy_d}{dt} = v_{d_y} \tag{A.2.15}$$

All variables are nondimensional. The above equations are first order differential equations and by letting $v_{d_x} = u$ and $v_{d_y} = v$, one would observe the equations are in the form,

$$\frac{du}{dt} = f(x,y,u;v) \tag{A.2.16}$$

$$\frac{dx}{dt} = u \tag{A.2.17}$$

$$\frac{dv}{dt} = g(x,y,u,v) \tag{A.2.18}$$

$$\frac{dy}{dt} = v \tag{A.2.19}$$

which may be solved with a 4-th order Runge-Kutta numerical technique by letting,

$$u_{i+1} = u_i + \frac{1}{6}(k_1 + 2k_2 + 2k_3 + k_4)$$

$$x_{i+1} = x_i + \frac{1}{6}(l_1 + 2l_2 + 2l_3 + l_4)$$

$$v_{i+1} = v_i + \frac{1}{6}(m_1 + 2m_2 + 2m_3 + m_4)$$

$$y_{i+1} = y_i + \frac{1}{6}(n_1 + 2n_2 + 2n_3 + n_4)$$

where,

$$k_1 = hf(x_i, y_i, u_i, v_i)$$

$$k_2 = hf(x_i + \frac{l_1}{2}, y_i + \frac{n_1}{2}, u_i + \frac{k_1}{2}, v_i + \frac{m_1}{2})$$

$$k_3 = hf(x_i + \frac{l_2}{2}, y_i + \frac{n_2}{2}, u_i + \frac{k_2}{2}, v_i + \frac{m_2}{2})$$

$$k_4 = hf(x_i + l_3, y_i + n_3, u_i + k_3, v_i + m_3)$$

$$l_1 = hu_i$$

$$l_2 = h(u_i + \frac{k_1}{2})$$

$$l_3 = h(u_i + \frac{k_2}{2})$$

$$l_4 = h(u_i + k_3)$$

$$m_1 = hg(x_i, y_i, u_i, v_i)$$

$$m_2 = hg(x_i + \frac{l_1}{2}, y_i + \frac{n_1}{2}, u_i + \frac{k_1}{2}, v_i + \frac{m_1}{2})$$

$$m_3 = hg(x_i + \frac{l_2}{2}, y_i + \frac{n_2}{2}, u_i + \frac{k_2}{2}, v_i + \frac{m_2}{2})$$

$$m_4 = hg(x_i + l_3, y_i + n_3, u_i + k_3, v_i + m_3)$$

and

$$n_1 = hv_i$$

$$n_2 = h(v_i + \frac{m_1}{2})$$

$$n_3 = h(v_i + \frac{m_2}{2})$$

$$n_4 = h(v_i + m_3)$$

where the nondimensional time step is h. From Beard and Pruppacher (1969),

$$\frac{ReC_D}{24} = 1 + 0.102Re^{0.955} \qquad 0.2 < Re < 2 \qquad (A.2.20)$$

$$\frac{ReC_D}{24} = 1 + 0.115Re^{0.802} \qquad 2 < Re < 21 \qquad (A.2.21)$$

$$\frac{ReC_D}{24} = 1 + 0.089Re^{0.632} \qquad 21 < Re < 200 \qquad (A.2.22)$$

$$\frac{ReC_D}{24} = 1 + 0.197Re^{0.63} + 0.00026Re^{1.38} \qquad 200 < Re \qquad (A.2.23)$$

APPENDIX 3

POTENTIAL FLOW PAST A CYLINDER

For steady-state incompressible flow around a right circular cylinder in an x-y plane, the stream function is given by,

$$\Psi = U_\infty y - \frac{U_\infty y D_c^2}{4(x^2 + y^2)}$$

The velocity in the x-direction is,

$$u_x = \frac{\partial \Psi}{\partial y} = U_\infty - \frac{U_\infty D_c^2}{4(x^2 + y^2)} + \frac{2y^2 U_\infty D_c^2}{4(x^2 + y^2)^2}$$

$$u_x = U_\infty + \frac{U_\infty D_c^2 (y^2 - x^2)}{4(x^2 + y^2)^2}$$

or in nondimensional form,

$$u_x^* = 1 + \frac{y^{*2} - x^{*2}}{4(x^{*2} + y^{*2})^2} \qquad \text{(A.3.1)}$$

The velocity in the y-direction is,

$$u_y = - \frac{\partial \Psi}{\partial x} = - \frac{U_\infty x y D_c^2}{2(x^2 + y^2)^2}$$

or in nondimensional form,

$$u_y^* = - \frac{x^* y^*}{2(x^{*2} + y^{*2})^2} \qquad \text{(A.3.2)}$$

APPENDIX 4

PROGRAM FOR THE DETERMINATION OF Y_1

```
C
C TRY VARIOUS VALUES OF YS FOR A PARTICULAR SET OF FLOW CONDITIONS
C (DC,DD,VA,TA) UNTIL YS - Y1 IS OBTAINED.  PROGRAM IS EXECUTED
C WITH,
C
C
C       * * * * * * * * * * * * * * * * * * * * * * * * * * * *
C       *                                                     *
C       *              #R *FORTG SCARDS=file                  *
C       *              #R -LOAD#                              *
C       *                                                     *
C       * * * * * * * * * * * * * * * * * * * * * * * * * * * *
C
C
      DOUBLE PRECISION FUNCTION CDRE(A,B,C,D)
      DD = 36.9D-6
      VA = 10.0D0
      TA = -15.0D0
      ADENS = 1.0D5/(287.0D0*(TA + 273.0D0))
      AVISC = 0.2033D-5*(TA + 273.0D0)**1.5/(TA + 273.0D0 +232.7D0)
      VAAY = -0.5*A*B/(A**2 + B**2)**2
      VAAX = 1.0 + 0.25*(B**2 - A**2)/(A**2 + B**2)**2
      RE = ADENS*DD*VA*((VAAX - C)**2 + (VAAY - D)**2)**0.5D0/AVISC
      IF(RE.LT.0.2) CDRE = 1.0D0
      IF(0.2.LE.RE.AND.RE.LT.2.0) CDRE = 1.0D0 + 1.02D-1*RE**9.55D-1
      IF(2.0.LE.RE.AND.RE.LT.21.0) CDRE = 1.0D0 + 1.15D-1*RE**8.02D-1
      IF(21.0.LE.RE.AND.RE.LT.200.0) CDRE = 1.0D0 + 8.9D-2*RE**6.32D-1
      IF(RE.GT.200.0) CDRE=1.0D0 + 1.97D-1*RE**6.3D-1 + 2.6D-4*RE**1.38D0
      RETURN
      END
C
      INTEGER SUM
      REAL K
      DOUBLE PRECISION ADENS,ADX,ADY,AVISC,CDRE,DC,DD,H,K1,K2,K3,K4
      DOUBLE PRECISION L1,L2,L3,L4,M1,M2,M3,M4,N1,N2,N3,N4,R,RATIO,TA
      DOUBLE PRECISION VA,VAX,VAXX,VAY,VAYY,WDENS,X,XS,Y,YS
C
      VAY(A,B) = -0.5*A*B/(A**2 + B**2)**2
      VAX(A,B) = 1.0 + 0.25*(B**2 - A**2)/(A**2 + B**2)**2
      ADX(A,B,C,D) = CDRE(A,B,C,D)*(VAX(A,B) - C)/K
      ADY(A,B,C,D) = CDRE(A,B,C,D)*(VAY(A,B) - D)/K
C
      DD = 36.9D-6
      DC = 2.54D-2
      VA = 10.0D0
      TA = -15.0D0
      XS = -10.0D0
      YS = 0.1877
      H= 0.0050D0
      WDENS = 1000.0D0
      ADENS = 1.0D5/(287.0D0*(TA+273.0D0))
```

```
      AVISC = 0.2033D-5*(TA + 273.0D0)**1.5/(TA + 273.0D0 + 232.7D0)
      K = (DD**2)*WDENS*VA/(18.0*DC*AVISC)
      DIST = (DC/2.0 + DD/2.0)/DC
      RATIO = DC/DD
      R = 0.5D0/RATIO
      WRITE(6,109)
  109 FORMAT('0',6X,'X',9X,'Y',7X,'VDX',7X,'VDY',7X,'VAXX',7X,'VAYY',
     Z5X,'TIME STEP')
     C
      X = XS
      Y = YS
      VDX = 0.0D0
      VDY = 0.0D0
      I = 1
  113 K1 = H*ADX(X,Y,VDX,VDY)
      L1 = H*VDX
      M1 = H*ADY(X,Y,VDX,VDY)
      N1 = H*VDY
      K2 = H*ADX(X + L1/2.0,Y + N1/2.0,VDX + K1/2.0,VDY + M1/2.0)
      L2 = H*(VDX + K1/2.0)
      M2 = H*ADY(X + L1/2.0,Y + N1/2.0,VDX + K1/2.0,VDY + M1/2.0)
      N2 = H*(VDY + M1/2.0)
      K3 = H*ADX(X + L2/2.0,Y + N2/2.0,VDX + K2/2.0,VDY + M2/2.0)
      L3 = H*(VDX + K2/2.0)
      M3 = H*ADY(X + L2/2.0,Y + N2/2.0,VDX + K2/2.0,VDY + M2/2.0)
      N3 = H*(VDY + M2/2.0)
      K4 = H*ADX(X + L3,Y + N3,VDX + K3,VDY + M3)
      L4 = H*(VDX + K3)
      M4 = H*ADY(X + L3,Y + N3,VDX + K3,VDY + M3)
      N4 = H*(VDY + M3)
      X = X + (L1 + 2.0*L2 + 2.0*L3 + L4)/6.0D0
      Y = Y + (N1 + 2.0*N2 + 2.0*N3 + N4)/6.0D0
      VDX = VDX + (K1 + 2.0*K2 + 2.0*K3 + K4)/6.0D0
      VDY = VDY + (M1 + 2.0*M2 + 2.0*M3 + M4)/6.0D0
      VAXX = VAX(X,Y)
      VAYY = VAY(X,Y)
      IF((I/1000)*1000.EQ.I)WRITE(6,110)X,Y,VDX,VDY,VAXX,VAYY,I
  110 FORMAT('0',6F10.5,I10)
      IF(X**2 + Y**2.LE.DIST**2.OR.X.GE.0.0) GOTO 112
      XO = X
      YO = Y
      I = I + 1
      GOTO 113
  112 IF(X.GE.0.0) GOTO 120
      WRITE(6,110)X,Y,VDX,VDY,VAXX,VAYY,I
  120 CONTINUE
      STOP
      END
```

APPENDIX 5

PROGRAM FOR CURVED TRAJECTORY MODEL

```
C
C INSERT APPROPRIATE SET OF FLOW CONDITIONS (DC,DD,VA,TA) AND YMAX
C (-YS FROM APPENDIX 4) AND EXECUTE MODEL WITH THE FOLLOWING SET OF
C COMMAND.  THE PLOT WILL BE PRODUCED ON CALCOMPQ PAPER.
C
C
C * * * * * * * * * * * * * * * * * * * * * * * * * * * * * * * * * * *
C *                                                                     *
C *       #R *FORTG SCARDS-file T=400                                   *
C *       #CR -PLOT SIZE=3000P                                          *
C *       #EMPTY -PLOT OK                                               *
C *       #R -LOAD#+*APPLOT+*PLOTLIB+*IMSLLIB 9=-PLOT T=400             *
C *       #TRUNC -PLOT                                                  *
C *       #R *CALCOMPQ PAR-FILE=-PLOT PEN=3BLK                          *
C *       #SOURCE PREVIOUS                                              *
C *                                                                     *
C * * * * * * * * * * * * * * * * * * * * * * * * * * * * * * * * * * *
C
C
C ALL POSITIONS AND VELOCITIES ARE NORMALIZED
C
 DOUBLE PRECISION FUNCTION CDRE(A,B,C,D,E,F,VD)
 VAAY = -0.5*A*B/(A**2 + B**2)**2
 VAAX = 1.0 + 0.25*(B**2 - A**2)/(A**2 + B**2)**2
 RE = E*VD*((VAAX - C)**2 + (VAAY - D)**2)**0.5D0/F
 IF(RE.LT.0.2) CDRE = 1.0D0
 IF(0.2.LE.RE.AND.RE.LT.2.0) CDRE = 1.0D0 + 1.02D-1*RE**9.55D-1
 IF(2.0.LE.RE.AND.RE.LT.21.0) CDRE = 1.0D0 + 1.15D-1*RE**8.02D-1
 IF(21.0.LE.RE.AND.RE.LT.200.0) CDRE = 1.0D0 + 8.9D-2*RE**6.32D-1
 IF(RE.GT.200.0) CDRE=1.0D0 + 1.97D-1*RE**6.3D-1 + 2.6D-4*RE**1.38D0
 RETURN
 END
C
C SPECIFICATION OF VARIABLE TYPES
C
 INTEGER COUNT,DROPLT,DROPS,IC,IER,KCOUNT,M,MM(90),NX
 REAL BPAR(4),CS(2999,3),C2(2999,3),C3(2999,3),C4(2999,3),C5(2999,3)
 REAL DENSTY(90),DS(5),DYC(20000),E(3000),E1(3000),E2(3000),E3(3000)
 REAL E4(3000),E5(3000),F(3000),F1(3000),F2(3000),F3(3000),F4(3000)
 REAL F5(3000),K(5),KK,S(2),RI(10000),SC(6),U(2),UU(10000),V(10000)
 REAL W(10000),XX(20000),YBC(20000),YBL(20000),YTC(200000,YTL(20000)
 DOUBLE PRECISION ADX,ADY,CDRE,DC,DD,DSEED,H,K1,K2,K3,K4,L1,L2,L3,L4
 DOUBLE PRECISION M1,M2,M3,M4,N1,N2,N3,N4,R,RATIO,TA,VA,VAX,VAXX
 DOUBLE PRECISION VAY,VAYY,WDENS,X,XS,Y,YS
C
C CALCULATION OF COMPONENTS OF AIR VELOCITY AND DROPLET ACCELERATION
C
 VAX(A,B) = 1.0 + 0.25*(B**2 - A**2)/(A**2 + B**2)**2
 VAY(A,B) = -0.5*A*B/(A**2 + B**2)**2
```

```
      ADX(A,B,C,D) = CDRE(A,B,C,D,ADENS,AVISC,VD)*(VAX(A,B) - C)/KK
      ADY(A,B,C,D) = CDRE(A,B,C,D,ADENS,AVISC,VD)*(VAY(A,B) - D)/KK
C
C FLOW CONDITIONS
C
      DD = 36.9D-6
      DC = 2.54D-2
      VA = 10.0D0
      TA = -15.0D0
      VD = VA*DD
      DIST = (DC/2.0 + DD/2.0)/DC
      RATIO = DC/DD
      R = 0.5D0/RATIO
      WDENS = 1000D0
      ADENS = 1.0D5/(287.0D0*(TA + 273.0D0))
      AVISC = 0.2033D-5*(TA + 273.0D0)**1.5/(TA + 273.0D0 +232.7D0)
      KK = (DD**2)*WDENS*VA/(18.0*DC*AVISC)
C
C CALCULATION OF THE SIX TRAJECTORIES THAT MAKE UP THE BOUNDARIES
C OF THE FIVE BANDS LOCATED UPSTREAM FROM THE CYLINDER.  INITIAL
C POSITION (XS) AND VELOCITY (VDX,VDY) OF THE DROPLET MUST BE
C SPECIFIED FIRST.  THEN, THE POINTS THAT MAKE UP THE TRAJECTORIES
C ARE CALCULATED WITH A 4-TH ORDER RUNGE-KUTTA TECHNIQUE.
C
      H = 0.005D0
      XS = -10.0D0
      VDX = 0.0D0
      VDY = 0.0D0
      J = 1
      SC(J) = 0.0
   60 I = 1
      KO = 1
      KX = 2
      X = XS
      Y = 0.1*J
      E1(1) = X
      F1(1) = Y
  113 K1 = H*ADX(X,Y,VDX,VDY)
      L1 = H*VDX
      M1 = H*ADY(X,Y,VDX,VDY)
      N1 = H*VDY
      K2 = H*ADX(X+L1/2.0,Y+N1/2.0,VDX+K1/2.0,VDY+M1/2.0)
      L2 = H*(VDX+K1/2.0)
      M2 = H*ADY(X+L1/2.0,Y+N1/2.0,VDX+K1/2.0,VDY+M1/2.0)
      N2 = H*(VDY+M1/2.0)
      K3 = H*ADX(X+L2/2.0,Y+N2/2.0,VDX+K2/2.0,VDY+M2/2.0)
      L3 = H*(VDX+K2/2.0)
      M3 = H*ADY(X+L2/2.0,Y+N2/2.0,VDX+K2/2.0,VDY+M2/2.0)
      N3 = H*(VDY+M2/2.0)
      K4 = H*ADX(X+L3,Y+N3,VDX+K3,VDY+M3)
      L4 = H*(VDX+K3)
      M4 = H*ADY(X+L3,Y+N3,VDX+K3,VDY+M3)
      N4 = H*(VDY+M3)
      X = X + (L1+2.0*L2+2.0*L3+L4)/6.0D0
```

```
      Y = Y + (N1+2.0*N2+2.0*N3+N4)/6.0D0
      VDX = VDX + (K1+2.0*K2+2.0*K3+K4)/6.0D0
      VDY = VDY + (M1+2.0*M2+2.0*M3+M4)/6.0D0
      VAXX = VAX(X,Y)
      VAYY = VAY(X,Y)
      IF(X.GE.0.0) GOTO 112
      IF(X**2+Y**2.GT.DIST**2.OR.KO.EQ.2) GOTO 114
      CALL CONTAK(X,Y,XO,YO,XR,YR,DIST)
      KO = 2
  114 XO = X
      YO = Y
      I = I+1
      E1(I) = X
      F1(I) = Y
      IF(I.NE.3000) GOTO 113
     C
     C THE BOUNDARY POINTS ARE FITTED WITH A CUBIC SPLINE USING
     C THE IMSLLIB ROUTINE ICSICU.
     C
      IC = 2999
      NX = 3000
      FNX = SQRT(VDX**2+VDY**2)
      BPAR(1) = 1.0
      BPAR(2) = 6.0/(E1(2)-E1(1))*((F1(2)-F1(1))/(E1(2)-E1(1))-0.0)
      BPAR(3) = 1.0
      BPAR(4) = 6.0/(E1(NX)-E1(NX-1))*(FNX-(F1(NX)-F1(NX-1))/(E1(NX)-
     ZE1(NX-1)))
      IF(J.EQ.1) GOTO 10
      IF(J.EQ.2) GOTO 20
      IF(J.EQ.3) GOTO 30
      IF(J.EQ.4) GOTO 40
      IF(J.EQ.5) GOTO 50
   10 DO 11 I=1,NX
      E(I) = E1(I)
   11 F(I) = F1(I)
      CALL ICSICU(E,F,NX,BPAR,CS,IC,IER)
      J = 2
      GOTO 60
   20 DO 21 I=1.NX
      E2(I) = E1(I)
   21 F2(I) = F1(I)
      CALL ICSICU(E2,F2,NX,BPAR,C2,IC,IER)
      J = 3
      GOTO 60
   30 DO 31 I=1,NX
      E3(I) = E1(I)
   31 F3(I) = F1(I)
      CALL ICSICU(E3,F3,NX,BPAR,C3,IC,IER)
      J = 4
      GOTO 60
   40 DO 41 I=1,NX
      E4(I) = E1(I)
   41 F4(I) = F1(I)
      CALL ICSICU(E4,F4,NX,BPAR,C4,IC,IER)
```

```
      J = 5
      GOTO 60
   50 DO 51 I=1,NX
      E5(I) = E1(I)
   51 F5(I) = F1(I)
      CALL ICSICU(E5,F5,NX,BPAR,C5,IC,IER)
     C
     C PLOT A QUARTER CYLINDER WITH RADIUS OF 0.5
     C
      COMMON XX,YY,U,V
      CALL PLOTS
      PI = 3.14159
      FD = 0.0
      CALL METRIC(0)
      CALL FACTOR(10.0)
      CALL CIRCLE(0.5,0.0,0.0,90.0,0.5,0.5,0.0)
      CALL CIREP1(10.0)
      CALL PLOT(0.0,0.0,2)
      CALL PLOT(0.5,0.0,2)
     C
     C SPECIFY NUMBER OF DROPLETS TO BE INTRODUCED INTO THE FLOW
     C USE RANDOM NUMBER GENERATOR IMSLLIB ROUTINE GGUBS TO DETERMINE
     C YR POSITION OF DROPLET.
     C
      NSECT = 5
      NDROP = 10000
      DSEED = 13957.D0
      CALL GGUBS(DSEED,BDROP,RI)
      DO 70 M=1,NSECT
   70 K(M) = M
      COUNT = 1
      DO 77 J=1,20000
      XX(J) = 0.0
      YY(J) = 0.0
      DYC(J) = 0.0
      YTC(J) = 0.0
      YTL(J) = 0.0
      YBC(J) = 0.0
      YBL(J) = 0.0
   77 CONTINUE
      CALL SPACE
      ZX = 0.0
      ZY = 0.0
      YMAX = 0.3014
     C
     C YMAX = YR FOR LIMITING TRAJECTORY
     C
      DO 80 DROPLT=1,NDROP
      YR = 5.5*RI(DROPLT)
      M = YR + 1.0
     C
     C DETERMINE WHICH BAND (M=1,2,...5) DROPLET WILL ENTER.  IF M > 5,
     C DROPLET IS SHED INTO THE AIRSTREAM, OTHERWISE DROPLET STICKS TO
     C STRUCTURE AND CALCULATION OF ITS POSITION (XD,YD) IN THE
```

```
C ACCRETION IS PERFORMED.
C
 IF(M.GT.5) GOTO 80
 IF(YR.LT.1.0) FR = YR
 IF(YR.GE.1.0) MB = YR
 IF(YR.GE.1.0) FR = YR - MB
 YR = YR/10.0
 XD = -0.0001
 IF(YR.GT.YMAX) XD = 1.0
 L = K(M)
 DO 100 N=M,L,NSECT
 XP = XX(N)
 YP = YY(N)
 IF(N.EQ.L) GOTO 99
 YT = YTC(N)-(1-FR)*DYC(N)
 IF(ABS(YP-YT).GT.(2*R)) GOTO 99
 SLOPEU = (YTC(N)-YTL(N))/(20*R)
 SLOPEL = (YBC(N)-YBL(N))/(20*R)
 SLOPE = SLOPEL+FR*(SLOPEU-SLOPEL)
 YINT = YT-SLOPE*XP
 A = SLOPE**2 +1
 B = 2.0*(YINT- YP)*SLOPE-2.0*XP
 CC = XP**2+(YINT-YP)**2-(2*R)**2
 GG = B**2-4.0*A*CC
 IF(GG.EQ.0.0) GOTO 97
 GG = -GG
 97 X1 = (-B+SQRT(GG))/(2.0*A)
 X2 = (-B-SQRT(GG))/(2.0*A)
 IF(X1.LE.X2) ZX=X1
 IF(X2.LE.X1) ZX=X2
 ZY = SLOPE*ZX+YINT
 KX = 1
 99 IF(ZX.GE.XD) GOTO 105
 XD = ZX
 YD = ZY
 XOO = XX(N)
 YOO = YY(N)
105 ZX = 0.0
 ZY = 0.0
100 CONTINUE
 IF(XD.EQ.0.0) GOTO 80
 IF(KX.EQ.1.AND.XD**2+YD**2.GE.DIST**2) GOTO 101
 I = 1
 X = XS
 Y = YR
 VDX = 0.0D0
 VDY = 0.0D0
102 K1 = H*ADX(X,Y,VDX,VDY)
 L1 = H*VDX
 M1 = H*ADY(X,Y,VDX,VDY)
 N1 = H*VDY
 K2 = H*ADX(X+L1/2.0,Y+N1/2.0,VDX+K1/2.0,VDY+M1/2.0)
 L2 = H*(VDX+K1/2.0)
 M2 = H*ADY(X+L1/2.0,Y+N1/2.0,VDX+K1/2.0,VDY+M1/2.0)
```

```
      N2 = H*(VDY+M1/2.0)
      K3 = H*ADX(X+L2/2.0,Y+N2/2.0,VDX+K2/2.0,VDY+M2/2.0)
      L3 = H*(VDX+K2/2.0)
      M3 = H*ADY(X+L2/2.0,Y+N2/2.0,VDX+K2/2.0,VDY+M2/2.0)
      N3 = H*(VDY+M2/2.0)
      K4 = H*ADX(X+L3,Y+N3,VDX+K3,VDY+M3)
      L4 = H*(VDX+K3)
      M4 = H*ADY(X+L3,Y+N3,VDX+K3,VDY+M3)
      N4 = H*(VDY+M3)
      X = X + (L1+2.0*L2+2.0*L3+L4)/6.0D0
      Y = Y + (N1+2.0*N2+2.0*N3+N4)/6.0D0
      VDX = VDX + (K1+2.0*K2+2.0*K3+K4)/6.0D0
      VDY = VDY + (M1+2.0*M2+2.0*M3+M4)/6.0D0
      IF(X**2+Y**2.LE.DIST**2) GOTO 61
      XO = X
      YO = Y
      I = I+1
      GOTO 102
   61 SLOPE = (Y-YO)/(X-XO)
      YINT = Y-SLOPE*X
      A = SLOPE**2+1
      B = 2.0*SLOPE*YINT
      CC = YINT**2-DIST**2
      WB1 = B**2
      WB2 = 4.0*A*CC
      WB3 = WB1-WB2
      IF(WB3.GE.0.0) GOTO 417
      WB3 = -WB3
  417 X1 = (-B+SQRT(WB3))/(2.0*A)
      X2 = (-B-SQRT(WB3))/(2.0*A)
      IF(X1.LT.0.0) XR=X1
      IF(X2.LT.0.0) XR=X2
      YH = SLOPE*XR+YINT
      XD = XR
      YD = YH
      IF(KX.EQ.2) GOTO 101
      IF((YOO-YH)**2+(XOO-XR)**2.GE.(2*R)**2) GOTO 101
      A = SLOPE**2+1.0
      B = 2.0*(YINT-YOO)*SLOPE-2.0*XOO
      CC = XOO**2+(YINT-YOO)**2-(2*R)**2
      HTS = B**2-4.0*A*CC
      IF(HTS.GE.0.0) GOTO 655
      HTS = -HTS
  655 X1 = (-B+SQRT(HTS))/(2.0*A)
      X2 = (-B-SQRT(HTS))/(2.0*A)
      IF(X1.LE.X2) XT=X1
      IF(X2.LE.X1) XT=X2
      YQ = SLOPE*XT+YINT
      XD = XT
      YD = YQ
  101 KX = 2
      XOO = 0.0
      YOO = 0.0
      CALL CIRCLE(-XD,YD,0.0,360.0,R)
```

```
C
C STORE LOCATION OF DROPLET IN THE ACCRETION AND THE CORRESPONDING
C BAND NUMBER.
C
 U(1) = XD
 U(2) = XD - 20*R
 IF(M.NE.1) GOTO 200
 CALL ICSEVU(E,F,NX,CS,IC,U,S,2,IER)
 YTCM = S(1)
 YTLM = S(2)
 DYC(L) = YTCM
 YTC(L) = YTCM
 YTL(L) = YTLM
 YBC(L) = 0.0
 YBL(L) = 0.0
 CALL ICSEVU(E2,F2,NX,C2,IC,U,S,2,IER)
 L = K(M+1)
 YTCU = S(1)
 YTLU = S(2)
 DYC(L) = YTCU-YTCM
 YTC(L) = YTCU
 YTL(L) = YTLU
 YBC(L) = YTCM
 YBL(L) = YTLM
 YTCL = 0.0
 YTLL = 0.0
200 IF(M.NE.2) GOTO 201
 CALL ICSEVU(E2,F2,NX,C2,IC,U,S,2,IER)
 YTCM = S(1)
 YTLM = S(2)
 CALL ICSEVU(E,F,NX,CS,IC,U,S,2,IER)
 YTCL = S(1)
 YTLL = S(2)
 DYC(L) = YTCM-YTCL
 YTC(L) = YTCM
 YTL(L) = YTLM
 YBC(L) = YTCL
 YBL(L) = YTLL
 L = K(M-1)
 DYC(L) = YTCL
 YTC(L) = YTCL
 YTL(L) = YTLL
 YBC(L) = 0.0
 YBL(L) = 0.0
 CALL ICSEVU(E3,F3,NX,C3,IC,U,S,2,IER)
 YTCU = S(1)
 YTLU = S(2)
 L = K(M+1)
 DYC(L) = YTCU-YTCM
 YTC(L) = YTCU
 YTL(L) = YTLU
 YBC(L) = YTCM
 YBL(L) = YTLM
201 IF(M.NE.3) GOTO 202
```

```
      CALL ICSEVU(E3,F3,NX,C3,IC,U,S,2,IER)
      YTCM = S(1)
      YTLM = S(2)
      YTC(L) = YTCM
      YTL(L) = YTLM
      CALL ICSEVU(E2,F2,NX,C2,IC,U,S,2.IER)
      YTCL = S(1)
      YTLL = S(2)
      DYC(L) = YTCM-YTCL
      YBC(L) = YTCL
      YBL(L) = YTLL
      L = K(M-1)
      YTC(L) = YTCL
      YTL(L) = YTLL
      CALL ICSEVU(E,F,NX,CS,IC,U,S,2,IER)
      DYC(L) = YTCL-S(1)
      YBC(L) = S(1)
      YBL(L) = S(2)
      CALL ICSEVU(E4,F4,NX,C4,IC,U,S,2,IER)
      YTCU = S(1)
      YTLU = S(2)
      L = K(M+1)
      DYC(L) = YTCU-YTCM
      YTC(L) = YTCU
      YTL(L) = YTLU
      YBC(L) = YTCM
      YBL(L) = YTLM
  202 IF(M.NE.4) GOTO 203
      CALL ICSEVU(E4,F4,NX,C4,IC,U,S,2,IER)
      YTCM = S(1)
      YTLM = S(2)
      YTC(L) = YTCM
      YTL(L) = YTLM
      CALL ICSEVU(E3,F3,NX,C3,IC,U,S,2,IER)
      YTCL = S(1)
      YTLL = S(2)
      DYC(L) = YTCM-YTCL
      YBC(L) = YTCL
      YBL(L) = YTLL
      CALL ICSEVU(E2,F2,NX,C2,IC,U,S,2,IER)
      L = K(M-1)
      YTC(L) = YTCL
      YTL(L) = YTLL
      DYC(L) = YTCL-S(1)
      YBC(L) = S(1)
      YBL(L) = S(2)
      CALL ICSEVU(E5,F5,NX,C5,IC,U,S,2,IER)
      YTCU = S(1)
      YTLU = S(2)
      L = K(M+1)
      YTC(L) = YTCU
      YTL(L) = YTLU
      DYC(L) = YTCU-YTCM
      YBC(L) = YTCM
```

```
      YBL(L) = YTLM
  203 IF(M.NE.5) GOTO 204
      CALL ICSEVU(E5,F5,NX,C5,IC,U,S,2,IER)
      YTCM = S(1)
      YTLM = S(2)
      YTC(L) = YTCM
      YTL(L) = YTLM
      CALL ICSEVU(E4,F4,NX,C4,IC,U,S,2,IER)
      YTCL = S(1)
      YTLL = S(2)
      DYC(L) = YTCM-YTCL
      YBC(L) = YTCL
      YBL(L) = YTLL
      L = K(M-1)
      YTC(L) = YTCL
      YTL(L) = YTLL
      CALL ICSEVU(E3,F3,NX,C3,IC,U,S,2,IER)
      DYC(L) = YTCL-S(1)
      YBC(L) = S(1)
      YBL(L) = S(2)
  204 L = K(M)
      XX(L) = XD
      YY(L) = YD
      K(M) = L + NSECT
      TG = YTCM-YD
      BG = YD-YTCL
      IF(M.GE.NSECT.OR.TG.GT.2*R) GOTO 250
      L = K(M+1)
      XX(L) = XD
      YY(L) = YD
      K(M+1) = L+NSECT
  250 CONTINUE
      IF(M.LE.1.OR.BG.GT.2*R) GOTO 300
      L = K(M-1)
      XX(L) = XD
      YY(L) = YD
      K(M-1) = L + NSECT
  300 CONTINUE
      UU(COUNT) = SQRT(XD**2+YD**2)
      V(COUNT) = ATAN(YD/(-XD))*180.0/PI
      IF(UU(COUNT).GT.FD) FD=UU(COUNT)
      COUNT = COUNT+1
   80 CONTINUE
      CALL PLOT(0.0,0.0,999)
      DROPS = COUNT-1
      WRITE(6,1) DROPS
    1 FORMAT(1X,'#DROPLETS IN RIME STRUCTURE=',I5)
     C
     C DENSITY CALCULATION AT 5° SECTORS FROM STAGNATION POINT
     C
      NSECT = 18
      DO 575 ITHICK=1,3
      IF(ITHICK.EQ.1) SECTHK=8.0
      IF(ITHICK.EQ.2) SECTHK=4.0
```

```
      IF(ITHICK.EQ.3) SECTHK=2.0
      DOUT = 0.5+(FD-0.5)/SECTHK
      SAREA = (DOUT**2-0.5**2)*PI/72.0
      DAREA = PI*R**2
      KCOUNT = 1
      DO 25 KS=1,DROPS
      IF(UU(KS).GT.DOUT) GOTO 25
      W(KCOUNT) = V(KS)
      KCOUNT = KCOUNT+1
   25 CONTINUE
      DO 26 L=1,NSECT
   26 MM(L) = 0
      NC = KCOUNT-1
      DO 45 KS=1,NC
      ET = W(KS)/5.0
      N = ET+1.0
      MM(N) = MM(N)+1
      ES = N-1
      IF(ES.NE.0.0.AND.ES.EQ.W(KS)) MM(N-1)=MM(N-1)+1
   45 CONTINUE
      ISEC = SECTHK
      WRITE(6,55)ISEC
   55 FORMAT('0','SECTION',1X,'DENSITY (1/',I1,')')
      DO 65 L=1,NSECT
      DENSTY(L) = MM(L)*DAREA/SAREA
   65 CONTINUE
      DO 75 I=5,90,5
      IJ = I/5
      PACFAC = DENSTY(IJ)
      DIMLES = PACFAC/DENSTY(1)
      WRITE(6,47)I,PACFAC,DIMLES
   47 FORMAT(4X,I2,3X,F6.3,1X,F6.3)
   75 CONTINUE
      AROSTG = DENSTY(1)*890.0
      WRITE(6,5)DENSTY(1)
    5 FORMAT(1X,'PACKING FACTOR AT STAG POINT=',F5.3)
      WRITE(6,7)AROSTG
    7 FORMAT(1X,'ABSOLUTE DENSITY AT STAG POINT=',F7.2)
  575 CONTINUE
      STOP
      END
     C
      SUBROUTINE CONTAK(X,Y,XO,YO,XR,YH,DIST)
      SLOPE = (Y-YO)/(X-XO)
      YINT = Y-SLOPE*X
      A = SLOPE**2+1.0
      B = 2.0*SLOPE*YINT
      CC = YINT**2-DIST**2
      X1 = (-B+SQRT(B**2-4.0*A*CC))/(2.0*A)
      X2 = (-B-SQRT(B**2-4.0*A*CC))/(2.0*A)
      IF(X1.LT.0.0) XR=X1
      IF(X2.LT.0.0) XR=X2
      YH = SLOPE*XR+YINT
      RETURN
```

```
      END
C
      SUBROUTINE SPACE
      DIMENSION XX(20000),YY(20000),U(10000),V(10000)
      COMMON XX,YY,U,V
      RETURN
      END
```

APPENDIX 6

CALCULATION OF DROPLET CONCENTRATION

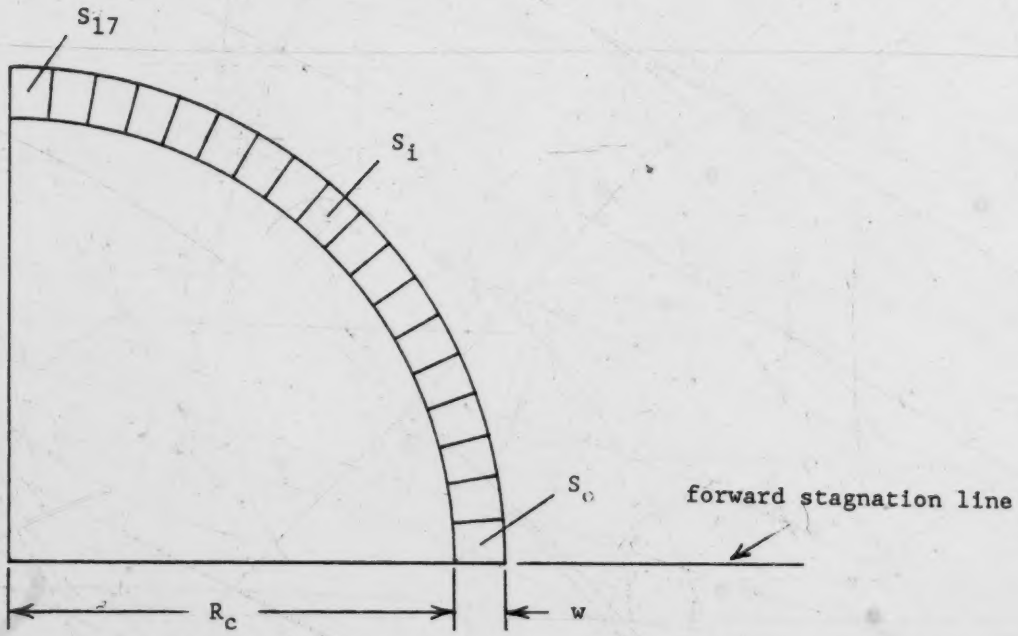

S_i - ith 5° - sector, where i - 0 at the stagnation line and increases to i - 17 at the edge of the accretion.

$C(S_i)$ - concentration of droplets in sector i

R_c - cylinder radius

R_d - droplet radius

w - width of annular region in which density calculations are made.

N_i - number of droplets in sector i

Therefore,

$$C(S_i) - \frac{\text{Area occupied by droplets in sector } S_i}{\text{Area of sector } S_i}$$

In the stochastic models, each sector occupies a constant area of,

$$S_i = \frac{\pi(R_c + w)^2 - \pi R_c^2}{72}$$

and an assumption,

$$w = \frac{\text{(distance of furthest droplet from the center of the cylinder)} - R_c}{2}$$

is made. Thus, the approximation,

$$C(S_i) = \frac{N_i * \pi R_d^2}{S_i}$$

will be used in the stochastic model to calculate droplet concentration in each sector. In fact, $C(S_i)/C(S_o)$ is calculated and will represent ρ/ρ_o in the density plots.

APPENDIX 7

CALCULATION OF K AND ϕ

$$K = \frac{2\rho_w R_d^2 U_\infty}{9\eta_a R_c}$$

$$\phi = \frac{18\rho_a^2 R_c U_\infty}{\eta_a \rho_w}$$

where,

ρ_w (kg/m^3) - water density

ρ_a (kg/m^3) - air density

U_∞ (m/s) - freestream velocity

η_a (kg/m•sec) - air viscosity

R_c (m) - cylinder radius

R_d (m) - droplet radius

All variables are in S.I. units. From L & B (1946),

$$\eta_a = 2.48 \times 10^{-7}\ T^{0.754}\ \text{kg/m•sec}$$

where T is in °K. At the flow conditions of test A from Table 3.1,

R_d = 9.1 μm

U_∞ = 10 m/s

T = 258 °K

$P_a = 10^5$ N/m^2

and therefore,

$$\eta_a = 1.632 \times 10^{-5}\ \text{kg/m•sec}$$

$$\rho_a = \frac{P_a}{RT} = \frac{10^5}{(2.87)(258)} = 1.35 \text{ kg/m}^3$$

and,

$$\rho_w \simeq 1000 \text{ kg/m}^3$$

Thus,

$$K = \frac{2(1000)(9.1 \times 10^{-6})^2(10)}{9(1.632 \times 10^{-5})(0.0254/2)} = 0.89$$

and,

$$\phi = \frac{18(1.35)^2(0.0254/2)(10)}{(1.632 \times 10^{-5})(1000)} = 255$$

APPENDIX 8

PACKING FACTOR FOR AREAL PACKING

The maximum packing factor for 2-dimensional droplets of equal size is determined as follows,

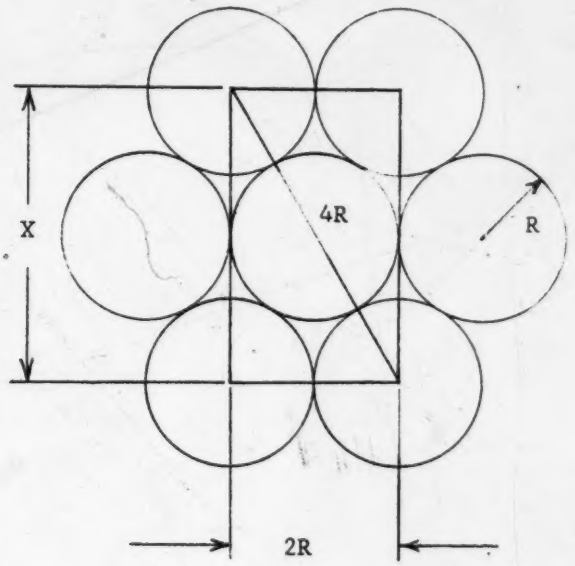

$$X = ((4R)^2 - (2R)^2)^{0.5}$$

and the packing factor in the rectangular region is,

$$PF = \frac{\text{Area occupied by the droplets}}{\text{Area of rectangle}}$$

$$PF = \frac{2 * \pi R^2}{2R * X} = 0.91$$